

**Ba_{1-x}Sr_xCo_yFe_{1-y}O_{3-δ} SOFC cathode materials:
Bulk properties,
kinetics and mechanism of oxygen reduction**

Von der Fakultät Chemie der Universität Stuttgart
zur Erlangung der Würde eines
Doktors der Naturwissenschaften (Dr. rer. nat.)
genehmigte Abhandlung

Vorgelegt von

Lei Wang

aus Qingdao, Shandong, China

Hauptberichter:	Prof. Dr. J. Maier
Mitberichter:	Prof. Dr. E. Roduner
Tag der Einreichung:	21.10.2009
Tag der mündlichen Prüfung:	18.12.2009

Max-Planck-Institut für Festkörperforschung

Stuttgart

2009

Contents

Zusammenfassung	5
Abbreviations and Symbols	9
1 Introduction	13
2 Theoretical background	17
2.1 Oxygen reduction on SOFC cathodes	17
2.2 Transport and reaction	20
2.3 Mixed conducting perovskites (Ba,Sr)(Co,Fe)O _{3-δ}	22
2.3.1 From permeation membranes to SOFC cathodes	23
2.3.2 Lattice constant	24
2.3.3 Oxygen vacancy concentration and diffusion coefficient	24
3 Experimental	27
3.1 Sample preparation	27
3.1.1 Synthesis of powders and preparation of pellets	27
3.1.2 Thin film deposition by pulsed laser deposition	29
3.1.3 Microelectrode preparation by photolithography	30
3.2 Structural and compositional characterization by XRD and ICP-OES	30
3.3 Differential scanning calorimetry	31
3.4 Determination of oxygen nonstoichiometry	31
3.4.1 Thermogravimetric analysis	31
3.4.2 Chemical reaction	32
3.5 Microelectrode impedance spectroscopy	34
3.6 Conductivity relaxation experiments	37
3.7 Oxygen isotope exchange and SIMS measurements	38
4 Results and discussion	43
4.1 Sample characterization	43
4.1.1 X-ray diffraction measurements	43

4.1.1.1	Powders	43
4.1.1.2	Thin films	45
4.1.2	ICP-OES measurements	48
4.2	Stability of (Ba,Sr)(Co,Fe)O _{3-δ}	48
4.2.1	Compatibility with electrolyte materials	49
4.2.2	Stability under CO ₂ -containing atmosphere	52
4.2.3	Long-term phase stability	54
4.3	Impedance spectroscopy on BSCF microelectrodes	55
4.3.1	A representative impedance spectrum without dc bias	55
4.3.2	Temperature dependence	58
4.3.3	Oxygen partial pressure dependence	60
4.3.4	Effect of dc bias	62
4.3.5	Comments on the degradation	64
4.4	Oxygen diffusion coefficients and effective surface exchange constants of Ba _{0.5} Sr _{0.5} Co _{0.8} Fe _{0.2} O _{3-δ}	65
4.5	Influence of bulk properties on oxygen incorporation rate	72
4.5.1	Lattice constant	72
4.5.2	Electronic conductivity	73
4.5.3	Goldschmidt tolerance factor	74
4.5.4	Oxidation enthalpy	76
4.5.5	Oxygen vacancy concentration	78
4.5.6	Oxygen vacancy diffusion coefficient	81
4.6	Proposed oxygen incorporation mechanism for (Ba,Sr)(Co,Fe)O _{3-δ}	82
4.7	Perovskites with mixed monovalent and trivalent ions at A-site	84
5	Summary	87
	References	91
	Acknowledgments	101
	Curriculum Vitae	103

Zusammenfassung

Gegenstand der Arbeit sind hauptsächlich Untersuchungen an gemischtleitenden Oxiden der Zusammensetzung $\text{Ba}_{1-x}\text{Sr}_x\text{Co}_y\text{Fe}_{1-y}\text{O}_{3-\delta}$ (BSCF) mit Perowskitstruktur. Diese werden als Kathodenmaterial für oxidkeramische Brennstoffzellen (SOFC) diskutiert. Das Ziel dieser Arbeit besteht darin, ein besseres Verständnis der komplexen Sauerstoffreduktionsreaktion auf solchen Oxiden im Allgemeinen wie auch für die Anwendungen als katalytisch aktiven Kathode in SOFC zu erhalten.

Für seine Funktion als mögliches SOFC-Kathodenmaterial wurde die Stabilität der BSCFs zunächst an Pulvern untersucht, die durch den Glycin Nitrat-Prozess hergestellt wurden. Was die Stabilität gegenüber Elektrolytmaterialien angeht, wurde zwischen $(\text{Ba}_{0.5}\text{Sr}_{0.5})_{1.04}\text{Co}_{0.8}\text{Fe}_{0.2}\text{O}_{3-\delta}$ (BSCF5080) und 8 mol % $\text{Y}_2\text{O}_3\text{-ZrO}_2$ (YSZ) bereits bei 750 °C eine Reaktion beobachtet. Die unerwünschte Reaktivität ist stärker als die zwischen $\text{La}_{0.6}\text{Sr}_{0.4}\text{Co}_{0.8}\text{Fe}_{0.2}\text{O}_{3-\delta}$ und YSZ. BSCF5080 reagiert ab 850 °C auch mit $\text{Ce}_{0.9}\text{Ge}_{0.1}\text{O}_{2-\delta}$ (CGO). Die erhöhte Reaktivität der BSCF5080 hängt vermutlich mit dem größeren Unterschied der A- und B-Kationengröße zusammen, daher könnten BSCFs mit niedrigeren Ba-Gehalten oder der Ba-Unterstöchiometrie eine höhere Stabilität gegenüber Elektrolyten zeigen. Bezüglich der Stabilität der BSCFs unter CO_2 -haltiger Atmosphäre ist ein hoher Ba-Gehalt schädlich. Auch eine Ba-Unterstöchiometrie kann die Bildung von Karbonaten nicht wirksam hemmen. Deshalb erfordern Ba-haltige Perowskit-Kathodenmaterialien eine hochreine oxidierende Atmosphäre, was für einen praktischen Einsatz nachteilig ist. Einige der BSCF Materialien, die mit kubischen Perowskitstruktur hergestellt werden können, gehen bei mittleren Temperaturen langsam in nichtkubische Phasen über. Für die untersuchten Zusammensetzungen konnte keine offensichtliche Beziehung zwischen der Stabilität der kubischen Perowskitphase bei mittleren Temperaturen und dem Goldschmidt-Toleranzfaktor ermittelt werden. Allerdings zeigt BSCF mit niedrigeren Co Inhalt eine höhere langfristige Phasenstabilität, deshalb könnte das Co/Fe Verhältnis eine wichtige Rolle spielen. Co ändert seine Oxidationsstufe leichter, und die entsprechende Änderung des Ionenradius erleichtert die Bildung von flächenverknüpften Oktaedern mit kürzeren B-O Bindungslängen und der resultierenden nichtkubischen Perowskitphase.

Die Kinetik und der Mechanismus der Sauerstoffreduktion wurde auf geometrisch

wohldefinierten Mikroelektroden untersucht. 100 nm dünne Filme der jeweiligen Zusammensetzungen wurden mit Laserablation (PLD) auf Einkristall-Substraten des Elektrolytmaterials YSZ mit (100) Orientierung aufgebracht. Röntgendiffraktometrie (XRD) zeigt eine hohe Phasenreinheit der Filme und eine stark texturierte Struktur, die von der Filmstärke, der genauen Kationenzusammensetzung und dem Substrat abhängt. Rasterelektronenmikroskopie (SEM) bestätigt, dass die unter den gegenwärtigen Bedingungen hergestellten Dünnschichten säulenförmiges Wachstum aufweisen und porenfrei sind. Die Dünnschichten wurden anschließend durch Photolithographie in kreisförmige Mikroelektroden mit 20 bis 100 μm Durchmessern strukturiert. Eine Silberschicht und -Folie wurden auf der Proberückseite als Gegenelektrode aufgebracht. Impedanzspektren wurden an diesen Mikroelektroden unter Variation von Temperatur, Sauerstoff-Partialdruck und DC-Vorspannung aufgenommen.

Die Sauerstoffreduktion auf diesen BSCF Mikroelektroden verläuft auf dem "Volumenpfad", das heißt, Sauerstoff wird auf der ganzen Elektrodenoberfläche in die Elektrode aufgenommen und anschließend als Sauerstoffionen durch das Volumen der Elektrode transportiert. Die Rate der Sauerstoffaufnahme wird durch die Reaktionsgeschwindigkeit an der Elektrodenoberfläche begrenzt. Basierend auf dem Ersatzschaltbild aus früheren Arbeiten, kann der durch die Sauerstoffeinbaureaktion verursachte Oberflächenwiderstand R_s für BSCFs mit unterschiedlicher Kationenzusammensetzung quantitativ verglichen werden. Die Temperaturabhängigkeit von R_s für die sechs untersuchten BSCF-Zusammensetzungen ist ähnlich, die Aktivierungsenergien liegen im Bereich von 1,3 bis 1,8 eV. Der Exponent n der Abhängigkeit von R_s vom Sauerstoffpartialdruck ($\log R_s - \log P(\text{O}_2)$) liegt zwischen -0,5 und -1, was auf eine Reaktionsordnung der Sauerstoffmoleküle von 1 hinweist. Sowohl kathodische wie anodische DC-Vorspannung verringern R_s . Auf einer wenig degradierten ("frischen") Probe gibt es keine offensichtlichen irreversiblen Veränderungen bis zu 400 mV kathodischer Vorspannung, während auf einer stärker degradierten ("alten") Probe bereits eine kathodische Vorspannung von 300 mV R_s reduziert und zu irreversiblen Veränderungen führt.

Da eine direkte Messung der Art und Bedeckung von Sauerstoff-Zwischenstufen auf der SOFC-Oberfläche unter Betriebsbedingungen schwierig ist, wurden Korrelationen zwischen der effektiven Ratenkonstante k^a (berechnet aus R_s) und verschiedenen Materialeigenschaften untersucht, um Informationen über den Mechanismus der Sauerstoffreduktion zu bekommen. Es existiert keine einfache Korrelation zwischen k^a und der Gitterkonstante, der elektrischen Leitfähigkeit, dem Goldschmidt-Toleranzfaktor oder der Oxidationsenthalpie. Allerdings steigt k^a nichtlinear mit zunehmender Konzentration von Sauerstoffleerstellen $c_{V\bullet}$, was darauf hindeutet, dass die Sauerstoffleerstellen am ratenbe-

stimmenden Schritt der Sauerstoffeinbaureaktion beteiligt sind. Es ist zu vermuten, dass die nichtlineare Erhöhung von k^a mit zunehmender $c_{V\bullet\bullet}$ durch eine zunehmende Beweglichkeit den Sauerstoffleerstellen verursacht wird.

Um diese Annahme zu bestätigen, sind verlässliche Daten des Diffusionskoeffizienten der Sauerstoffleerstellen erforderlich. Aufgrund der relativ geringen Dichte der gesinterten Keramiktabelten und der Komplexität der Experimente ist die Genauigkeit des Sauerstoffleerstellen-Diffusionskoeffizienten aus Messungen der Leitfähigkeitrelaxation für BSCF5080 nicht ausreichend. Zuverlässige Sauerstoffleerstellen-Diffusionskoeffizienten können jedoch an 250 nm dünnen BSCF-Schichten auf (100)-orientiert MgO Einkristallen erhalten werden, die mit PLD hergestellt wurden. Eine gasdichte Gold-Deckschicht wurde auf die BSCF-Filme aufgedampft. Um den Sauerstoff-Isotopenaustausch zwischen BSCF und der Atmosphäre zu ermöglichen, wurde ein etwa 30 μm breiter Schnitt mit relativ scharfen Kanten durch die Gold- und BSCF-Schicht mit einer automatischen Säge angebracht. Der Isotopenaustausch wurde bei verschiedenen Temperaturen durchgeführt, und danach wurde das ^{18}O -Konzentrationsprofil in den abgeschreckten Proben durch Flugzeit-Sekundärionen-Massenspektrometrie (TOF-SIMS) gemessen. Die aus den ^{18}O -Diffusionskoeffizienten (D^*) berechneten Sauerstoffleerstellen-Diffusionskoeffizienten $D_{V\bullet\bullet}$ für BSCF5080 sind deutlich höher als die von $(\text{La,Sr})(\text{Mn,Fe,Co})\text{O}_{3-\delta}$ Perowskiten. Die Aktivierungsenergie E_a von $D_{V\bullet\bullet}$ für BSCF5080 beträgt lediglich $0.47 (\pm 0.04)$ eV, was wesentlich niedriger ist als für $\text{Ba}_{0.5}\text{Sr}_{0.5}\text{FeO}_{3-\delta}$ (BSF, $1.1 (\pm 0.1)$ eV), $\text{SrFeO}_{3-\delta}$ (SF, $0.9 (\pm 0.1)$ eV) und $(\text{La,Sr})(\text{Mn,Fe,Co})\text{O}_{3-\delta}$ (≈ 0.9 eV). Der hohe Wert von $D_{V\bullet\bullet}$ und die niedrige E_a hängen wahrscheinlich mit der niedrigen Kationladung (A^{2+} , ein Teil des Kobalt Co^{2+}) und der hohen Polarisierbarkeit (Ba^{2+} , Co^{2+}) zusammen.

Mit den aus D^* berechneten Leerstellen-Diffusionskoeffizienten $D_{V\bullet\bullet}$ wird die Korrelation zwischen k^a und $D_{V\bullet\bullet}$ bestätigt. Die Erhöhung der k^a -Werte von $(\text{La,Sr})(\text{Mn})\text{O}_{3\pm\delta}$ (LSM) zu $(\text{La,Sr})(\text{Co,Fe})\text{O}_{3-\delta}$ (LSCF) ist vor allem auf die Zunahme der Sauerstoffleerstellenkonzentration zurückzuführen, und die Erhöhung der k^a von LSCF/SF zu $\text{Ba}_{0.5}\text{Sr}_{0.5}\text{Co}_{0.8}\text{Fe}_{0.2}\text{O}_{3-\delta}$ kommt hauptsächlich von der beschleunigten Diffusion der (Oberflächen-) Sauerstoffleerstellen. Basierend auf den experimentellen Beobachtungen und den Schlussfolgerungen aus DFT-Rechnungen an LaMnO_3 -Schichten wird als ratenbestimmender Schritt der Sauerstoffeinbaureaktion in BSCF die Diffusion von Sauerstoffleerstellen zu einem adsorbierten O_2^- vorgeschlagen. Die folgende Dissoziation des in der Leerstelle adsorbierten O_2^- ist schnell.

BSCF weist inhärente Probleme auf, wenn es als SOFC-Kathode angewandt wird, zum Beispiel die unerwünschte Reaktivität mit Elektrolytmaterialien, die Carbonat-Bildung unter CO_2 -haltiger Atmosphäre und die langfristige Phasenumwandlung. Es ist fast

unmöglich, diese Probleme nur durch Zusammensetzungsvariation innerhalb dieser Materialfamilie zu lösen. Deshalb kann BSCF wahrscheinlich nicht als SOFC-Kathode eingesetzt werden. Trotzdem kann, ausgehend vom vorgeschlagenen Mechanismus des Sauerstoffeinbaus in BSCF, eine hohe Sauerstoffleerstellenkonzentration und -Beweglichkeit als Kriterium für die Auswahl der alternativer SOFC-Kathodenmaterialien dienen. In BSCF ist die hohe Sauerstoffleerstellenkonzentration darauf zurückzuführen, dass die 4+ Oxidationsstufe der B-Platz-Kationen nicht sehr stabil ist, und somit die 2+ Oxidationsstufe der A-Plätze vor allem durch die Bildung von Sauerstoffleerstellen ausgeglichen wird. Um die durch Ba eingebrachten Probleme zu vermeiden und die durchschnittliche Oxidationsstufe den A-Plätzen auf 2+ zu halten, wurden Perowskite mit einer Kombination aus Alkalimetall (1+) und Seltenerdmetall (3+) auf den A-Plätzen untersucht. Die Löslichkeit von Ag in $(\text{La,Ag})\text{Co}_{0.4}\text{Fe}_{0.6}\text{O}_{3-\delta}$ Perowskiten ist ziemlich begrenzt. Für K-haltige $(\text{La,K})\text{Co}_{0.4}\text{Fe}_{0.6}\text{O}_{3-\delta}$ und $(\text{Nd,K})\text{Co}_{0.4}\text{Fe}_{0.6}\text{O}_{3-\delta}$ Perowskite ist es schwierig, einphasige Pulver zu erhalten. Die R_s -Werte aus impedanzspektroskopischen Messungen eines Materials mit einer nominalen Zusammensetzung $\text{La}_{0.5}\text{Co}_{0.4}\text{Fe}_{0.6}\text{O}_{3-\delta}$ und einer vorherrschenden Perowskitphase sind eine Größenordnung höher als für LSCF und wird wahrscheinlich durch die Verunreinigung mit Nicht-Perowskitphasen verursacht. Ausgehend von dem in dieser Arbeit vorgeschlagenen Mechanismus sollten Materialien mit schnellem Sauerstoffaustausch eine hohe Beweglichkeit der Sauerstoffleerstellen haben. Dies ermuntert zur Untersuchung von Perowskiten mit stark polarisierbaren A-Kationen. In dieser Hinsicht ist Bi^{3+} anstelle von Ba^{2+} ein interessanter Kandidat, der auch die Probleme der Karbonatbildung verringern könnte.

Abbreviations and Symbols

List of Abbreviations

ac	alternating current
APU	auxiliary power unit
BET	Brunauer-Emmett-Teller method
BSCF	$(\text{Ba,Sr})(\text{Co,Fe})\text{O}_{3-\delta}$
BSCF2580	$\text{Ba}_{0.25}\text{Sr}_{0.75}\text{Co}_{0.8}\text{Fe}_{0.2}\text{O}_{3-\delta}$
BSCF5040	$\text{Ba}_{0.5}\text{Sr}_{0.5}\text{Co}_{0.4}\text{Fe}_{0.6}\text{O}_{3-\delta}$
BSCF5080	$\text{Ba}_{0.5}\text{Sr}_{0.5}\text{Co}_{0.8}\text{Fe}_{0.2}\text{O}_{3-\delta}$ or $(\text{Ba}_{0.5}\text{Sr}_{0.5})_{1.04}\text{Co}_{0.8}\text{Fe}_{0.2}\text{O}_{3-\delta}$
BSF	$\text{Ba}_{0.5}\text{Sr}_{0.5}\text{FeO}_{3-\delta}$
CGO	$\text{Ce}_{0.9}\text{Ge}_{0.1}\text{O}_{2-\delta}$
CHP	combined heat and power
dc	direct current
DSC	differential scanning calorimetry
HS	high spin
ICP-OES	inductively coupled plasma - optical emission spectroscopy
IS	intermediate spin
IT-SOFC	intermediate temperature solid oxide fuel cell
LS	low spin
LSC	$\text{La}_{0.6}\text{Sr}_{0.4}\text{CoO}_{3-\delta}$
LSCF	$(\text{La,Sr})(\text{Co,Fe})\text{O}_{3-\delta}$
LSCF6080	$\text{La}_{0.6}\text{Sr}_{0.4}\text{Co}_{0.8}\text{Fe}_{0.2}\text{O}_{3-\delta}$
LSF	$\text{La}_{0.6}\text{Sr}_{0.4}\text{FeO}_{3-\delta}$
LSM	$(\text{La,Sr})\text{MnO}_{3\pm\delta}$
LSM80	$(\text{La}_{0.8}\text{Sr}_{0.2})_{0.92}\text{MnO}_{3-\delta}$
MIEC	mixed ionic-electronic conductor
PLD	pulsed laser deposition
RDS	rate-determining step
SCF	$\text{SrCo}_{0.8}\text{Fe}_{0.2}\text{O}_{3-\delta}$

SEM	scanning electron microscopy
SF	$\text{SrFeO}_{3-\delta}$
SIMS	secondary ion mass spectrometry
SOFC	solid oxide fuel cell
TG	thermogravimetry
TOF-SIMS	time-of-flight secondary ion mass spectrometry
XPS	X-ray photoelectron spectroscopy
XRD	X-ray diffraction
YSZ	8 mol % or 9.5 mol % $\text{Y}_2\text{O}_3\text{-ZrO}_2$

List of Symbols

c_{O}	concentration of lattice oxygen
$c_{\text{O}^{2-}}$	oxygen ion concentration
c_{p}	heat capacitance
$c_{\text{V}\bullet\bullet}$	oxygen vacancy concentration
C_{i}	capacitance corresponding to the electrode/electrolyte interface
C_{δ}	chemical capacitance
d_{ME}	diameter of the microelectrode
D	diffusion coefficient
D^{a}	diffusion coefficient determined by an “electrical” experiment
D^{δ}	chemical diffusion coefficient
D^*	tracer diffusion coefficient
$D_{\text{V}\bullet\bullet}$	oxygen vacancy diffusion coefficient
e	elementary charge
E^0	theoretical cell potential
E_{a}	activation energy
f	correlation factor
F	Faraday constant
ΔG°	standard value of the change in Gibbs energy for a reaction
ΔH_{ox}	oxidation enthalpy
j	particle flux
k	effective surface exchange rate constant
k^{a}	surface exchange rate constant determined by an “electrical” experiment
k^{δ}	surface exchange rate constant determined by a “chemical” experiment

k^*	surface exchange rate constant determined by a “tracer” experiment
k_B	Boltzmann constant
$P(O_2)$	oxygen partial pressure
$P(CO_2)$	CO_2 partial pressure
Q	constant phase element
r	ionic radius
r_c	critical radius
R	gas constant
R_b	YSZ bulk resistance
R_i	resistance corresponding to the ion transfer across the electrode/electrolyte interface
R_s	area specific surface resistance
t	Goldschmidt tolerance factor or time
T	absolute temperature
$V_O^{\bullet\bullet}$	oxygen vacancy
w_c	Carnot efficiency
z	charge number
δ	oxygen nonstoichiometry
μ	chemical potential
$\tilde{\mu}$	electrochemical potential
σ	electrical conductivity
σ_{eon}	electronic conductivity
σ_{ion}	ionic conductivity
$\sigma_{O^{2-}}$	oxygen ion conductivity
σ_O^δ	effective ambipolar conductivity of oxygen
φ	electrical potential
ω_O	thermodynamic factor of oxygen

Chapter 1

Introduction

Fuel cells are energy conversion devices which convert chemical energy directly into electrical energy without intermediate steps involving thermal and mechanical energy. One advantage is its high efficiency that is not limited by Carnot's law. Take $\text{H}_2 + 1/2\text{O}_2 \rightarrow \text{H}_2\text{O}(\text{g})$ reaction as an example: if the electrical energy is obtained from the combustion process, the efficiency cannot exceed the Carnot-efficiency w_c , e. g., for a heat engine operated between 373 K and 900 K $w_c = 0.59$, while the theoretical efficiency (defined as the ratio between Gibbs energy and enthalpy of the cell reaction) for SOFC is 0.80 at 900 K. Fuel cells are at the same time more environmentally friendly mainly because of the high efficiency.

Among different types of fuel cells, solid oxide fuel cells (SOFCs) typically operate at relatively high temperature (e. g., 800 °C - 1000 °C). In the case of an oxide ion conductor as the electrolyte, gas-phase oxygen is reduced at the cathode, the oxide ions are transported through the electrolyte, and react with the fuel, such as hydrogen, to produce water at the anode. The electrons travel in an external circuit and deliver electric power. This high operation temperature was originally due to the limited conduction of the thick electrolyte and is nowadays mainly chosen because of the beneficial influence on the electrode overpotential. An additional reason for the high operation temperature is that it enables the internal reforming of the fuels (the conversion of hydrocarbons to CO or CO₂ and H₂) which results in the flexibility in terms of the choice of fuels. The waste heat produced at this temperature also facilitates the integration of SOFC and a gas turbine into a power generation system which further increases the efficiency.

Potential applications for SOFCs have been discussed by Singhal [1]. One factor that limits its large-scale commercialization is the still relatively high cost compared to traditional power generation. Besides, high temperatures lead to stringent requirements on materials. Therefore there is a tendency to move to intermediate temperature SOFCs (IT-SOFCs), e. g., 500 °C to 750 °C, so that the use of cheaper materials and reduced system

costs would be possible. IT-SOFCs are especially suitable for small scale applications, such as micro combined heat and power devices (micro-CHP) in stationary applications and auxiliary power units (APUs) in mobile applications (automotive; refrigeration units) [2].

Since many of the processes that are relevant for fuel cell operation are thermally activated, decreasing operation temperature would result in poorer performance, for example, higher polarization losses with regard to oxygen reduction at the cathode. This could be compensated in different ways. While one single cell can generally supply only a voltage of about 1 V [3], it is common to connect more than one cell into stacks. Accordingly it is possible to improve the design of the stack as well as the fabrication techniques to achieve better performance [4,5]. However, the effort to develop novel materials and optimize the existing materials should never be underestimated [6].

Based on the function of different components and the operation conditions, there are certain requirements for the materials. From a technical point of view, a cathode material should have [5, 7]:

- (1) high electrocatalytic activity towards oxygen reduction;
- (2) sufficient electronic conductivity;
- (3) high stability in oxidizing environment;
- (4) tolerance in CO₂-containing atmosphere;
- (5) chemical compatibility with the electrolyte, interconnect and sealing materials;
- (6) similar thermal expansion coefficients with other components.

Identifying materials that fulfill the aforementioned conditions is obviously nontrivial. One promising candidate for SOFC cathodes are mixed ionic-electronic conducting (MIEC) perovskite oxides due to their high catalytic activity towards oxygen reduction. Oxides with perovskite structure are particularly suited because their properties can be adjusted in a wide range by doping on the A-site as well as on the B-site.

The state-of-the-art MIEC perovskite cathode materials are (La,Sr)MnO_{3±δ} (LSM) and (La,Sr)(Co,Fe)O_{3-δ} (LSCF) and they have been intensively studied during the last two decades [8]. Driven by the requirement of lowering SOFC operation temperature, many new compositions have been proposed and tested, and (Ba,Sr)(Co,Fe)O_{3-δ} (BSCF) is one of the most attractive candidates with respect to high oxygen diffusivity and fast oxygen reduction kinetics [9, 10]. There might be some intrinsic shortcomings of this material that prevent it from being an ideal SOFC cathode material, such as the formation of carbonate in the presence of CO₂ and limited compatibility with the electrolyte. However, the encouraging performance greatly stimulates the detailed study of the oxygen reduction on this material and enables a deeper insight into the complex reaction mechanism.

In this thesis, (Ba,Sr)(Co,Fe)O_{3-δ} materials with varying Ba/Sr and Co/Fe ratios are

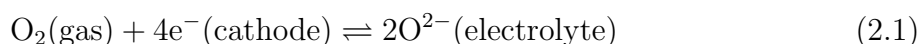
investigated from two aspects: On one hand, the properties related to the SOFC operation have been studied focusing mainly on the stability; and on the other hand, the oxygen reduction mechanism has been investigated. Emphasis has been put on correlations between structure, properties and performance of the materials. This is supposed to help identify the crucial requirements for high electrocatalytic activity and to develop better cathode materials.

Chapter 2

Theoretical background

2.1 Oxygen reduction on SOFC cathodes

With an oxygen ion conductor as electrolyte, the oxygen reduction reaction at the SOFC cathode side is expressed by the following overall formula:



Depending on the materials properties and the electrode geometry, two main oxygen reduction paths can be distinguished: the “surface path” and the “bulk path”. As indicated in the reaction equation, as an electrode material, certain electronic conductivity is necessary. If the cathode material is a pure electronic conductor such as Pt, the incorporation follows the surface path (Fig. 2.1a). In the surface path, oxygen molecules are adsorbed on the surface of the cathode and diffuse to the three-phase boundary where gas, cathode and electrolyte meet. It is only at the three-phase boundary that oxygen incorporation occurs. This active zone represents only a small fraction of the whole electrode/electrolyte arrangement. If, however, the cathode material exhibits a certain ionic conductivity besides the electronic conductivity, such as in mixed conducting perovskites, the oxygen incorporation through the bulk path (Fig. 2.1b) typically becomes preferable. In this case, oxygen adsorption, dissociation, ionization and incorporation all take place at the surface of the cathode material. Subsequently the incorporated O^{2-} ions migrate through the bulk cathode material and are transferred into the electrolyte at the whole electrode/electrolyte contact area.

For mixed conducting perovskites $(\text{Ba,Sr})(\text{Co,Fe})\text{O}_{3-\delta}$, $(\text{La,Sr})(\text{Co,Fe})\text{O}_{3-\delta}$ and even $(\text{La,Sr})\text{MnO}_{3\pm\delta}$ under certain conditions [11], the bulk path is the main oxygen incorporation path which is composed of several processes. With regard to kinetics analysis, we assume that one of the processes is much slower than the others which are in quasi-equilibrium. In the bulk path, the limiting process could be the gas diffusion, the surface

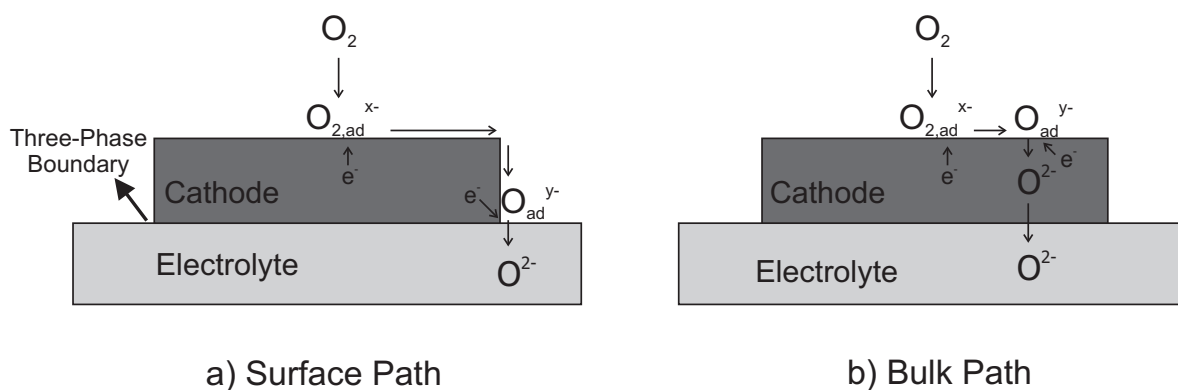


Figure 2.1: Sketch of two possible oxygen reduction paths at SOFC cathodes: a) Surface path; b) Bulk path.

oxygen incorporation reaction, the ion transport through the cathode or the ion transfer from the cathode into the electrolyte. A complex electrode morphology impedes the separation of different processes. But the restriction caused by the morphology can be released by studying dense thin film [12,13] or geometrically well-defined microelectrodes [14]. The experiments in this thesis were carried out on BSCF dense thin film microelectrodes. The cathode being pore-free excludes the possibility of the gas diffusion being limiting, and the geometry and the relatively high ionic conductivity of the material excludes the possibility of the ion transport through the cathode being limiting. Among the remaining two processes, it has been shown that the overall kinetics is essentially limited by the oxygen surface incorporation reaction [15].

The fundamental understanding of the mechanism of this surface reaction is however quite limited. This is at least partially due to the difficulty of directly detecting the nature and the coverage of intermediate oxygen species on the cathode materials by in situ experiments. It is mainly because the cathode reaction takes place under higher oxygen partial pressure, while surface analysis is carried out under high vacuum. Based on the detailed knowledge of the material's defect chemistry and extended kinetic experiments, a certain understanding of the oxygen incorporation mechanism into SrTiO_3 , a representative of the perovskite family with large band gap, is available [16]. Nevertheless, direct transfer of the conclusions to the analysis of cathode materials with a very different electronic structure (small or vanishing band gap) is difficult.

The oxygen incorporation reaction is composed of a series of reaction steps. A plausible sequence of elementary steps is listed as follows using the Kröger-Vink notation [17]:





The subscript “ad” represents adsorbates, $\text{V}_{\text{O}}^{\bullet\bullet}$ the oxygen vacancy, $\text{O}_{\text{O}}^{\bullet}$ the oxygen in the lattice with an effective positive charge, $\text{O}_{\text{O}}^{\text{x}}$ the regular oxygen in the lattice (neutral in terms of Kröger-Vink nomenclature) and M the B-site transition metal in the perovskite structure which can easily change its valence state. The electronic charge carriers are represented by $\text{M}_{\text{M}}^{\text{x}}$ (B-site transition metal at its initial valence state) and $\text{M}_{\text{M}}^{\bullet}$ (charge carriers with an effective positive charge realized by increasing the valence state of B-site transition metal) here, because under the temperature and oxygen partial pressure studied the electronic conduction of BSCF materials is attributed to the hopping of small polarons associated with charge fluctuations [18].

Among the aforementioned steps, one of them is supposed to be the rate-determining step RDS (the RDS may also comprise several of these steps) and the other steps to be in quasi-equilibrium. The overall oxygen partial pressure $P(\text{O}_2)$ dependence of the oxygen exchange rate (related to the surface resistance R_s) is an instructive parameter that can be compared to predictions from different possible reaction mechanisms. In this way it is possible to corroborate a proposed mechanism or to rule it out (section 4.3.3). On the other hand, the materials properties have individual influence on each step by affecting concentrations and mobilities of the involved point defects. For example, the reactions (2.2) and (2.3) will be accelerated by easily transferable electrons (sufficient concentration and suitable energetic position of $\text{M}_{\text{M}}^{\text{x}}$). The basicity of the perovskites may change the relative stability of the adsorbed oxygen species. The surface defect concentration and/or mobility are not identical but coupled to the bulk values. As a result, by investigating the correlation of the reaction rate or the surface resistance R_s with certain (bulk) properties of the materials, indications of the corresponding reaction mechanism could be obtained (section 4.5) and the electrode performance could eventually be correlated to the underlying materials properties. Identifying the rate-determining step as a basis for a better understanding of the oxygen incorporation reaction mechanism is then the main focus of this thesis.

2.2 Transport and reaction

Within the bulk path of the oxygen reduction reaction, the processes under consideration are the oxygen incorporation reaction at the surface and the oxygen diffusion in the bulk. The rate of the oxygen surface incorporation (= reaction) and the bulk diffusion (= transport) can be quantified with an effective exchange rate constant k and a diffusion coefficient D . The measured absolute values of k and D are however dependent on the applied experimental techniques corresponding to the different nature of the driving force. The driving force is the gradient of the electrochemical potential

$$\nabla\tilde{\mu} = \nabla\mu + ze\nabla\varphi. \quad (2.7)$$

μ is the chemical potential, z the charge number, e the elementary charge and φ the electrical potential. When a driving force is applied, after a certain transient steady-state fluxes of charge carriers are built up. Let us first consider that diffusion is the limiting process. In the realm of linear irreversible thermodynamics, i. e., for small driving forces, the relation between the net particle flux j and the gradient of the electrochemical potential for charged particles is given by [19,20]

$$j = -\frac{\sigma}{z^2e^2}\nabla\tilde{\mu}. \quad (2.8)$$

where σ is the respective conductivity.

The Nernst-Einstein equation relates conductivity and diffusion coefficient, e. g., for the oxygen ion conductivity $\sigma_{O^{2-}}$ (vacancies as mobile charge carriers):

$$\sigma_{O^{2-}} = \frac{4F^2c_{V_{\bullet\bullet}O}D_{V_{\bullet\bullet}O}}{RT} \quad (2.9)$$

in which F is the Faraday constant, R the gas constant, T the absolute temperature, $c_{V_{\bullet\bullet}O}$ the oxygen vacancy concentration and $D_{V_{\bullet\bullet}O}$ the oxygen vacancy diffusion coefficient. If one relates $\sigma_{O^{2-}}$ to the concentration of oxide ions $c_{O^{2-}}$, this leads to the definition of D^a :

$$D^a = \frac{c_{V_{\bullet\bullet}O}}{c_{O^{2-}}}D_{V_{\bullet\bullet}O}. \quad (2.10)$$

In an isotope exchange experiment (“tracer” experiment), the gradient of the electrochemical potential can be transformed to the gradient of the ^{18}O concentration $c_{O^{2-}}^*$ since the isotope distribution is random.

$$\nabla\mu_{O^{2-}}^* = RT\frac{\nabla c_{O^{2-}}^*}{c_{O^{2-}}^*}. \quad (2.11)$$

The resulting ^{18}O fluxes $j_{O^{2-}}^*$ can then be expressed as

$$j_{O^{2-}}^* = -\frac{\sigma_{O^{2-}}^*}{4F^2}\nabla\mu_{O^{2-}}^* = -\frac{RT\sigma_{O^{2-}}^*}{4F^2c_{O^{2-}}^*}\nabla c_{O^{2-}}^* = -\frac{RT\sigma_{O^{2-}}}{4F^2c_{O^{2-}}}\nabla c_{O^{2-}}^*. \quad (2.12)$$

The tracer diffusion coefficient D^* is thus

$$D^* = \frac{RT\sigma_{O_{2-}}}{4F^2c_{O_{2-}}}. \quad (2.13)$$

For the oxygen vacancy the environment before and after the jump is equivalent; the next oxygen vacancy jump can occur in any direction. However from the point view of a labeled ion, after the exchange with a vacancy position, the situation is different. As long as the oxygen vacancy concentration is low, most probably there will not be a second oxygen vacancy neighboring the labeled oxygen. Thus the chance is high that it jumps back to its initial position, reducing the tracer diffusion coefficient. The respective correlation factor f depends on the migration mechanism and the crystallographic lattice; for the oxygen vacancy jump in the perovskite structure $f = 0.69$ [21]. Thus

$$D^* = f \cdot D^a = f \frac{c_{V_{O^{\bullet\bullet}}}}{c_{O_{2-}}} D_{V_{O^{\bullet\bullet}}}. \quad (2.14)$$

In a chemical relaxation experiment, under the driving force of a $P(O_2)$ gradient, the oxide adjusts its nonstoichiometry with ambipolar diffusion of electronic and ionic charge carriers. The ambipolar conductivity σ_O^δ is the harmonic average of the individual electronic conductivity σ_{eon} and ionic conductivity σ_{ion} [22], $\sigma_O^\delta = (\sigma_{eon}\sigma_{ion})/(\sigma_{eon} + \sigma_{ion})$. The flux-force relation is then expressed as

$$j_O = -\frac{1}{4F^2}\sigma_O^\delta \nabla \mu_O = -\left(\frac{1}{4F^2}\sigma_O^\delta \frac{\partial \mu_O}{\partial c_O}\right) \nabla c_O. \quad (2.15)$$

Hence the chemical diffusion coefficient becomes

$$D^\delta = \frac{1}{4F^2}\sigma_O^\delta \frac{\partial \mu_O}{\partial c_O}. \quad (2.16)$$

For $\sigma_{eon} \gg \sigma_{ion}$ we get

$$D^\delta \approx \frac{c_{V_{O^{\bullet\bullet}}}}{RT} \frac{\partial \mu_O}{\partial c_O} D_{V_{O^{\bullet\bullet}}} = \frac{\omega_O c_{V_{O^{\bullet\bullet}}}}{c_O} D_{V_{O^{\bullet\bullet}}}. \quad (2.17)$$

ω_O is the thermodynamic factor and equal to $(c_O/RT)(\partial \mu_O/\partial c_O)$.

Similarly, the different effective rate constants k (k^a , k^* and k^δ) for the surface reaction from different experiments can be distinguished [23]. Instead of being the ratio between the flux and the gradients in the case of diffusion coefficient, k is defined as the ratio between the flux and the concentration deviation δc at the surface from the equilibrium state. When the deviation is small:

$$j = k \cdot \delta c. \quad (2.18)$$

The relations between the different k 's are analogous to the diffusion coefficients:

$$k^a \approx k^*. \quad (2.19)$$

$$k^\delta = \omega_0 k^* \quad (2.20)$$

They are discussed in detail in Refs [23–25]. k^* is proportional to the equilibrium exchange rate \mathfrak{R}_0 of the surface reaction

$$k^* \propto \mathfrak{R}_0 \quad (2.21)$$

which is related to the rates $\overrightarrow{\mathfrak{R}}$, $\overleftarrow{\mathfrak{R}}$ of forward and backward reaction

$$\mathfrak{R}_0 = \sqrt{\overrightarrow{\mathfrak{R}} \overleftarrow{\mathfrak{R}}} = \sqrt{\overrightarrow{k} [A]^a [B]^b \dots \overleftarrow{k} [U]^u [V]^v \dots} \quad (2.22)$$

where \overrightarrow{k} , \overleftarrow{k} are forward/backward reaction rate constants and $[A]^a \dots [U]^u \dots$ are the equilibrium concentrations of the involved species with their respective reaction orders a, \dots, u, \dots . Thus the $P(O_2)$ dependence of $k^q \approx k^*$ is determined by the mechanism of the surface reaction.

2.3 Mixed conducting perovskites (Ba,Sr)(Co,Fe)O_{3-δ}

The crystal structure of cubic perovskite-type oxides with the formula ABO₃ can be described in two ways: 1. The relatively big A-site cations occupy the corners of the cubic lattice and the relatively small B-site cations stay at the center of the cubic structure. Oxygen ions are sitting at the face centers of the cube. A-site cations and oxygen ions with similar sizes form a closed packing face-centered cubic (fcc) lattice. (Fig. 2.2a) 2. The structure could also be viewed as composed of BO₆ octahedra which share corners infinitely in all 3 dimensions resulting in a symmetric structure. The A cations occupy the voids created by 8 BO₆ octahedra, leading to a 12-fold oxygen coordination for the A-site cations and a 6-fold oxygen coordination for the B-site cations. (Fig. 2.2b) The stability of the cubic perovskite structure can be indicated by the Goldschmidt tolerance factor $t = (r_A + r_O) / \sqrt{2}(r_B + r_O)$ in which r_A , r_B and r_O are the ionic radii of A, B and O ions with their appropriate coordination numbers, valence and spin states. In the ideal cubic perovskite structure, t is equal to 1. In general, the perovskite structure is quite flexible with regard to the doping at both A- and B- sites. This greatly facilitates the tailoring of materials properties in order to meet requirements for various applications.

A crucial feature which is also emphasized in Fig. 2.2, are the oxygen vacancies in this structure which allow for charge compensation if the sum of A- and B- cation charge is below +6. The ability to host a perceptible number of oxygen vacancies is well represented in (Ba,Sr)(Co,Fe)O_{3-δ} where δ up to 0.6 at 700 °C in air was observed [27]. The oxygen vacancies are the mobile ionic defects while the cation mobility is relatively low in this structure [28,29]. The migration of the oxygen vacancies follows a curved path instead of

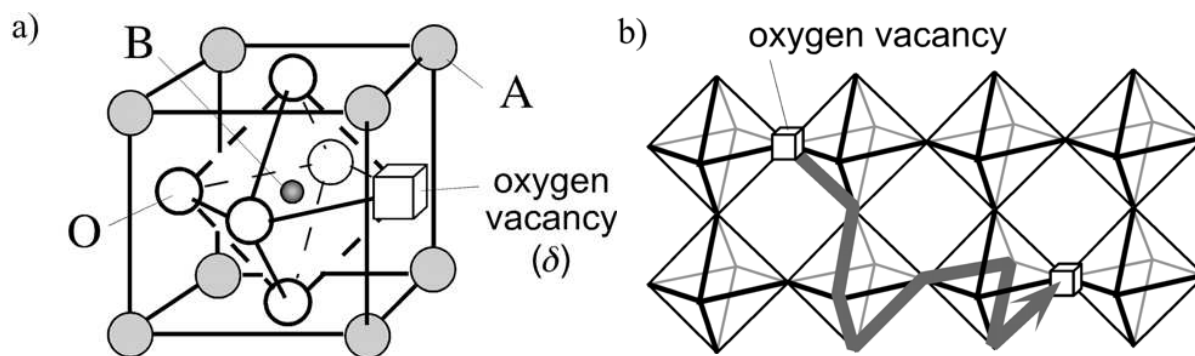


Figure 2.2: Crystal structure of perovskite oxide ABO_3 depicted by a) The positions of the ions in a cubic structure; b) Corner-sharing BO_6 octahedra and oxygen vacancy migration path. From Ref. [26].

a linear path along the edge of the BO_6 octahedra [30]. These vacancies are shown to be of great importance for the oxygen bulk transport and surface incorporation reaction.

2.3.1 From permeation membranes to SOFC cathodes

In the development of oxygen permeation membranes, perovskites with transition metals at the B-site and partial or full substitution of rare earth metals by alkaline earth metals at the A-site have attracted considerable attention mainly due to their fast oxygen transport. Among those compositions, $(La,Sr)(Co,Fe)O_{3-\delta}$ has been intensively investigated [31–33]. While in this material solid solution series, $SrCo_{0.8}Fe_{0.2}O_{3-\delta}$ exhibited the highest oxygen permeation rate [34], the phase transition into the vacancy-ordered Brownmillerite phase e. g., at $750\text{ }^\circ\text{C}$ and $p(O_2) = 0.015\text{ atm}$ [35] was detrimental for the application. To stabilize the cubic perovskite phase, Ba was introduced into $SrCo_{1-y}Fe_yO_{3-\delta}$ leading to $(Ba,Sr)(Co,Fe)O_{3-\delta}$. The previous study showed that the introduction of Ba into $SrCo_{1-y}Fe_yO_{3-\delta}$ can effectively stabilize the cubic perovskite structure even under low oxygen partial pressure and temperature, and maintain high oxygen permeability at the same time [9]. $Ba_{0.5}Sr_{0.5}Co_{0.8}Fe_{0.2}O_{3-\delta}$ (BSCF5080), in which 50% of Sr was substituted by Ba, has reached a high oxygen permeability and was estimated to be structurally stable based on the evaluation of the Goldschmidt tolerance factor [36], and therefore is the main composition in many following studies. Besides the application as oxygen permeation membranes, BSCF also showed its applicability in partial oxidation of methane to syngas [37] and ammonia oxidation [38]. In 2004, BSCF was assessed as SOFC cathode material [10]. With doped ceria as the electrolyte, a fuel cell with BSCF cathode exhibited a high power density of 1010 mWcm^{-2} at $600\text{ }^\circ\text{C}$ with humidified hydrogen as the fuel. Due to the high activity for oxygen incorporation but moderate activity for hydrocarbon

oxidation, BSCF has also been demonstrated to be suitable for being applied as cathodes in single-chamber fuel cells operated with propane [10] or methane [39]. Since BSCF was applied in the form of porous thick films in fuel cell studies [10], the electrode performance is determined rather by the surface oxygen incorporation reaction (k) than by the bulk transport (D). This interesting finding of a high surface electrocatalytic activity for a material mainly optimized with respect to fast bulk oxygen transport brings BSCF into the focus of the present study.

2.3.2 Lattice constant

Depending on the exact cation composition, BSCF may not always crystallize in cubic perovskite structure or as a single phase [36, 40, 41]. Ideal cubic perovskites can only be obtained when the Goldschmidt tolerance factor t is close to 1. For $0.75 \leq t \leq 1$, non-cubic distortions are formed; while $t \gg 1$ commonly results in a transformation into phases based on the hexagonal perovskite structure, e. g., 2H-type perovskite structure which contains chains of face-sharing BO_6 octahedra [42]. The reduction of the oxygen permeation flux through Brownmillerite-structured dense membranes, which have a vacancy-ordered structure, also hints towards a reduction of the oxygen transport rate in the distorted perovskite structure [43]. Although there is no direct measurements indicating slower oxygen transport in the hexagonal perovskite structure, it is generally believed that the reduced symmetry of the lattice may lead to a higher barrier for the oxygen diffusion and highly anisotropic transport properties. Therefore, in this thesis, mainly the compositions with cubic perovskite structure were investigated.

Due to the large size difference between Ba^{2+} (1.61 Å) and Sr^{2+} (1.44 Å) [44], the lattice constants in BSCF vary remarkably with the cation composition, especially with Ba content. This is illustrated in Fig. 2.3. The lattice constant of the cubic perovskite phase in BSCF increases linearly with Ba content, while the variation of Co/Fe ratio has much less influence on it. The general tendency is that the lattice constant slightly increases with increasing Co content. The variation of lattice constants with cation compositions is a representative example of the adjustability of the materials properties in BSCF.

2.3.3 Oxygen vacancy concentration and diffusion coefficient

In BSCF, the lower valence state (exclusively 2+ instead of 2+/3+ mixture) at the A-site could be compensated by the oxidation of B-site ions (which would affect the electronic conductivity in these materials) and/or by the formation of oxygen vacancies. In which way the compensation is preferred depends on how easily the B-site cations switch to higher oxidation states. Since the stability of 4+ oxidation state is much lower for Fe and

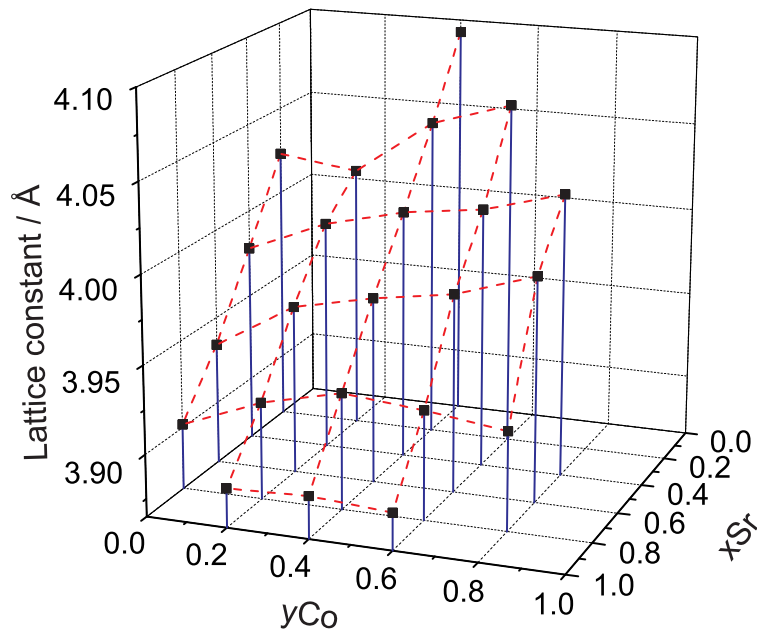


Figure 2.3: Dependence of lattice constants of cubic perovskites in $\text{Ba}_{1-x}\text{Sr}_x\text{Co}_y\text{Fe}_{1-y}\text{O}_{3-\delta}$ on composition at 1273 K in air with data from Ref. [41].

Co than for Mn, compensation by $\text{V}_{\text{O}}^{\bullet\bullet}$ is preferred in BSCF in contrast to LSM. While the relative changes of the oxygen vacancy concentration upon the changes of temperature and oxygen partial pressure can be accurately determined by thermogravimetry, the determination of the absolute values is however nontrivial (see section 4.6 for details). As can be seen from Fig. 2.4a, δ values for $\text{Ba}_{0.5}\text{Sr}_{0.5}\text{Co}_{0.8}\text{Fe}_{0.2}\text{O}_{3-\delta}$ from different references and obtained by different methods show a large scatter even when they were measured under similar oxygen partial pressures (0.1 - 0.2 bar). Most of the recent references agreed that δ may exceed 0.5 and contrary to the situation for SCF, the cubic perovskite structure is maintained even at moderate temperatures, i. e., no oxygen vacancy ordered superstructures such as the Brownmillerite phase occur [45].

Similar to the situation for the absolute values of oxygen nonstoichiometry, the reported oxygen vacancy diffusion coefficients $D_{\text{V}_{\text{O}}^{\bullet\bullet}}$ for $\text{Ba}_{0.5}\text{Sr}_{0.5}\text{Co}_{0.8}\text{Fe}_{0.2}\text{O}_{3-\delta}$ also exhibit considerable scatter (Fig. 2.4b). Since most of the data were obtained from oxygen permeation measurements, the variation may at least be partly due to the difficulty to sinter $\text{Ba}_{0.5}\text{Sr}_{0.5}\text{Co}_{0.8}\text{Fe}_{0.2}\text{O}_{3-\delta}$ into pore-free dense samples. The activation energy was found to be 0.4 - 0.6 eV [9, 10, 46, 47] which is significantly lower than the typical value of 0.9 eV observed for LSCF and LSM perovskites [21, 48]. Only the calculated $D_{\text{V}_{\text{O}}^{\bullet\bullet}}$ from conductivity relaxation measurements at intermediate temperatures was higher (0.8 - 0.9 eV) [49]. All these studies agree in the finding that the absolute $D_{\text{V}_{\text{O}}^{\bullet\bullet}}$ values are higher than those

for the widely studied $(\text{La,Sr})(\text{Co,Fe})\text{O}_{3-\delta}$ [49, 50] and $(\text{La,Sr})\text{MnO}_{3\pm\delta}$ [51] perovskites.

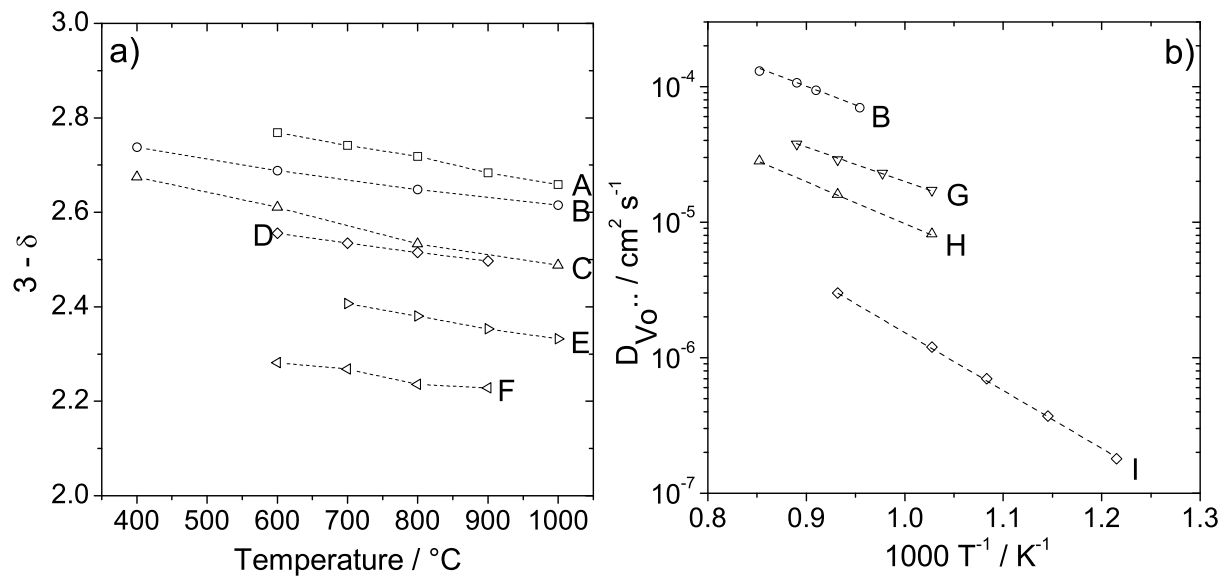


Figure 2.4: Temperature dependence of a) oxygen stoichiometry $3-\delta$ for $\text{Ba}_{0.5}\text{Sr}_{0.5}\text{Co}_{0.8}\text{Fe}_{0.2}\text{O}_{3-\delta}$ ($P(\text{O}_2)$ is in the range of 0.1 - 0.2 bar). b) Oxygen vacancy diffusion coefficient $D_{V_{\text{O}}^{..}}$ for $\text{Ba}_{0.5}\text{Sr}_{0.5}\text{Co}_{0.8}\text{Fe}_{0.2}\text{O}_{3-\delta}$. A = [52]; B = [10]; C = [53]; D = [49]; E = [27]; F = [54]; G = [46]; H = [47]; I = [49], D^{δ} extrapolated to 0.1 bar.

Chapter 3

Experimental

3.1 Sample preparation

3.1.1 Synthesis of powders and preparation of pellets

All the perovskite powders with various cation compositions (except SrFeO_3 , from solid state reaction of SrCO_3 and Fe_2O_3) studied in this thesis were synthesized from the metal nitrates by the glycine nitrate process [55]. First, aqueous solutions of the metal nitrates $\text{Ba}(\text{NO}_3)_2$, $\text{Sr}(\text{NO}_3)_2$, $\text{La}(\text{NO}_3)_2$, $\text{Nd}(\text{NO}_3)_3$, KNO_3 , AgNO_3 , $\text{Co}(\text{NO}_3)_2$ and $\text{Fe}(\text{NO}_3)_3$ were prepared with concentrations close to 1 mol/l (only for $\text{Ba}(\text{NO}_3)_2$, a solution with a concentration about 0.25 mol/l was used due to the low solubility). The cation concentrations in these stock solutions (except AgNO_3) were determined accurately by inductively coupled plasma - optical emission spectroscopy (ICP-OES, Analytical Chemistry Lab of the Max Planck Institute for Metals Research). The required amounts of the respective solutions were then mixed in a 2000 ml beaker, and for every 40 g powder prepared approximately 25 g glycine was added. The mixture (each batch 70 to 100 ml) was heated by a heating plate in the fumehood until the water was completely evaporated and the combustion finished. The beaker was covered with a glass plate to avoid severe loss of the powder during the vehement/strongly exothermic reaction. The obtained powder from different batches was subsequently ground together in a mortar and calcined in air for 12 h. For most of the BSCF compositions, 1000 °C was high enough to obtain a powder with predominant cubic perovskite phase, while higher calcination temperatures were necessary for some of them (see Table 3.1). The calcined powder was ground again and ballmilled for 2 h in a zirconia ballmill, and isostatically pressed into a cylindrical pellet at 0.5 GPa for 2 minutes and then sintered. The outmost layer of the sintered pellet was removed by polishing with silicon carbide papers and the resulting pellet with a diameter of about 10 mm served as the target for pulsed laser deposition (PLD) in the preparation of dense thin films. The respective calcination temperatures for the powders and the individual

sintering conditions for the PLD targets are listed in Table 3.1. The abbreviations for some compositions are indicated in brackets.

Table 3.1: Calcination temperatures for BSCF powders with predominant cubic perovskite phase and $\text{La}_{0.5}\text{Co}_{0.4}\text{Fe}_{0.6}\text{O}_{3-\delta}$, and sintering conditions for the PLD targets. The abbreviations for some compositions are indicated in the brackets.

Composition	Calcination T (°C)	Sintering T (°C) / t (h)	Heating / cooling rate (K/h)	Sintering atmosphere (25 ml/min)
$\text{Ba}_{0.5}\text{Sr}_{0.5}\text{Co}_{0.8}\text{Fe}_{0.2}\text{O}_{3-\delta}$	1000	1200 / 8	300 / 300	O_2
$(\text{Ba}_{0.5}\text{Sr}_{0.5})_{1.04}\text{Co}_{0.8}\text{Fe}_{0.2}\text{O}_{3-\delta}$ (BSCF5080)	1000	-	-	-
$\text{Ba}_{0.25}\text{Sr}_{0.75}\text{Co}_{0.8}\text{Fe}_{0.2}\text{O}_{3-\delta}$ (BSCF2580)	1000	1200 / 8	300 / 300	O_2
$\text{SrCo}_{0.8}\text{Fe}_{0.2}\text{O}_{3-\delta}$ (SCF)	1000	1080 / 8	120 / 60	N_2
$\text{Ba}_{0.37}\text{Sr}_{0.63}\text{Co}_{0.6}\text{Fe}_{0.4}\text{O}_{3-\delta}$	1130	-	-	-
$\text{Ba}_{0.75}\text{Sr}_{0.25}\text{Co}_{0.4}\text{Fe}_{0.6}\text{O}_{3-\delta}$	1000	-	-	-
$\text{Ba}_{0.5}\text{Sr}_{0.5}\text{Co}_{0.4}\text{Fe}_{0.6}\text{O}_{3-\delta}$ (BSCF5040)	1000	1200 / 8	120 / 60	N_2
$\text{Ba}_{0.45}\text{Sr}_{0.5}\text{Co}_{0.4}\text{Fe}_{0.6}\text{O}_{3-\delta}$	1000	-	-	-
$\text{Ba}_{0.25}\text{Sr}_{0.75}\text{Co}_{0.4}\text{Fe}_{0.6}\text{O}_{3-\delta}$	1100	-	-	-
$\text{SrCo}_{0.4}\text{Fe}_{0.6}\text{O}_{3-\delta}$	1200	-	-	-
$\text{Ba}_{0.5}\text{Sr}_{0.5}\text{FeO}_{3-\delta}$ (BSF)	1100	1200 / 8	120 / 60	N_2
$\text{Ba}_{0.25}\text{Sr}_{0.75}\text{FeO}_{3-\delta}$	1180	-	-	-
$\text{SrFeO}_{3-\delta}$ (SF)	1000	1250 / 6	200 / 30	O_2
$\text{La}_{0.5}\text{Co}_{0.4}\text{Fe}_{0.6}\text{O}_{3-\delta}$	1100	1150 / 4	120 / 60	O_2

For the pellets serving as PLD targets, the relative density of about 90 % was satisfying. However, in the case of the pellets used in conductivity relaxation measurements, cracks and pores still present at densities around 90 % were detrimental. A lot of effort was made to avoid the cracks and increase the relative density by the variation of the sintering conditions including the careful choice of the sintering temperature and time, the heating and cooling rate (60 K/h to 300 K/h) and the sintering atmosphere (O_2 , N_2 or vacuum). Because Sr-deficiency was shown to decrease the sintering rate of $\text{SrFeO}_{3-\delta}$ [56], A-site excess $(\text{Ba}_{0.5}\text{Sr}_{0.5})_{1.04}\text{Co}_{0.8}\text{Fe}_{0.2}\text{O}_{3-\delta}$ powder was therefore employed for improving the sinterability. The absolute density of 5.25 g/cm³ and a relative density of 94.7 % (estimated with the lattice constant from X-ray diffraction measurements assuming $\delta = 0.5$) was obtained for this powder at 1125 °C for 12 h with the respective heating and cooling rates of 120 K/h and 60 K/h under vacuum of about 250 Pa. Hot-pressing was another appealing choice, but the selection of proper dies was tricky. Glass (for hot iso-

static pressing) or Al_2O_3 dies may react with the powder and the reducing condition of carbon dies may decompose the powder. The A-site excess $(\text{Ba}_{0.5}\text{Sr}_{0.5})_{1.04}\text{Co}_{0.8}\text{Fe}_{0.2}\text{O}_{3-\delta}$ powder was first kept at 800 °C in N_2 for 1 h to adjust the oxygen nonstoichiometry and cooled down to room temperature. The powder was then uniaxially hot-pressed in an Al_2O_3 die under a pressure of 0.038 GPa at 1100 °C for 5 h with a high heating rate of 20 K/min and a low cooling rate of 1 K/min. The high heating rate avoided severe reaction between the powder and the Al_2O_3 die. In this way, a high absolute density of 5.43 g/cm³ and a relative density of 98 % was achieved.

For the study of the electrode/electrolyte reactivity, in addition to BSCF5080, 10 mol % Gd-doped CeO_2 (CGO) and commercially available $\text{La}_{0.6}\text{Sr}_{0.4}\text{Co}_{0.8}\text{Fe}_{0.2}\text{O}_{3-\delta}$ (LSCF6080, HITEC Materials, Germany) and 8 mol % Y_2O_3 - ZrO_2 (YSZ, TOSOH, Japan) were used. CGO was coprecipitated from $\text{Ce}(\text{NO}_3)_3 \cdot 6\text{H}_2\text{O}$ and $\text{Gd}(\text{NO}_3)_3 \cdot 6\text{H}_2\text{O}$ in aqueous ammonia solution. The powder was dried at 150 °C overnight and calcined at 800 °C for 30 minutes. The CGO powder after the calcination had a similar grain size as the YSZ powder which is about 20 nm estimated from the width of the X-ray diffraction (XRD) peaks with the Scherrer equation.

3.1.2 Thin film deposition by pulsed laser deposition

100 nm thin films used for the patterning into microelectrodes with various cation compositions and 300 nm $\text{Ba}_{0.5}\text{Sr}_{0.5}\text{Co}_{0.8}\text{Fe}_{0.2}\text{O}_{3-\delta}$ thin films were prepared by pulsed laser deposition (PLD) from sintered pellets onto $5 \times 5 \times 0.5 \text{ mm}^3$ 9.5 mol % Y_2O_3 - ZrO_2 single crystal substrates with (100) orientation (CrysTec, Germany). The laser pulse was repeated at a frequency of 5 Hz. The pulse energy was 66 mJ and the energy density per pulse was 0.16 J/cm². Before the deposition, the target was ablated for 3 min to clean the surface. The deposition was performed under an oxygen pressure of 0.4 mbar and with the substrate heated to about 770 °C. After the deposition, the films were annealed at 650 °C for 30 minutes in 1 bar oxygen. Under these deposition conditions, the resulting films are pore-free dense films [33]. The films exhibited columnar growth (not single crystal, from SEM image shown in Fig. 3.1) with more or less pronounced texture. The films used for oxygen isotope exchange measurements were 250 nm thick and prepared in the same way on $5 \times 5 \times 0.5 \text{ mm}^3$ (100)-oriented MgO single crystal substrates (CrysTec, Germany). MgO was chosen as a substrate with extremely small oxygen diffusivity [57] and a lattice constant of 4.212 Å which allows a good match with the perovskite films. All the PLD-deposited thin films were prepared in the Technology Service Group of the Max Planck Institute for Solid State Research.

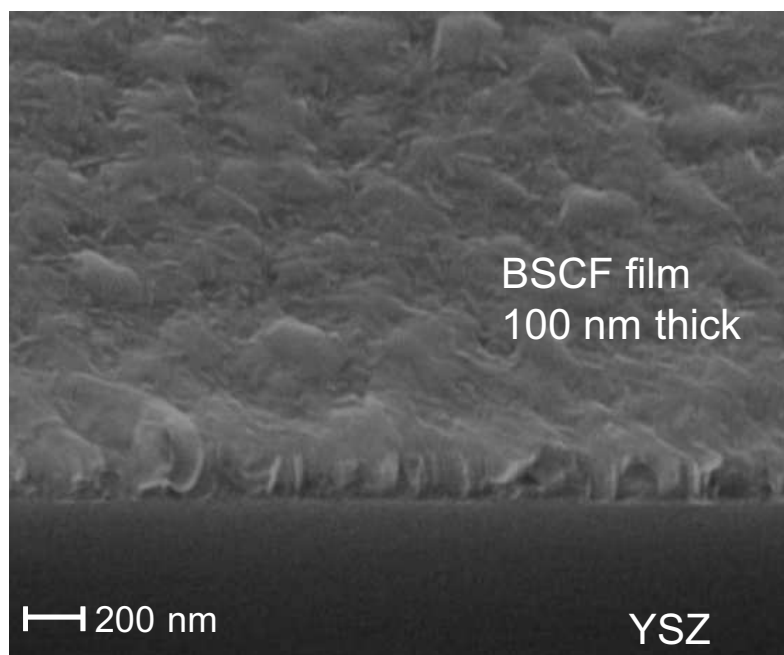


Figure 3.1: High resolution scanning electron microscopy (SEM) image of a fractured 100 nm BSCF5080 film on a YSZ single crystal, measured from a 45° perspective.

3.1.3 Microelectrode preparation by photolithography

The 100 nm films were patterned into circular microelectrodes by photolithography in the Technology Service Group of the Max Planck Institute for Solid State Research. First, a layer of photoresist was applied on top of the film by spin coating. Then the photoresist was illuminated with UV light through a photomask and the part that was exposed to the UV light was subsequently removed. In the next step, the sample was etched by Ar ion beam, removing the perovskite film in the areas not protected by the photoresist. The remaining part of the photoresist was finally removed by acetone. The photomask utilized for this thesis as well as the details of the preparation is available in Ref. [58] and the resulting microelectrodes have diameters between 20 μm and 100 μm .

3.2 Structural and compositional characterization by XRD and ICP-OES

X-ray diffraction (XRD) is a fundamental technique for the structural characterization in this thesis. It was involved in the identification of the phases of the powders, the pellets and the films, the orientations of the films and the determination of the lattice constants. Most of the XRD measurements were carried out on a Philips PW 3710 X-ray diffractometer with Cu K_{α} radiation in Bragg-Brentano geometry. The detector was a

gas proportional counter with graphite secondary monochromator. Normally 2θ covered the range of 10° to 90° with steps of 0.02° . The detection time at each step was 1 s for standard measurements and 15 s for measurements with improved signal/noise ratio.

The accurate cation concentrations of the nitrate solutions used for synthesizing the powder and the cation stoichiometry of the synthesized perovskite powder were measured by ICP-OES (Spectro Ciros CCD, Spectro Analytical Instruments, Germany) in the Analytical Chemistry Lab of the Max Planck Institute for Metals Research. When passing through the plasma, atoms and ions from the dissolved samples were excited. Radiation with characteristic wavelength for each element was released during the relaxation. By comparing the measured intensity of the radiation with standards, the concentration of the corresponding element was determined with high accuracy.

3.3 Differential scanning calorimetry

Differential scanning calorimetry (DSC) was employed to determine the oxidation enthalpies on powder samples (ca. 100 mg) in alumina crucibles from isothermal $P(\text{O}_2)$ changes in a Tian-Calvet calorimeter (Setaram DSC121, gas flow rate 10 ml/min). Molar oxidation enthalpies ΔH_{ox} were calculated from the integrated heat flow peaks and the respective changes $\Delta\delta$ in oxygen stoichiometry obtained from thermogravimetry. ΔH_{ox} values from oxidation and reduction steps were identical within error bars. The determination of calorimetric ΔH_{ox} was carried out by T. Neumaier during her summer internship at the Max Planck Institute for Solid State Research.

3.4 Determination of oxygen nonstoichiometry

As mentioned in section 2.3.3, the accurate determination of the absolute values of the oxygen nonstoichiometry δ is difficult. The difficulty comes from the limitations of different methods, e. g., in the case of thermogravimetric analysis it is difficult to prove the final products after hydrogen reduction really have the assumed well-defined composition. As a result, cross-checking with different methods is necessary.

3.4.1 Thermogravimetric analysis

The absolute δ values at 600°C and $P(\text{O}_2) = 10^{-3}$ bar were first determined from thermogravimetric analysis (STA449, Netzsch, Germany) and this method was also employed to determine the changes of the oxygen nonstoichiometry $\Delta\delta$. In all thermogravimetric analysis, the total gas flow rate was 50 ml/min and different $P(\text{O}_2)$ was controlled by N_2

and O₂ mixing by mass flow controllers. The “buoyancy” effect of the gas was corrected by subtracting the mass change measured with an empty alumina crucible under the same experimental conditions from the mass change measured with the sample.

$\Delta\delta$ upon temperature changes at certain $P(\text{O}_2)$ was determined in such a way: the powder was heated up to 1000 °C and equilibrated for 30 min. In this way, changes due to water and carbonate were excluded if there had been any in the powder. The powder was then slowly cooled down to 250 °C and heated up again to 1000 °C to check the reproducibility and the validity of the heating and cooling rates. The detailed temperature program (with lower heating rates at lower temperatures to ensure gas-solid equilibration) is illustrated in Fig. 3.2. In the next step, $\Delta\delta$ upon $P(\text{O}_2)$ changes at 600 °C was determined and combining with $\Delta\delta$ upon temperature changes, $\Delta\delta$ upon $P(\text{O}_2)$ changes in the temperature range of 250 °C and 1000 °C was obtained.

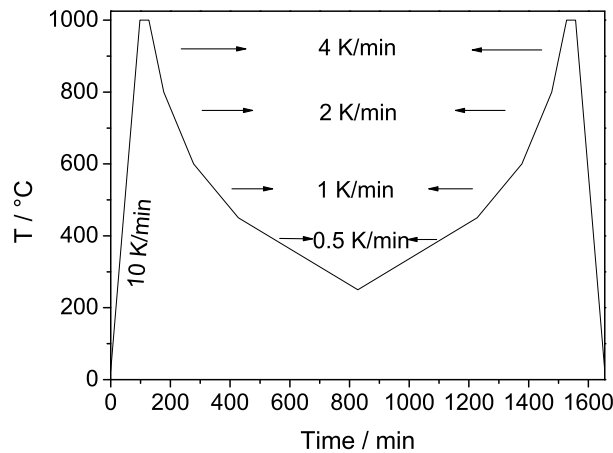


Figure 3.2: Temperature program in the thermogravimetric analysis to determine $\Delta\delta$ at certain $P(\text{O}_2)$.

The absolute δ values from thermogravimetric analysis were determined by thermogravimetric reduction of the oxides equilibrated at 600 °C and $P(\text{O}_2) = 10^{-3}$ bar to BaO, SrO, Co and Fe in 8 % H₂ in N₂ at 1000 °C. XRD measurements of the reaction products sealed in a capillary confirmed the existence of BaO, Co and Fe while the reduction products from Sr were not directly detected.

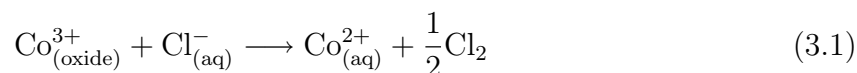
3.4.2 Chemical reaction

The absolute values from the thermogravimetric analysis were confirmed by the ones determined from the chemical reaction method.

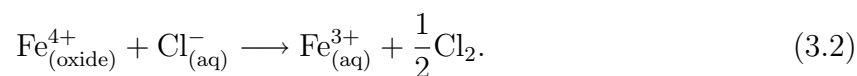
A sintered BSCF pellet was first equilibrated at 600 °C and $P(\text{O}_2) = 10^{-3}$ bar, and subsequently quenched to room temperature. The outmost layer of the pellet where

incorporation of oxygen during quenching might take place was removed. The remaining part of the pellet was ground to powder which was used for the chemical reaction.

The determination of δ by chemical reaction relied on the determination of the oxidation state of the B-site ions in BSCF. The stable oxidation states of Co ions are 2+ and 3+ and that of Fe ions are 3+ and 4+ in the oxide. When the powder was dissolved in diluted HCl (37 % HCl 1:5 volumetrically diluted with distilled water), the following reactions took place:



and/or



By determining the amount of Cl_2 generated, it is possible to determine the oxidation states of B-site ions and calculate the corresponding δ .

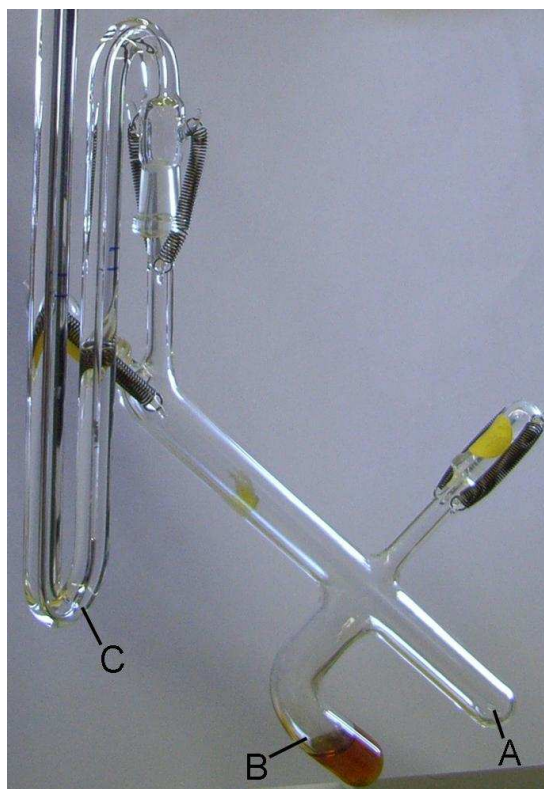


Figure 3.3: Experimental setup for determining the absolute δ values by chemical reaction. The HCl solution and the powder was separately transferred into region A and B before the reaction started. The HCl solution was poured into region B and reacted with the powder there by tilting the whole setup. Capillary tube C was filled with Hg as an indicator for the built-up pressure.

The amount of Cl_2 was determined volumetrically with the setup shown in Fig. 3.3. The HCl solution and the powder were separately transferred into region A and B before

the reaction started. The reaction tube was then connected to capillary tube C filled with Hg and sealed. The whole setup was then tilted so that the HCl solution from region A flew into region B and reacted with the powder as depicted in the figure. The reaction was accelerated by heating the tube with a lighter if necessary. From the built-up pressure in the capillary and the volume of the reaction tube (determined by filling the tube with ethanol), the amount of Cl_2 as well as δ was calculated.

There was, however, a certain amount of Cl_2 from the reaction dissolved in the HCl solution. To determine the dissolved amount, the volume of the HCl solution was kept constant as 1 ml and various amounts of powder were dissolved in the solution. The amount of dissolved Cl_2 was then equal to the absolute value of the amount of “generated” Cl_2 extrapolated to 0 mg powder.

The validity of this method was proved by measurements on samples with known oxygen stoichiometry ($\text{SrFeO}_{3-\delta}$ prepared by high oxygen pressure treatment (see Ref. [59]), $\delta \approx 0$).

3.5 Microelectrode impedance spectroscopy

For the measurements of impedance spectroscopy on the microelectrodes on YSZ single crystals, silver paste (Leitsilber 6200/0007, Oegussa, Austria) was applied to the back side of the YSZ single crystal as an extended porous counter electrode which connected the sample to a silver foil and also ensured good thermal contact to the $6 \times 6 \times 0.53 \text{ mm}^3$ sapphire disc at the bottom. This sample was then placed in a heating stage (Linkam, UK) enclosed in a vacuum-tight chamber (VACOM, Germany). Pt/Ir needles (Moser Company, USA) were used to contact to individual microelectrodes and the silver counter electrode. Impedance spectra were measured with an Alpha High Resolution Dielectric Analyser combined with a POT/GAL 15V 10A Electrochemical Impedance Test Interface (Novocontrol, Germany). The setup is shown schematically in Fig. 3.4.

An ac amplitude of 10 mV was used for most of the impedance measurements. This value has been shown to lie within the linear regime of the current-voltage response of the samples [58] (ideally, the corresponding energy, 10 meV, should be $\leq k_{\text{B}}T$ at the measurement temperature). It was also occasionally increased to 15 mV or 20 mV when the data quality was poor. The impedance spectra typically covered a frequency range of 10^{-2} to 10^6 Hz which was sometimes extended to lower frequency to achieve reliable data of the low frequency semicircle.

For accurate determination of the temperature dependence, the determination of the actual temperature of the microelectrodes is crucial. In a previous work, when the sample

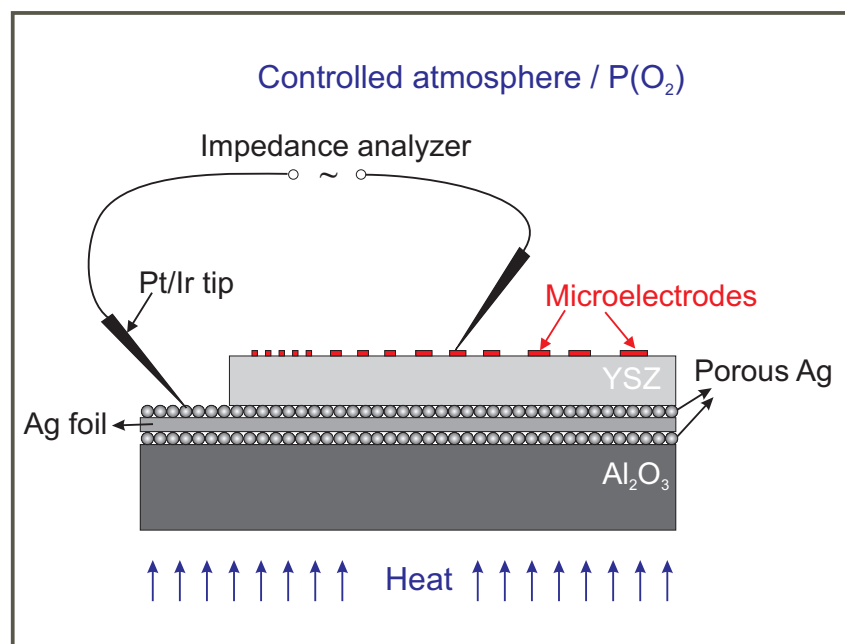


Figure 3.4: Schematic experimental setup for microelectrode impedance spectroscopy.

was placed on top of a gold piece sticking out of the heated crucible, this was done by a combination of three methods [58]. In this thesis, the whole sample sat inside the heating stage. Besides, all measurements were carried out in the closed chamber which further increased the stability of the sample temperature. As a result, only a direct contact measurement was used to determine the actual sample temperature. For this purpose, a sample analogous to the real sample except the microelectrodes was employed. A thermocouple with a diameter of 0.002 inch (Omega Engineering, Inc) was connected to the surface of the YSZ crystal by silver paste. The nominal temperature of the furnace that is necessary to reach the desired actual temperature of the sample was therefore determined under conditions analogous to the real measurement: with 200 ml/min gas flow-rate in the closed chamber with cooling water flowing through the bottom of the heating stage. The temperature calibration covered the temperature range of 500 °C to 800 °C while the temperature dependence measurements were generally conducted in the temperature range of 500 °C to 750 °C.

According to the study in Ref. [60] and from this work (section 4.2.2), the presence of CO₂ and/or H₂O could influence the performance of the cathode. To eliminate such influence, the oxygen partial pressure ($P(\text{O}_2)$) was always adjusted by a mixture of O₂ and N₂. For the temperature dependence measurements, the chamber was flushed with N₂ and subsequently evacuated to lower than 2 torr. This was repeated for three times and then the chamber was filled with O₂/N₂ mixture with $P(\text{O}_2) = 0.2$ bar. In the case of

the oxygen partial pressure dependence measurements, $P(\text{O}_2)$ was adjusted in the range of 10^{-4} to 1 bar. The exact $P(\text{O}_2)$ at the gas outlet of the chamber was indicated by a Rapidox 2100 Oxygen Analyzer (Cambridge Sensortec, UK).

Degradation, which has been referred to the slow increase of the absolute values of the surface resistance when the sample is kept at high temperatures for long time [58], also happened for the samples studied in this thesis. Therefore a general measurement routine for each sample was followed to ensure the comparability of data from different samples. At the beginning, average resistance values were measured on at least ten $60 \mu\text{m}$ microelectrodes at $750 \text{ }^\circ\text{C}$ and $P(\text{O}_2) = 0.2 \text{ bar}$. The temperature dependence was recorded immediately afterwards on a $100 \mu\text{m}$ microelectrode. Impedance spectra were recorded at each temperature when the sample was cooled from $750 \text{ }^\circ\text{C}$ to $500 \text{ }^\circ\text{C}$ in steps of $25 \text{ }^\circ\text{C}$. In order to check and correct for the influence of the degradation on the determination of the activation energy, the sample was subsequently measured during heating up to $750 \text{ }^\circ\text{C}$ in steps of $50 \text{ }^\circ\text{C}$. The next measurements were carried out under different $P(\text{O}_2)$ on another $100 \mu\text{m}$ microelectrode at $700 \text{ }^\circ\text{C}$, starting from around 10^{-4} bar to around 1 bar in steps of one order of magnitude. For the degradation effect correction, one impedance spectrum was measured again at a lower $P(\text{O}_2)$ (10^{-4} or 0.2 bar) in the end.

The effects of dc bias on the microelectrodes' resistance has been studied in the following way: First, a certain dc bias was applied on a microelectrode for two minutes. Followed by the application of the dc bias, an impedance spectrum was recorded on the microelectrode with the same dc bias superimposed onto the ac signal. After about two minutes of relaxation without dc bias, another impedance spectrum was recorded to check for any irreversible changes caused by the applied dc bias. The cathodic bias corresponded to a negative potential applied at the microelectrode compared with the counter electrode, i. e., net oxygen incorporation at the microelectrode surface. Under the cathodic bias, the microelectrodes were under reducing conditions. The measurements for cathodic bias and anodic bias were carried out on two separate $80 \mu\text{m}$ microelectrodes at $650 \text{ }^\circ\text{C}$ and $P(\text{O}_2) = 0.2 \text{ bar}$. Due to the much larger extension of the counterelectrode, the applied bias essentially dropped over the oxygen surface incorporation reaction. Thus no reference electrode was required to measure the actual electrode overpotential [33]. Only if the resistance of the oxygen surface incorporation reaction R_s was approximately equal to the YSZ bulk resistance R_b and/or the resistance R_i corresponding to the ion transfer through BSCF/YSZ interface, corrections might become necessary.

3.6 Conductivity relaxation experiments

In a conductivity relaxation experiment, the time-dependent variation of the conductivity of the sample upon a change of $P(\text{O}_2)$ was recorded and this was used to extract the surface exchange rate constant (k) and the oxygen diffusion coefficient (D). A $3.15 \times 3.15 \times 8.30$ mm³ cuboid was cut out of the sintered $\text{Ba}_{0.5}\text{Sr}_{0.5}\text{Co}_{0.8}\text{Fe}_{0.2}\text{O}_{3-\delta}$ pellet with the relative density of 94.7 % for the conductivity relaxation experiments. The setup is schematically shown in Fig. 3.5a. The cuboid was placed in a quartz sample holder and tube. $P(\text{O}_2)$ was adjusted with a gas mixture of N_2 and O_2 mixing by mass flow controllers passing through the tube with the rate of 100 ml/min. The exact $P(\text{O}_2)$ was monitored with a Rapidox 2100 Oxygen Analyzer (Cambridge Sensortec, UK) at the gas outlet. The time to reach 80 % of a $P(\text{O}_2)$ change was estimated to be about 2-3 min. The temperature of the sample was indicated by a thermocouple close to it and the thermocouple was inserted into the tube through “a” in Fig. 3.5a. The $P(\text{O}_2)$ dependence was measured at 600 °C by changing the $P(\text{O}_2)$ stepwise by a factor of about 3. The temperature dependence was measured by switching $P(\text{O}_2)$ between 0.3 and 1 bar (the $P(\text{O}_2)$ step has to be sufficiently small in order to allow the usual analysis within the linear irreversible thermodynamics treatment).

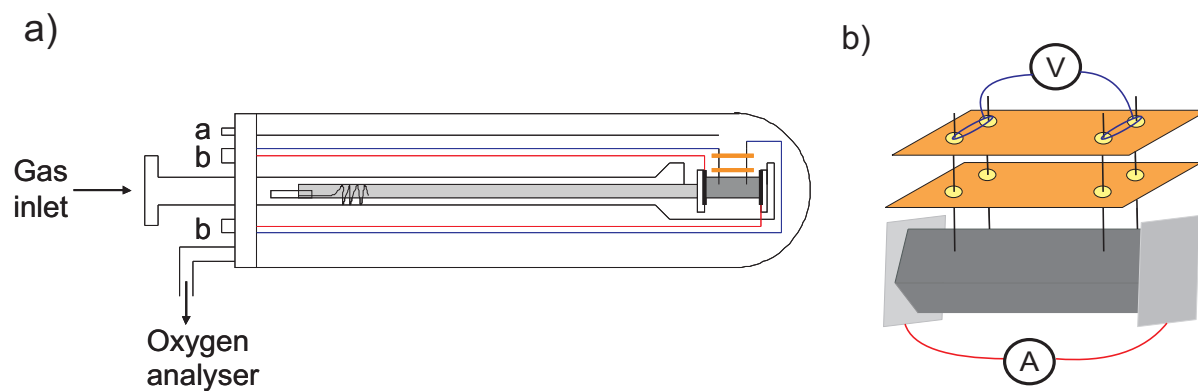


Figure 3.5: Schematic experimental setup for conductivity relaxation measurements. a) The measurement apparatus; b) Details of the wire connections.

In order to remove contributions from electrode resistance, a 4-point arrangement was used in the measurements of the dc conductivity. Pt foils, through which current was applied to the sample, were connected to the cuboid at the ends with Pt paste as illustrated in Fig. 3.5b. To assure the contact between the sample and the wires for the voltage measurements, a special design was applied as depicted in Fig. 3.5b. Each wire was connected to two Pt/Ir needles whose positions were defined by the Al_2O_3 plates they passed through. The distance between the two inner voltage probes, 4 mm in this case,

was therefore defined by the distance between the holes in the Al_2O_3 plates. The four Pt wires for current and voltage measurements were connected to feedthroughs “b” in Fig. 3.5a.

For each resistance value acquired, four measurements with currents of different magnitudes and polarizations (-20 mA, -10 mA, 10 mA, 20 mA) were carried out. The resistance was then determined from the linear regression of the resulting voltage-current curve. The current was applied through a Keithley 220 current source and the voltage was measured with a Keithley 617 multimeter (Keithley Instruments, USA) controlled by the measurement software programmed in “Asyst”.

3.7 Oxygen isotope exchange and SIMS measurements

Due to the difficulty in sintering dense BSCF pellets and the evaluation of data from conductivity relaxation experiments (see section 4.4 for details), oxygen isotope exchange and SIMS analysis on dense thin films were employed to obtain reliable data on oxygen diffusion coefficient D^* and surface exchange rate constant k^* .

Oxygen isotope exchange followed by secondary ion mass spectrometry (SIMS) analysis is an effective way for studying the oxygen transport in oxides [61,62]. Conventional depth profiling complemented by the linescanning mode enables the accurate determination of tracer diffusion coefficient and surface exchange rate constant over a broad range [63]. In most of the previous studies, this method was applied to sintered samples that had similar size in three dimensions. In this thesis, it was applied to dense thin films and thus avoided the inaccuracy caused by the pores and cracks in the sintered samples. A gas-tight cover layer extended the range of the measurable diffusion length. The feasibility of such a method for measuring diffusion parallel to the film direction was demonstrated in Ref. [64] for $\text{La}_2\text{NiO}_{4+\delta}$.

For the oxygen isotope exchange, a 300 nm thick gas-tight Au layer was deposited by evaporation on the BSCF film in the Technology Service Group of the Max Planck Institute for Solid State Research (Fig. 3.6a) and post-annealed for 4 h at 400 °C in air to increase adhesion. In order to enable oxygen isotope exchange between BSCF and the atmosphere, a cut about 30 μm wide with relatively sharp edges was created through the gold and BSCF layers with an automatic dicing saw (DAD321, Disco, Japan) which can operate without lubricant (Fig. 3.6b). The gas-tightness of the Au layer and the uniformity of the isotope distribution perpendicular to the plane of the diffusion in the film was confirmed by depth profiling through the Au and BSCF layers.

Before the isotope exchange annealing, the samples were pre-annealed in O_2 with nor-

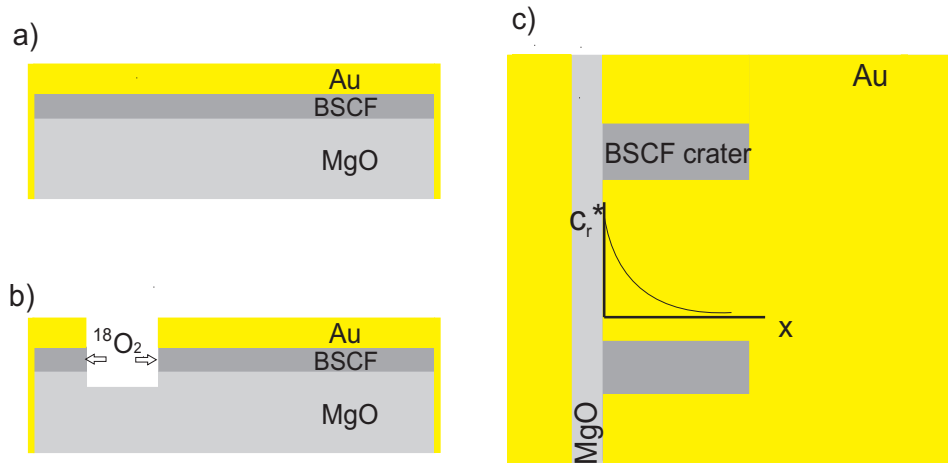


Figure 3.6: Steps in the isotope exchange and SIMS measurements: a) Deposition of a gas-tight Au layer on top of the BSCF dense film and post-annealing. b) A cut through the Au and BSCF layers to enable the isotope exchange between BSCF and the atmosphere. c) Top view of the sample with BSCF craters for measuring line scans as well as an schematic profile of the normalized ^{18}O concentration c_r^* versus the distance from the cut x (c_r^* is defined as $[c^*(x, t) - c_{\text{bg}}^*]/(c_g^* - c_{\text{bg}}^*)$, where c_{bg}^* and c_g^* refer to the background and annealing gas isotope fraction, $c^*(x, t)$ is the ^{18}O fraction in the film).

mal isotopic abundance (“technical quality”; high purity oxygen 5.0 or 6.0 was found to contain an increased amount of ^{18}O) at least ten times longer than the tracer annealing duration and then quenched to room temperature. The subsequent tracer exchange took place at the same temperature and $P(\text{O}_2)$ as the pre-annealing in $^{18}\text{O}_2$ enriched atmosphere (99 % $^{18}\text{O}_2$, measured by a BALZERS Prisma quadrupole mass spectrometer at the beginning and the end of each isotope exchange annealing) which excluded a $P(\text{O}_2)$ gradient acting as additional driving force. For the exact tracer annealing time the duration of heating up and cooling down the sample was recorded and also taken into account in the analysis. The choice of the annealing temperature and time assured the accurate determination of both D^* and k^* simultaneously according to the conditions explained in Ref. [63] in detail.

The ^{18}O concentration profile was analyzed by time-of-flight secondary ion mass spectrometry (TOF-SIMS IV, ION-TOF, Germany). For the determination of the isotope profile, a $500 \mu\text{m} \times 1500 \mu\text{m}$ crater was created by sputtering away the gold layer as well as half of the BSCF layer (Fig. 3.6c) with a 2 keV Cs^+ ion beam. Approximately in the middle of the BSCF layer, line scans with $10 \mu\text{m}$ steps were carried out. In every step, the surface layer was first briefly sputtered away by 1 keV Cs^+ ions to ensure a clean surface and then analyzed with a 25 keV Ga^+ primary ion beam in burst mode (a long pulse was cut into 8 pulses). The negatively charged secondary O^- ions were chosen to be analyzed

due to their high yields.

To estimate the experimental error, usually two line scans were measured on each sample at different positions and analyzed independently. The starting point of the ^{18}O concentration profile in each line scan was determined by combining the optical images during the measurement and the values of ^{18}O concentration c^* ($c^* = I(^{18}\text{O}^-)/(I(^{18}\text{O}^-)+I(^{16}\text{O}^-))$) where $I(^{18}\text{O}^-)$ and $I(^{16}\text{O}^-)$ are secondary ion intensities of $^{18}\text{O}^-$ and $^{16}\text{O}^-$). A possible variation of $10\ \mu\text{m}$ was taken into account in the fitting procedure. To check the consistency of the results, isotope exchanges at $500\ ^\circ\text{C}$ were carried out on two samples for different exchange time and both data were included in the estimation of the error bars.

Due to the high intensity of $^{16}\text{O}^-$ and the dead time effect of the detector (the intensity of the first peak was so high that the detector was not able to register all the ions from the subsequent bursts), its peaks from different bursts were not of equal intensity and as a result only the Poisson corrected intensity of the first peak was used for calculating. When $^{18}\text{O}^-$ peaks did not suffer from the dead time effect, the corrected total intensity of all $^{18}\text{O}^-$ peaks was used. When $^{18}\text{O}^-$ peaks also suffered from the dead time effect, only the intensity of the first $^{18}\text{O}^-$ peak was used. [65]

The background isotope fraction c_{bg}^* was generally close to the natural abundance of ^{18}O , which is 0.2 %. For some of the line scans, c_{bg}^* was slightly higher (e. g., 0.3 % for $\text{Ba}_{0.5}\text{Sr}_{0.5}\text{Co}_{0.8}\text{Fe}_{0.2}\text{O}_{3-\delta}$ or 0.8 % for $\text{Ba}_{0.5}\text{Sr}_{0.5}\text{FeO}_{3-\delta}$ and $\text{SrFeO}_{3-\delta}$), but this will not significantly affect the D^* and k^* values which are mainly fitted from the part of the profile with higher c^* . We do not expect accelerated diffusion along grain boundaries in these materials. With the accelerated diffusion along grain boundaries, there is a “tail” in the c_r^* - x curve and thus the high precision of c_{bg}^* close to 0.2 % is decisive for the determination of grain boundary diffusivity.

The reliability of the acquired ^{18}O concentration profile also depends on how much ^{18}O was lost from BSCF to the MgO substrate. Depth profiling through BSCF into the MgO substrate was not able to supply a definite answer to this question since the Cs^+ ion beam slightly bombarded the ^{18}O from BSCF into MgO. As an alternative, isotope exchange was carried out on a $300\ \text{nm}$ $\text{Ba}_{0.5}\text{Sr}_{0.5}\text{Co}_{0.8}\text{Fe}_{0.2}\text{O}_{3-\delta}$ film on a $0.5\ \text{mm}$ thick MgO substrate without Au cover layer at $600\ ^\circ\text{C}$ and $P(\text{O}_2) = 500\ \text{mbar}$ for 20 min which resulted in a high ^{18}O fraction similar to the isotope concentration in the gas phase (99 %) in the whole film. The sample was glued to an organic substrate at the BSCF5080 side and the thickness of the MgO layer was first uniformly reduced by grinding to $100\ \mu\text{m}$ and then locally reduced to about 15 to $20\ \mu\text{m}$ with a grinding ball of $15\ \text{mm}$ diameter. A depth profile through the MgO layer into BSCF5080 was then recorded to evaluate the amount of ^{18}O diffused into the MgO substrate. A $300 \times 300\ \mu\text{m}^2$ crater was created and

the analysis area was $50 \times 50 \mu\text{m}^2$ in the middle of the crater. The charge compensation necessary for the insulating MgO was achieved by flooding the sample with electrons. The ^{18}O concentration c^* and the intensity of the respective ions close to the MgO/BSCF5080 interface versus sputtering time is shown in Fig. 3.7. Ideally the curves should be step functions. The resulting curves were due to the fact that the surface of the MgO layer after the thickness reduction was not parallel to the MgO/BSCF5080 interface. The C^- ions came from the organic substrate. The sputtering rate of MgO was estimated to be $0.65 \pm 0.1 \mu\text{m}/\text{h}$ by measuring the depth of a crater created under the same condition by white light interferometer. The MgO layer with increased $c^* \approx 1.5 \%$ was therefore about $1.2 \mu\text{m}$. Taking the fact that there is an angle between the sputtered surface and the MgO/BSCF5080 interface, the actual thickness of MgO layer with increased c^* was even smaller. If estimated conservatively, there was only about 6% ^{18}O diffused into MgO even at relatively high temperature and with rather high c^* in BSCF5080. Therefore the diffusion of ^{18}O into MgO did not result in obvious change of the shape of the ^{18}O concentration profile.

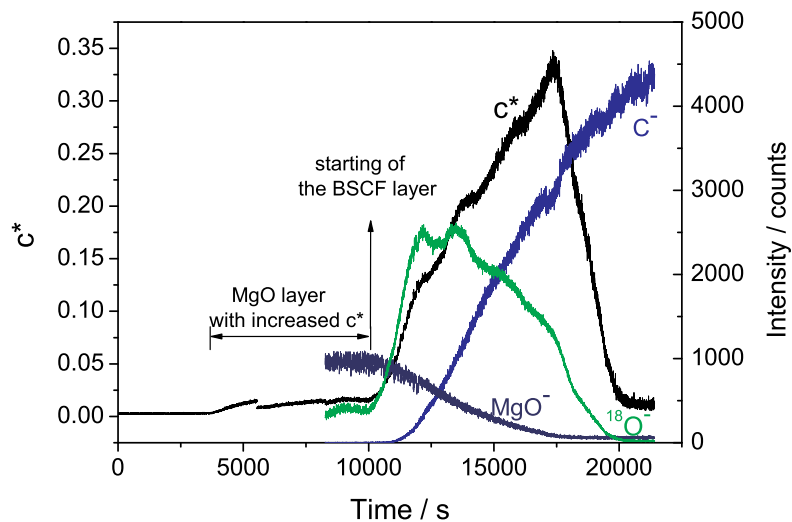


Figure 3.7: ^{18}O concentration c^* and the intensity of the respective ions close to the MgO/BSCF5080 interface versus sputtering time. The discontinuity around 5500 s came from the slight change of the analysis position.

Chapter 4

Results and discussion

4.1 Sample characterization

4.1.1 X-ray diffraction measurements

4.1.1.1 Powders

The room temperature X-ray diffractogram for $(\text{Ba}_{0.5}\text{Sr}_{0.5})_{1.04}\text{Co}_{0.8}\text{Fe}_{0.2}\text{O}_{3-\delta}$ powder is shown in Fig. 4.1 as an example of X-ray diffractograms for BSCF powders with cubic perovskite structure studied in this thesis. The peaks are indexed on the basis of a cubic perovskite phase with the space group $\text{Pm}\bar{3}\text{m}(221)$. From the powder diffraction data, the

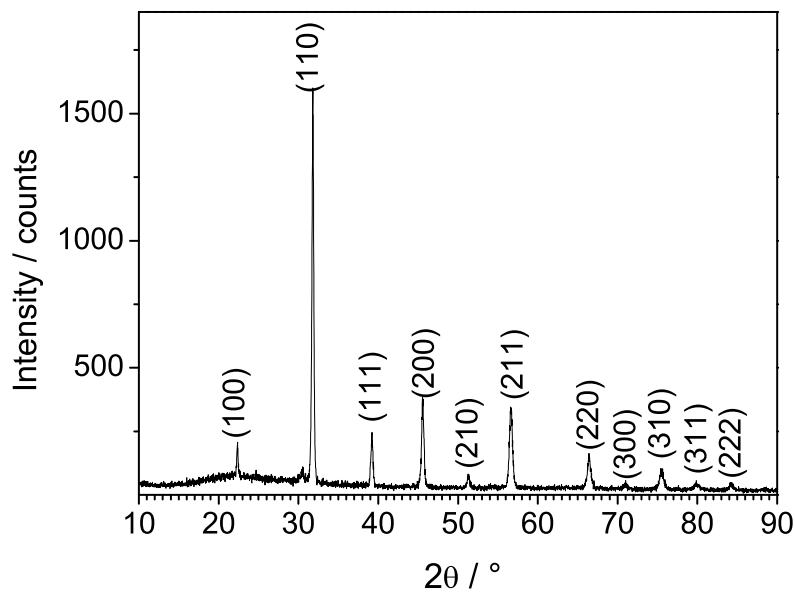


Figure 4.1: Room temperature X-ray diffractogram of $(\text{Ba}_{0.5}\text{Sr}_{0.5})_{1.04}\text{Co}_{0.8}\text{Fe}_{0.2}\text{O}_{3-\delta}$ powder calcined in air at 1000 °C for 12 h. The peaks are indexed on a basis of a cubic perovskite phase with the space group $\text{Pm}\bar{3}\text{m}(221)$.

lattice constants for the individual compositions were refined with the program TOPAS

2.1 (Bruker AXS, Germany). The variation of the lattice constant upon variation of the cation composition is depicted in Fig. 4.2. Since Ba^{2+} (1.61 Å) for the coordination number of 12 is much larger than Sr^{2+} (1.44 Å) [44], the increase of the lattice constant with increasing Ba content for a fixed Co/Fe ratio is not surprising. When the Ba/Sr ratio is fixed, the lattice constant increases slightly with increasing Co content. According to Ref. [41], this may indicate the predominant oxidation and spin state of Co and Fe ions are 3+ and high spin with the coordination number of 6.

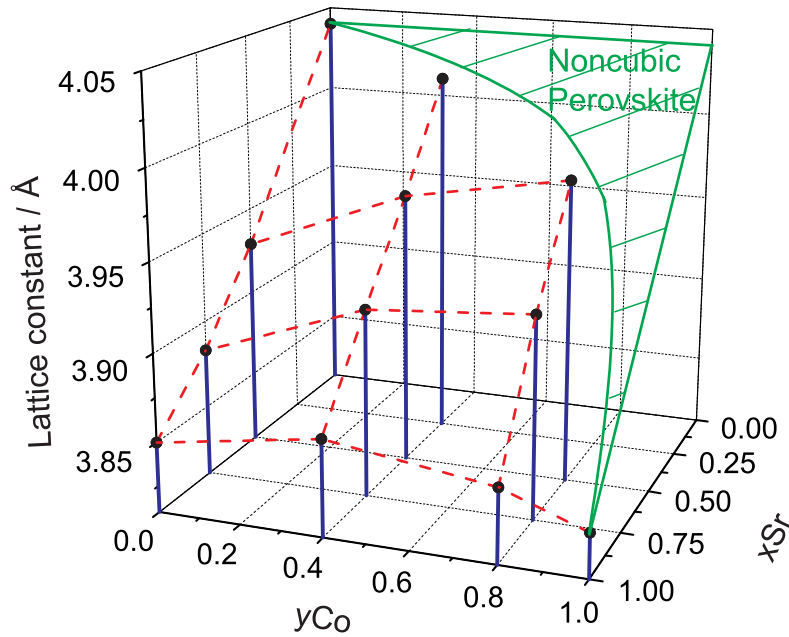


Figure 4.2: Dependence of room temperature lattice constants of cubic perovskites $\text{Ba}_{1-x}\text{Sr}_x\text{Co}_y\text{Fe}_{1-y}\text{O}_{3-\delta}$ (furnace-cooled in air) on composition. The existence range of noncubic perovskite phases is roughly estimated and indicated as the green area. Data for $\text{BaFeO}_{3-\delta}$ is estimated from Ref. [66] for cubic $\text{BaCe}_{0.05}\text{Fe}_{0.95}\text{O}_{3-\delta}$ and data for cubic SrCoO_3 is from Ref. [67].

The noncubic perovskites are favored when the Ba content is very high (corresponding to $t \gg 1$ which leads to e. g., hexagonal perovskite structure), and/or the Co content is high (the low oxidation state of Co^{2+} leads to high oxygen vacancy concentration which facilitates the formation of vacancy ordered superstructures.). It is remarkable that the BSCF with best transport properties ($x = 0.5$, $y = 0.8$ with high k and D) is located close to the stability limit of the cubic perovskite structure.

The lattice constant a depends on the oxygen nonstoichiometry δ . In the case of $\text{Ba}_{0.5}\text{Sr}_{0.5}\text{Co}_{0.8}\text{Fe}_{0.2}\text{O}_{3-\delta}$, an increase of 0.1 in δ upon a $P(\text{O}_2)$ change from 1 atm to 10^{-3} atm leads to an increase of 0.01 Å [68] which is small compared with the variation upon variation of the cation composition.

4.1.1.2 Thin films

A typical X-ray diffractogram of a 100 nm $\text{Ba}_{0.5}\text{Sr}_{0.5}\text{Co}_{0.8}\text{Fe}_{0.2}\text{O}_{3-\delta}$ thin film on a (100)-oriented YSZ single crystal is shown in Fig. 4.3a. Comparison with the diffractogram of a YSZ single crystal (Fig. 4.3b) shows that the two peaks at 34.9° and 73.6° correspond to the YSZ K_α peaks, whereas the four small peaks at 33.3° , 33.6° , 70.0° , 70.6° are artefacts from the monochromator. The remaining K_β peaks are marked in the graph. The film is strongly textured with dominant (111) orientation and no obvious peaks of secondary phases besides the cubic perovskite are observed.

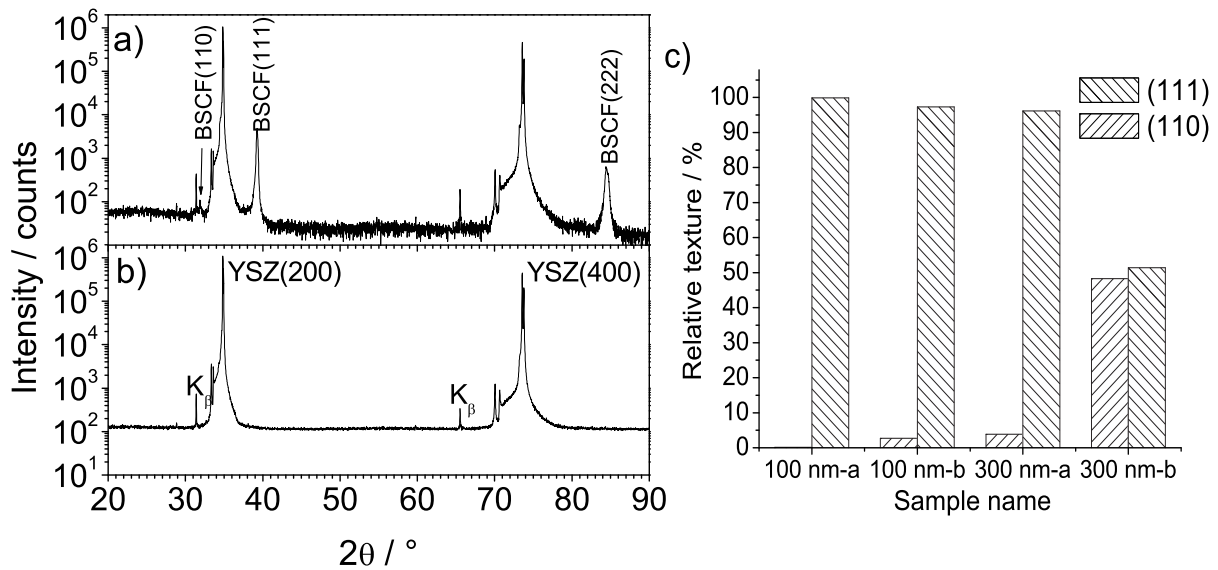


Figure 4.3: X-ray diffractograms of a) a 100 nm $\text{Ba}_{0.5}\text{Sr}_{0.5}\text{Co}_{0.8}\text{Fe}_{0.2}\text{O}_{3-\delta}$ thin film on a YSZ single crystal with (100) orientation; b) a bare YSZ single crystal with (100) orientation; c) Quantitative analysis of texture of two 100 nm and two 300 nm thick $\text{Ba}_{0.5}\text{Sr}_{0.5}\text{Co}_{0.8}\text{Fe}_{0.2}\text{O}_{3-\delta}$ films.

Since the peak widths are comparable, the ratio of peak intensity can be used to estimate the relative texture (peak areas are difficult to determine because of overlap with YSZ peaks). Due to the difference of peak intensity from different orientations in the powder diffractogram (Fig. 4.1), the intensity in the film is normalized to the intensity from the powder diffractogram and the relative texture is defined here as

$$I_r(\text{hkl}) = I_p(\text{hkl})/I_p(110) \quad (4.1)$$

$$\text{relative texture} = [I_f(\text{hkl})/I_r(\text{hkl})]/\Sigma[I_f(\text{hkl})/I_r(\text{hkl})] \quad (4.2)$$

where $I(\text{hkl})$ is the intensity of the (hkl) peak and “r”, “p” and “f” represent relative, powder and film.

The relative textures of four $\text{Ba}_{0.5}\text{Sr}_{0.5}\text{Co}_{0.8}\text{Fe}_{0.2}\text{O}_{3-\delta}$ samples are shown in Fig. 4.3c (since the relative texture of the (100) orientation is very low compared to the others, it is not included in the figure). Measurements on 100 nm thick samples (100 nm-a and 100 nm-b) from different PLD batches show a reproducible preferred (111) orientation. The 300 nm films (300 nm-a and 300 nm-b) have an inconsistent preferred orientation; the reason is not understood yet.

For films with other cation compositions, different preferred orientations are observed. It is not surprising that perovskite thin films with different cation compositions prefer different orientations [69]. Different cation composition samples have different lattice constants and therefore different misfit f relative to the substrate lattice:

$$f = [a_0(s) - a_0(f)]/a_0(f). \quad (4.3)$$

$a_0(s)$ is the lattice constant of the substrate and $a_0(f)$ is the lattice constant of the material from the powder diffraction. Since $a_0(\text{YSZ})$ (5.14 Å) is much bigger than $a_0(f)$ (3.85 to 3.98 Å) while the diagonal of the BSCF unit cell (5.4 to 5.6 Å) is comparable to the YSZ lattice constant, $a_0(\text{YSZ})/\sqrt{2}$ is taken as $a_0(s)$. The lattice of the films shrink slightly in the direction perpendicular to the surface of the substrate compared with the powders with the same composition except SF and BSF.

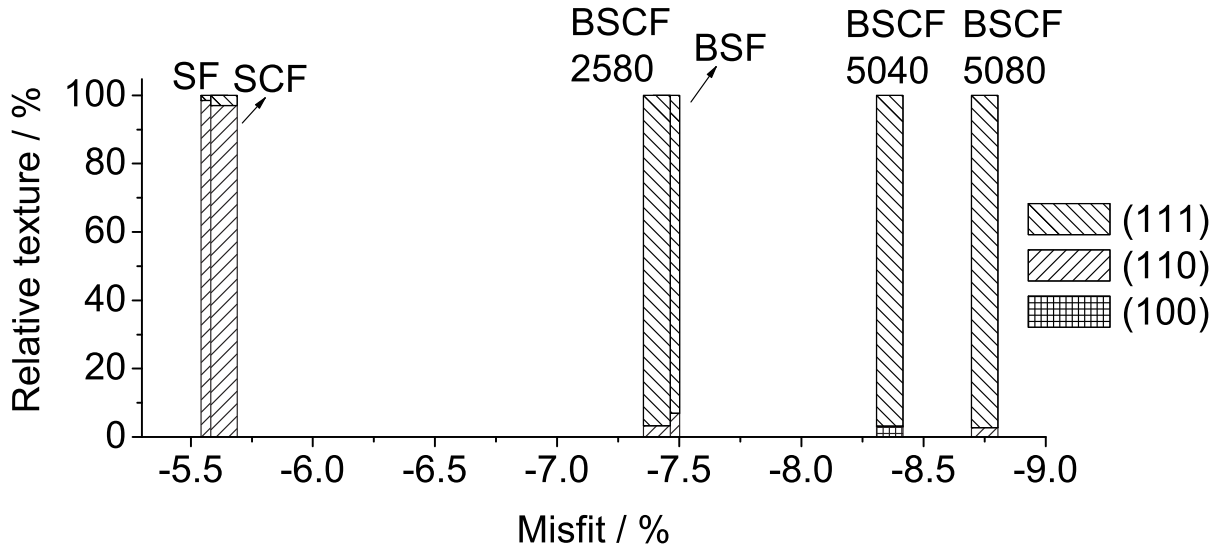


Figure 4.4: Quantitative analysis of texture versus misfit for different cation compositions (100 nm films on (100)-oriented YSZ single crystals).

Fig. 4.4 indicates that 100 nm thick BSCF films with relatively smaller misfit prefer a dominant (110) orientation while films with relatively bigger misfit have dominant (111) orientation.

For PLD-deposited $\text{La}_{0.6}\text{Sr}_{0.4}(\text{Co}_y\text{Fe}_{1-y})\text{O}_{3-\delta}$ films (100 nm and 300 nm thick) [33,58], which have a unit cell volume comparable to that of $\text{Sr}_{0.5}\text{Co}_{0.8}\text{Fe}_{0.2}\text{O}_{3-\delta}$ and $\text{SrFeO}_{3-\delta}$, predominant (110) texture was also observed. The growth process of SrRuO_3 films on (100)-oriented YSZ single crystals was investigated in detail [70,71]. There also a preferential (110) orientation of the perovskite was found.

An X-ray diffractogram of a dense 250 nm thick $\text{Ba}_{0.5}\text{Sr}_{0.5}\text{Co}_{0.8}\text{Fe}_{0.2}\text{O}_{3-\delta}$ film on a (100)-oriented MgO single crystal substrate with a gas-tight 300 nm Au cover layer after the oxygen isotope exchange experiment at 600 °C is shown in Fig. 4.5. Different from the situation of BSCF films on (100)-oriented YSZ single crystal substrates, the preferred orientation of BSCF films on (100)-oriented MgO single crystal substrates is (100) and does not show any obvious dependence on the cation composition. This is probably due to the fact that the lattice constant of MgO (4.212 Å) is close to the lattice constants of BSCFs (SCF films on (100)-oriented MgO single crystal substrates were not phase pure under the present preparation conditions).

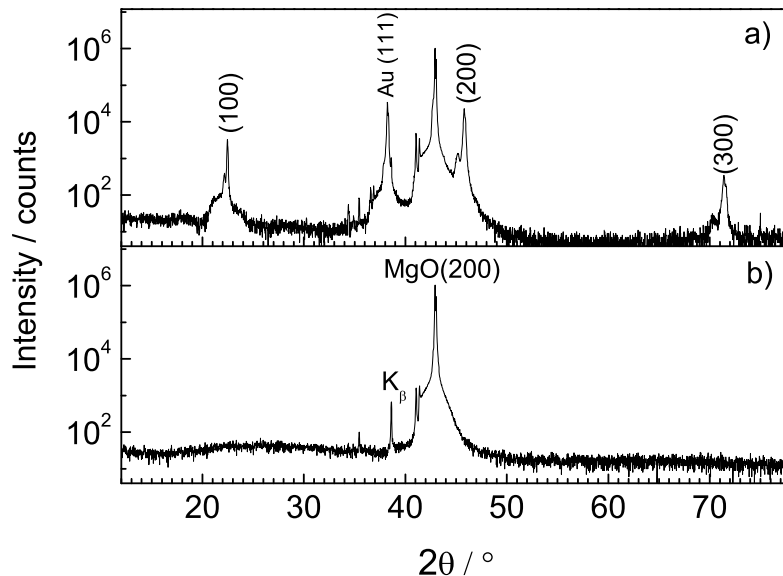


Figure 4.5: X-ray diffractograms of a) a dense 250 nm thick $\text{Ba}_{0.5}\text{Sr}_{0.5}\text{Co}_{0.8}\text{Fe}_{0.2}\text{O}_{3-\delta}$ film on a (100)-oriented MgO single crystal substrate with a gas-tight 300 nm Au cover layer after the oxygen isotope exchange experiment at 600 °C and b) the bare (100)-oriented MgO substrate.

Although the BSCF films show different preferred orientations depending on film thickness, exact cation composition and nature of substrate, they maintain under the present preparation conditions high phase purity and exhibit a highly textured structure according to the XRD measurements. Despite the macroscopic texture, the orientation of the topmost layer of the films might be different by surface reconstructions in order to keep

the surface in the lowest energy state. DFT calculations for a free-standing LaMnO_3 thin film [72,73] indicate that (100) is the energetically most preferred surface orientation, with the Mn-O-termination being more stable than La-O. These findings may be valid also for related cobaltate and ferrate perovskites such as BSCF.

4.1.2 ICP-OES measurements

The exact cation ratios of synthesized BSCF powder were analyzed by ICP-OES. The results are summarized in Table 4.1 assuming the B-site is stoichiometric (The A-site is assumed to be stoichiometric for $\text{SrCo}_{0.8}\text{Fe}_{0.2}\text{O}_{3-\delta}$). The errors from the experiment are approximately 1 %.

Table 4.1: Exact cation ratios for synthesized BSCF powder assuming B-site is stoichiometric (A-site is assumed to be stoichiometric for $\text{SrCo}_{0.8}\text{Fe}_{0.2}\text{O}_{3-\delta}$). $\text{Ba}_{0.5}\text{Sr}_{0.5}\text{Co}_{0.8}\text{Fe}_{0.2}\text{O}_{3-\delta}^*$ is the powder synthesized during the previous study [58] and $\text{Ba}_{0.5}\text{Sr}_{0.5}\text{Co}_{0.8}\text{Fe}_{0.2}\text{O}_{3-\delta}^{**}$ is the powder synthesized during the present study.

Intended composition	Composition measured by ICP-OES
$\text{Ba}_{0.5}\text{Sr}_{0.5}\text{Co}_{0.8}\text{Fe}_{0.2}\text{O}_{3-\delta}^*$	$\text{Ba}_{0.48}\text{Sr}_{0.50}\text{Co}_{0.80}\text{Fe}_{0.20}\text{O}_{3-\delta}$
$\text{Ba}_{0.5}\text{Sr}_{0.5}\text{Co}_{0.8}\text{Fe}_{0.2}\text{O}_{3-\delta}^{**}$	$\text{Ba}_{0.48}\text{Sr}_{0.51}\text{Co}_{0.81}\text{Fe}_{0.19}\text{O}_{3-\delta}$
$(\text{Ba}_{0.5}\text{Sr}_{0.5})_{1.04}\text{Co}_{0.8}\text{Fe}_{0.2}\text{O}_{3-\delta}$	$\text{Ba}_{0.49}\text{Sr}_{0.52}\text{Co}_{0.80}\text{Fe}_{0.20}\text{O}_{3-\delta}$
$\text{Ba}_{0.25}\text{Sr}_{0.75}\text{Co}_{0.8}\text{Fe}_{0.2}\text{O}_{3-\delta}$	$\text{Ba}_{0.23}\text{Sr}_{0.75}\text{Co}_{0.80}\text{Fe}_{0.20}\text{O}_{3-\delta}$
$\text{SrCo}_{0.8}\text{Fe}_{0.2}\text{O}_{3-\delta}$	$\text{SrCo}_{0.72}\text{Fe}_{0.20}\text{O}_{3-\delta}$
$\text{Ba}_{0.5}\text{Sr}_{0.5}\text{FeO}_{3-\delta}$	$\text{Ba}_{0.45}\text{Sr}_{0.49}\text{FeO}_{3-\delta}$

The $\text{Ba}_{0.5}\text{Sr}_{0.5}\text{Co}_{0.8}\text{Fe}_{0.2}\text{O}_{3-\delta}$ used for sintering the PLD target was from the previous study [58], and it has a cation composition almost identical to the powder synthesized in the present study (Table 4.1). Most of the other measurements for BSCF5080 were carried out on the nominal A-site excess $(\text{Ba}_{0.5}\text{Sr}_{0.5})_{1.04}\text{Co}_{0.8}\text{Fe}_{0.2}\text{O}_{3-\delta}$ powder which actually did not have a significant A-site excess (Table 4.1). Since the exact cation compositions of the three BSCF5080 powders are quite similar, in this thesis, both $\text{Ba}_{0.5}\text{Sr}_{0.5}\text{Co}_{0.8}\text{Fe}_{0.2}\text{O}_{3-\delta}$ and $(\text{Ba}_{0.5}\text{Sr}_{0.5})_{1.04}\text{Co}_{0.8}\text{Fe}_{0.2}\text{O}_{3-\delta}$ are referred to as BSCF5080. If not mentioned specifically, the measurements on thin films and microelectrodes were done with $\text{Ba}_{0.5}\text{Sr}_{0.5}\text{Co}_{0.8}\text{Fe}_{0.2}\text{O}_{3-\delta}$ and all the other measurements on BSCF5080 with $(\text{Ba}_{0.5}\text{Sr}_{0.5})_{1.04}\text{Co}_{0.8}\text{Fe}_{0.2}\text{O}_{3-\delta}$.

4.2 Stability of $(\text{Ba,Sr})(\text{Co,Fe})\text{O}_{3-\delta}$

As listed in chapter 1, there are several requirements for a cathode material. The studies with regard to the stability are then presented in this section.

4.2.1 Compatibility with electrolyte materials

As a potential SOFC cathode, good compatibility with the electrolyte is necessary. To check the compatibility between cathode materials and electrolyte materials, perovskite oxide cathode powders ($\text{La}_{0.6}\text{Sr}_{0.4}\text{Co}_{0.8}\text{Fe}_{0.2}\text{O}_{3-\delta}$ (LSCF6080) or $\text{Ba}_{0.5}\text{Sr}_{0.5}\text{Co}_{0.8}\text{Fe}_{0.2}\text{O}_{3-\delta}$ (BSCF5080, from the previous study)) and electrolyte powders (10 mol % Gd-doped CeO_2 (CGO) or 8 mol % $\text{Y}_2\text{O}_3\text{-ZrO}_2$ (YSZ)) were ground together in a mortar in a 1:1 molar ratio. Besides BSCF5080, the compatibility between LSCF6080 and YSZ as well as CGO were also studied to allow a direct comparison. The mixtures were then heated in air to different temperatures and kept for different dwelling time. The phases present after the temperature treatment were analyzed by X-ray diffraction. The peak areas of the newly formed phases were determined from a fitting procedure using a “split pseudo-Voigt” peak shape.

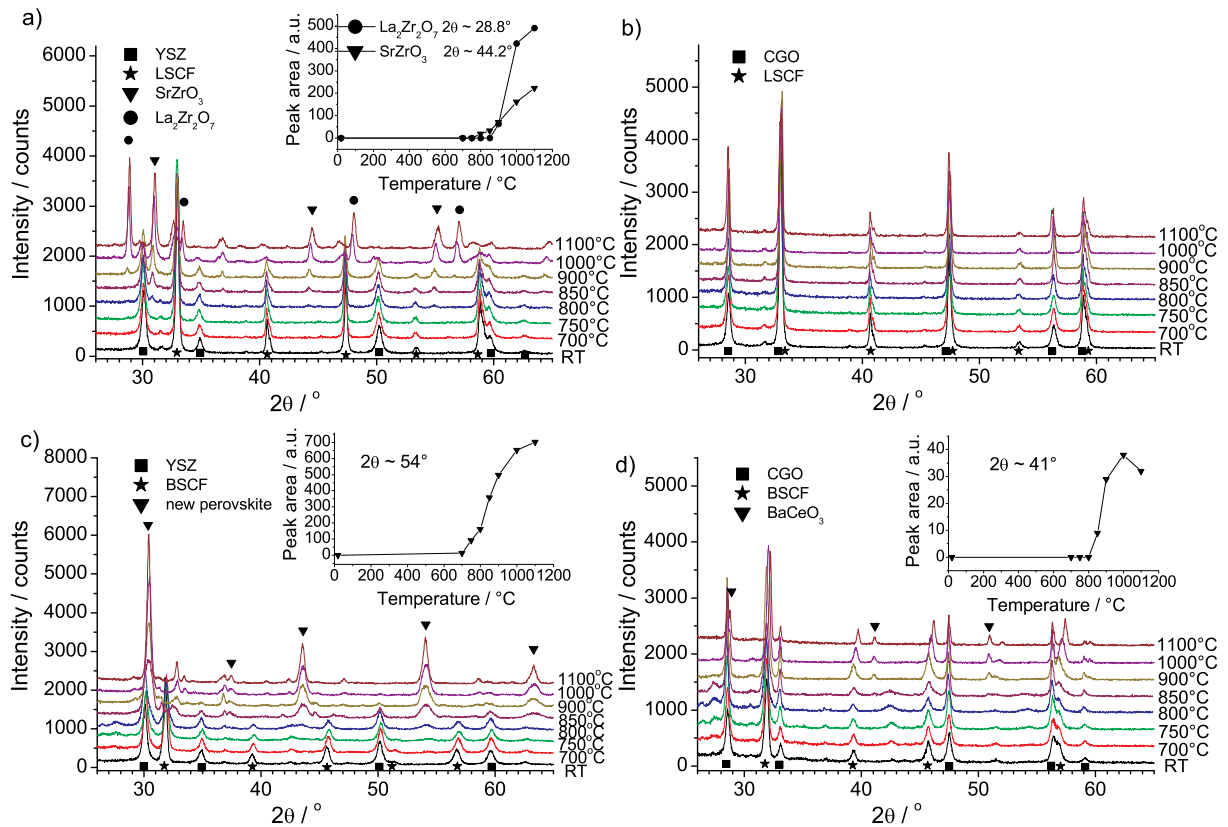


Figure 4.6: Diffractograms of powder mixtures at 25 °C and after 24 hours at the indicated temperatures in air. Symbols indicate the main phases. a) $\text{La}_{0.6}\text{Sr}_{0.4}\text{Co}_{0.8}\text{Fe}_{0.2}\text{O}_{3-\delta}$ + YSZ; b) $\text{La}_{0.6}\text{Sr}_{0.4}\text{Co}_{0.8}\text{Fe}_{0.2}\text{O}_{3-\delta}$ + CGO; c) $\text{Ba}_{0.5}\text{Sr}_{0.5}\text{Co}_{0.8}\text{Fe}_{0.2}\text{O}_{3-\delta}$ + YSZ; d) $\text{Ba}_{0.5}\text{Sr}_{0.5}\text{Co}_{0.8}\text{Fe}_{0.2}\text{O}_{3-\delta}$ + CGO. Insets: quantitative analysis of peak areas of the reaction products.

Interfacial reactions between YSZ and $(\text{La}_x\text{Sr}_{1-x})(\text{Co}_y\text{Fe}_{1-y})\text{O}_{3-\delta}$ at SOFC manufac-

ture and operation temperatures are reported in the literature (see e. g., [74]), and a ceria buffer layer has proven to prevent these reactions. The diffractograms in Fig. 4.6a show complete decomposition of LSCF6080 in contact with YSZ which begins with the formation of SrZrO_3 at 800 °C followed by the $\text{La}_2\text{Zr}_2\text{O}_7$ pyrochlore formation at 900 °C. The SrZrO_3 formation at 850 °C (Fig. 4.7a) seems to slow down as soon as a certain amount is formed although the amounts of initial phases have hardly decreased. Pyrochlore formation is not observed at 850 °C even after 48 h. Interfacial reactions between LSCF6080 and CGO are negligible even at 1100 °C (Fig. 4.6b).

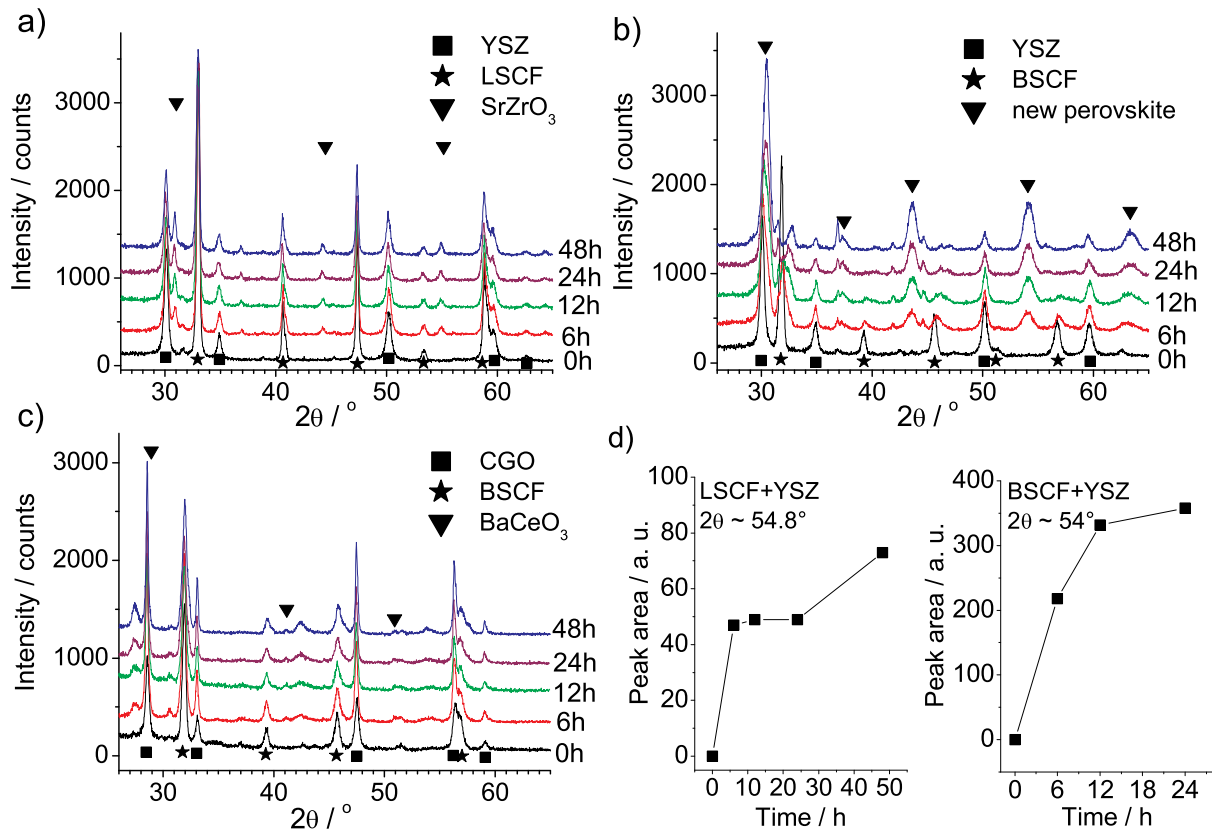


Figure 4.7: Diffractograms of powder mixtures at 25 °C and upon annealing at 850 °C in air for the indicated time intervals. Symbols indicate the main phases. a) $\text{La}_{0.6}\text{Sr}_{0.4}\text{Co}_{0.8}\text{Fe}_{0.2}\text{O}_{3-\delta}$ + YSZ; b) $\text{Ba}_{0.5}\text{Sr}_{0.5}\text{Co}_{0.8}\text{Fe}_{0.2}\text{O}_{3-\delta}$ + YSZ; c) $\text{Ba}_{0.5}\text{Sr}_{0.5}\text{Co}_{0.8}\text{Fe}_{0.2}\text{O}_{3-\delta}$ + CGO (the BaCeO_3 peaks are too small for reliable quantification); d) quantitative analysis of peak areas.

$\text{Ba}_{0.5}\text{Sr}_{0.5}\text{Co}_{0.8}\text{Fe}_{0.2}\text{O}_{3-\delta}$ reacts with YSZ already at 750 °C (Fig. 4.6c), leading mainly to a new perovskite phase with an extremely large lattice constant of 4.14 Å. This reaction is essentially complete after 12 h at 850 °C (all BSCF5080 is used up, see Fig. 4.7). In the temperature series (Fig. 4.6c), further grain growth and incorporation of remaining YSZ occurs up to 1000 °C narrowing the peaks. From the initial mixture, a 1:1 molar ratio

of BSCF5080 and YSZ, one can conclude that the composition of the new perovskite phase must be close to $(\text{Ba}_{0.5}\text{Sr}_{0.5}\text{Y}_{0.16})_{0.86}((\text{Co,Fe})_{0.32}\text{Zr}_{0.84})_{0.86}\text{O}_{3-\delta}$ (Y substitutes for Ba in BaTiO_3 [75], therefore we count it as an A-site cation here), while a part of the surplus Co and/or Fe is found in the Co_3O_4 phase (peaks at $2\theta \approx 37^\circ$). Since similar perovskites such as $\text{BaCo}_{0.4}\text{Fe}_{0.4}\text{Zr}_{0.2}\text{O}_{3-\delta}$ (lattice constant = 4.05 Å) are used as oxygen permeation membranes [45], one may expect this new phase not to be so detrimental for oxygen incorporation as the pyrochlore phase, but probably not as effective as the initial composition. Additionally, the transformation of YSZ into a mixed conducting perovskite could short-circuit the cell. Above 850 °C BSCF5080 reacts even with CGO, but in contrast to YSZ most of the CGO is still present upon exposure to 1100 °C. BaCeO_3 can be identified as a reaction product by its peaks at $2\theta = 41^\circ$ and 50.8° . While the BaCeO_3 peak intensity seems to saturate above 900 °C, the further increasing peak shift of the remaining BSCF-related perovskite to higher angles indicates an ongoing composition change, probably due to Ba loss.

The observations made for BSCF5080 in contact with YSZ or CGO are in qualitative agreement with literature (Ref. [40]: BSCF/YSZ molar ratio not given but probably close to 1:1; Ref. [76]: BSCF/YSZ molar ratio $\approx 1:1.8 \Rightarrow$ unreacted YSZ after complete BSCF conversion), but in both references quantitative analysis was not performed and only the temperature was varied. Interestingly, samples with low Ba content ($x = 0$ or 0.3) showed no reactions with CGO at 1000 °C [40].

The known high interfacial reactivity of cobaltite perovskites with standard solid electrolytes is even more pronounced for BSCF5080 compared to LSCF6080. This may be related to the fact that the size misfit between A- and B- site cations in BSCF5080 is extremely large. In the reaction with YSZ, the substitution of Co/Fe by Zr as well as the incorporation of Y on the A-site reduce this mismatch. The Ce in CGO is already larger than the optimum size for a B-site cation in (Ba,Sr)-based perovskites, together with the smaller acidity of ceria compared to zirconia, this might explain its lower reactivity. It remains to be clarified to which extent the good electrode performance of BSCF5080 is related to the observed large lattice constant or the A/B cation size mismatch, and thus how far the reactivity towards the electrolyte materials can be reduced without losing electrocatalytic performance.

The interfacial reaction between a 300 nm LSCF6080 film and a YSZ substrate [58] has been found to start at the same temperature (800 °C annealed for 10 h) as the reaction between the LSCF6080 and YSZ powder. The interfacial reaction between the BSCF5080 film and the YSZ substrate was not studied in this thesis. If we assume similar reactivity for the films and the powders, new phases may appear after long-term measurements at

750 °C between the BSCF thin film and the YSZ substrate. Since the sample was not always kept at 750 °C, the reaction at the BSCF5080/YSZ interface can be assumed to be not severe. Moreover, the slight interfacial reaction at the BSCF5080/YSZ interface does not influence the determination of the surface resistance as long as surface reaction and interfacial ion transfer are well separated in the impedance spectra.

The possibility of an interfacial reaction between BSCF5080 films and MgO substrates is relevant for the isotope exchange measurements and therefore the result is also reported here although it is not with regard to the compatibility with electrolyte materials. Approximately 50 mg MgO powder and 60 mg $(\text{Ba}_{0.5}\text{Sr}_{0.5})_{1.04}\text{Co}_{0.8}\text{Fe}_{0.2}\text{O}_{3-\delta}$ powder was ground together in a mortar. This mixture and a 300 nm BSCF5080 film on a (100)-oriented MgO substrate were annealed at 800 °C for 300 h in air. New phases caused by the phase transformation of BSCF5080 (section 4.2.3) are detected in the powder and the film; and some carbonate may also have formed at the surface of the BSCF5080 film. But no reaction product between MgO and BSCF5080 are detected.

4.2.2 Stability under CO₂-containing atmosphere

Perovskite oxides with alkaline-earth metal ions are susceptible to carbonate formation in CO₂-containing atmosphere. When $\text{Ba}_{0.5}\text{Sr}_{0.5}\text{Co}_{0.8}\text{Fe}_{0.2}\text{O}_{3-\delta}$ cathodes were exposed to CO₂-containing oxidant gas in SOFCs, the fuel cell performance degraded, but recovered when switching back to CO₂-free atmosphere at temperatures higher than 550 °C [77]. For $\text{Ba}_{0.5}\text{Sr}_{0.5}\text{Co}_{0.8}\text{Fe}_{0.2}\text{O}_{3-\delta}$ oxygen permeation membranes, CO₂ in the feed gas decreased the oxygen permeation flux which could also recover when switching back to CO₂-free atmosphere [78]. These studies have claimed that the formation of carbonate at the surface was responsible for the degraded fuel cell performance and decreased oxygen permeation flux [77,78]. Therefore it is interesting to investigate the effect of BSCF cation composition on the carbonate formation to see if the composition can be optimized with regard to the stability under CO₂-containing atmosphere.

The carbonate formation was studied with thermogravimetric analysis. The weight of the powder for analysis was approximately 200 mg for all the compositions studied here. The temperature program was the same as described in Fig. 3.2. The total gas flow rate was 50 ml/min. The powder was first heated up and slowly cooled down in O₂/N₂ mixture with $P(\text{O}_2) = 0.1$ bar. The atmosphere was switched to a CO₂/O₂/N₂ mixture with $P(\text{O}_2)$ and $P(\text{CO}_2)$ both equal to 0.1 bar when the sample was cooled down to 250 °C. The mass change during the heating process from 250 °C to 1000 °C in CO₂-containing atmosphere is shown in Fig. 4.8a. The mass increase during this process is due to the adsorption/reaction of CO₂ with the powder and the

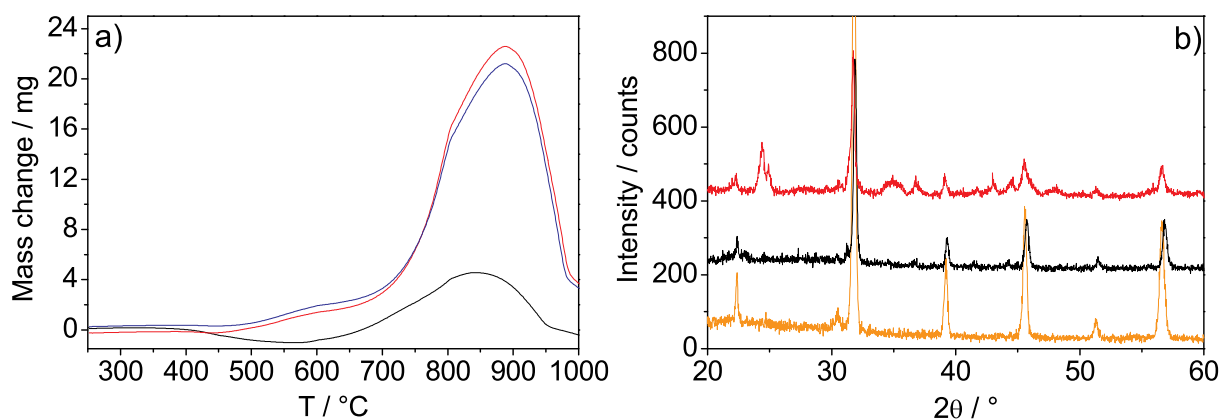


Figure 4.8: a) Mass change upon heating in $\text{CO}_2/\text{O}_2/\text{N}_2$ mixture with $P(\text{O}_2)$ and $P(\text{CO}_2)$ both equal to 0.1 bar for $(\text{Ba}_{0.5}\text{Sr}_{0.5})_{1.04}\text{Co}_{0.8}\text{Fe}_{0.2}\text{O}_{3-\delta}$ (red curve), $\text{Ba}_{0.5}\text{Sr}_{0.5}\text{Co}_{0.8}\text{Fe}_{0.2}\text{O}_{3-\delta}$ (blue curve) and $\text{Ba}_{0.45}\text{Sr}_{0.5}\text{Co}_{0.4}\text{Fe}_{0.6}\text{O}_{3-\delta}$ (black curve); b) Comparison of X-ray diffractograms of $\text{Ba}_{0.45}\text{Sr}_{0.5}\text{Co}_{0.4}\text{Fe}_{0.6}\text{O}_{3-\delta}$ (black curve, shifted upwards) and $(\text{Ba}_{0.5}\text{Sr}_{0.5})_{1.04}\text{Co}_{0.8}\text{Fe}_{0.2}\text{O}_{3-\delta}$ (red curve, shifted upwards) after cooling down in CO_2 -containing atmosphere in the thermogravimetric analysis with the one from as prepared $(\text{Ba}_{0.5}\text{Sr}_{0.5})_{1.04}\text{Co}_{0.8}\text{Fe}_{0.2}\text{O}_{3-\delta}$ (orange curve).

mass decrease is mainly due to the decomposition of the carbonate. At first glance, the A-site deficient $\text{Ba}_{0.45}\text{Sr}_{0.5}\text{Co}_{0.4}\text{Fe}_{0.6}\text{O}_{3-\delta}$ seems to be more CO_2 resistive. The X-ray diffractogram of $\text{Ba}_{0.45}\text{Sr}_{0.5}\text{Co}_{0.4}\text{Fe}_{0.6}\text{O}_{3-\delta}$ after cooling down in CO_2 -containing atmosphere in the thermogravimetric analysis indicates that the powder exhibit the cubic structure identical with as prepared $(\text{Ba}_{0.5}\text{Sr}_{0.5})_{1.04}\text{Co}_{0.8}\text{Fe}_{0.2}\text{O}_{3-\delta}$ and has only minor amount of carbonate. However, there is considerable amount of carbonate detected after $(\text{Ba}_{0.5}\text{Sr}_{0.5})_{1.04}\text{Co}_{0.8}\text{Fe}_{0.2}\text{O}_{3-\delta}$ was treated in the same way (Fig. 4.8b). But as mentioned previously, the carbonate formation is limited to the surface at least in the early stage. The surface area is therefore relevant. BET surface areas of $(\text{Ba}_{0.5}\text{Sr}_{0.5})_{1.04}\text{Co}_{0.8}\text{Fe}_{0.2}\text{O}_{3-\delta}$ and $\text{Ba}_{0.45}\text{Sr}_{0.5}\text{Co}_{0.4}\text{Fe}_{0.6}\text{O}_{3-\delta}$ are 21.1 g/cm^2 and 0.3 g/cm^2 respectively. The surface area for $\text{Ba}_{0.45}\text{Sr}_{0.5}\text{Co}_{0.4}\text{Fe}_{0.6}\text{O}_{3-\delta}$ is 1/70 of that for $(\text{Ba}_{0.5}\text{Sr}_{0.5})_{1.04}\text{Co}_{0.8}\text{Fe}_{0.2}\text{O}_{3-\delta}$, so the amount of carbonate formed at high temperatures for $\text{Ba}_{0.45}\text{Sr}_{0.5}\text{Co}_{0.4}\text{Fe}_{0.6}\text{O}_{3-\delta}$ being about 1/5 to 1/6 of that for $(\text{Ba}_{0.5}\text{Sr}_{0.5})_{1.04}\text{Co}_{0.8}\text{Fe}_{0.2}\text{O}_{3-\delta}$ is indeed more pronounced. Therefore, Ba-deficient $\text{Ba}_{0.45}\text{Sr}_{0.5}\text{Co}_{0.4}\text{Fe}_{0.6}\text{O}_{3-\delta}$ is not effective for inhibiting the carbonate formation. The larger grain size of $\text{Ba}_{0.45}\text{Sr}_{0.5}\text{Co}_{0.4}\text{Fe}_{0.6}\text{O}_{3-\delta}$ (after identical calcination conditions) can be seen as an indication for enhanced cation diffusivity, which would then also accelerate the decomposition of the perovskite into $(\text{Ba},\text{Sr})\text{CO}_3$.

4.2.3 Long-term phase stability

For those BSCF compositions which crystallized in the cubic perovskite structure under the present synthesis conditions, the long-term phase stability of the BSCF powders was tested by annealing the powder at 800 °C for 300 h in air. The phases before and after the treatment were analyzed by X-ray diffraction. The results for $(\text{Ba}_{0.5}\text{Sr}_{0.5})_{1.04}\text{Co}_{0.8}\text{Fe}_{0.2}\text{O}_{3-\delta}$ and $\text{Ba}_{0.5}\text{Sr}_{0.5}\text{Co}_{0.4}\text{Fe}_{0.6}\text{O}_{3-\delta}$ are shown as examples in Fig. 4.9. After the heat treatment, a partial phase transformation is detected for $(\text{Ba}_{0.5}\text{Sr}_{0.5})_{1.04}\text{Co}_{0.8}\text{Fe}_{0.2}\text{O}_{3-\delta}$ (Fig. 4.9a, Goldschmidt tolerance factor $t = 1.054$, see section 4.5.3 for the details of the calculation of t) and $\text{Ba}_{0.25}\text{Sr}_{0.75}\text{Co}_{0.8}\text{Fe}_{0.2}\text{O}_{3-\delta}$ ($t = 1.017$). For other compositions with lower Co content, i. e., $\text{Ba}_{0.5}\text{Sr}_{0.5}\text{Co}_{0.4}\text{Fe}_{0.6}\text{O}_{3-\delta}$ (Fig. 4.9b, $t = 1.022$), $\text{Ba}_{0.45}\text{Sr}_{0.5}\text{Co}_{0.4}\text{Fe}_{0.6}\text{O}_{3-\delta}$ ($t = 0.994$) and $\text{Ba}_{0.75}\text{Sr}_{0.25}\text{Co}_{0.4}\text{Fe}_{0.6}\text{O}_{3-\delta}$ ($t = 1.036$), no obvious secondary phases are found after the treatment. It has been reported that $\text{Ba}_{0.5}\text{Sr}_{0.5}\text{Co}_{0.8}\text{Fe}_{0.2}\text{O}_{3-\delta}$ powder treated

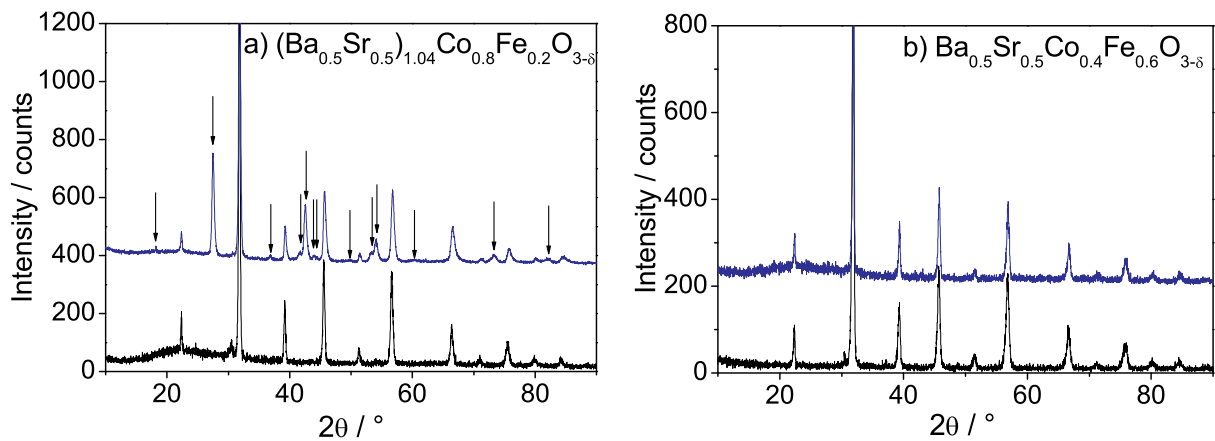


Figure 4.9: Powder diffractograms of a) $(\text{Ba}_{0.5}\text{Sr}_{0.5})_{1.04}\text{Co}_{0.8}\text{Fe}_{0.2}\text{O}_{3-\delta}$ and b) $\text{Ba}_{0.45}\text{Sr}_{0.5}\text{Co}_{0.8}\text{Fe}_{0.2}\text{O}_{3-\delta}$ before (black curves) and after (blue curves, shifted upward) annealing at 800 °C for 300 h in air. The arrows in Fig. a) indicate the peak positions of the new phases.

for 500 h at 750 °C decomposed and formed BaCoO_2 [9]. It is difficult to determine the new phases from the powder diffractograms accurately since the annealed powder is a mixture of the cubic and noncubic phases, but the new phase is not BaCoO_2 . It has been shown in Ref. [27] that $\text{Ba}_x\text{Sr}_{1-x}\text{Co}_{0.8}\text{Fe}_{0.2}\text{O}_{3-\delta}$ ($x=0, 0.2, 0.5$) transforms at intermediate temperatures, e. g., 750 °C to 850 °C, from a cubic perovskite to a hexagonal perovskite phase, which is a kinetically slow but reversible process. Attempts of indexing the new phase using “DICVOL 91” [79] and “TOPAS 2.1” software indicate that it might not necessarily be a hexagonal phase (although the assignment to a 2H hexagonal perovskite structure as observed for $\text{Ba}_{1-x}\text{Sr}_x\text{CoO}_{3-\delta}$ [42] is tempting). According to a recent study,

the new phases are possibly a mixture of monoclinic perovskite and hexagonal perovskite [80].

It was suggested to reduce the Goldschmidt tolerance factor in order to stabilize the cubic perovskite structure [27]. However, for the investigated compositions, no obvious relationship between the cubic perovskite stability at intermediate temperatures and tolerance factors could be established. Nevertheless at the higher powder synthesis temperature (1000 °C) where kinetic limitations are less severe, this could serve as a guideline to determine the compositions that form the cubic perovskite phase. At intermediate temperatures, the compositions with larger distance to the existence range of noncubic phases in Fig. 4.2 ($\text{Ba}_{0.25}\text{Sr}_{0.75}\text{Co}_{0.4}\text{Fe}_{0.6}\text{O}_{3-\delta}$ and $\text{Ba}_{0.5}\text{Sr}_{0.5}\text{Co}_{0.4}\text{Fe}_{0.6}\text{O}_{3-\delta}$) seem to be more stable.

For an A-site deficient $(\text{Ba}_{0.5}\text{Sr}_{0.5})_{1-x}\text{Co}_{0.8}\text{Fe}_{0.2}\text{O}_{3-\delta}$ sample (850 °C for 100 h in air), long-term phase stability was observed [81]. Therefore from the point of view of long-term phase stability, tuning the BSCF cation composition of interest to be slightly Ba-deficient may be practical for application as SOFC cathode.

4.3 Impedance spectroscopy on BSCF microelectrodes

4.3.1 A representative impedance spectrum without dc bias

Fig. 4.10 shows a typical impedance spectrum without dc bias for the materials studied in this thesis as well as the equivalent circuit used for evaluating the experimental data. The analysis of the spectrum was achieved by the determination of an appropriate equivalent circuit. The equivalent circuit was simplified from a general model for mixed conducting electrodes [82] under the conditions that the electrode material has a high electronic and a high ionic conductivity (such as BSCF) and that the oxygen incorporation occurs through the “bulk path” and is limited by the surface reaction rather than by the oxygen transport through the BSCF. The details for the simplification and the validity of the equivalent circuit have been given in Ref. [33].

There are three main features in the spectrum: one axis intercept at high frequency and two semicircles at intermediate and low frequencies. The interpretation of the five quantities in the equivalent circuit are as follows:

The dominant resistance R_s is the resistance associated with the oxygen incorporation reaction at the surface of the electrode and is inversely proportional to the effective surface exchange rate constant k^a [83]

$$k^a = \frac{k_B T}{4e^2 R_s c_O} \quad (4.4)$$

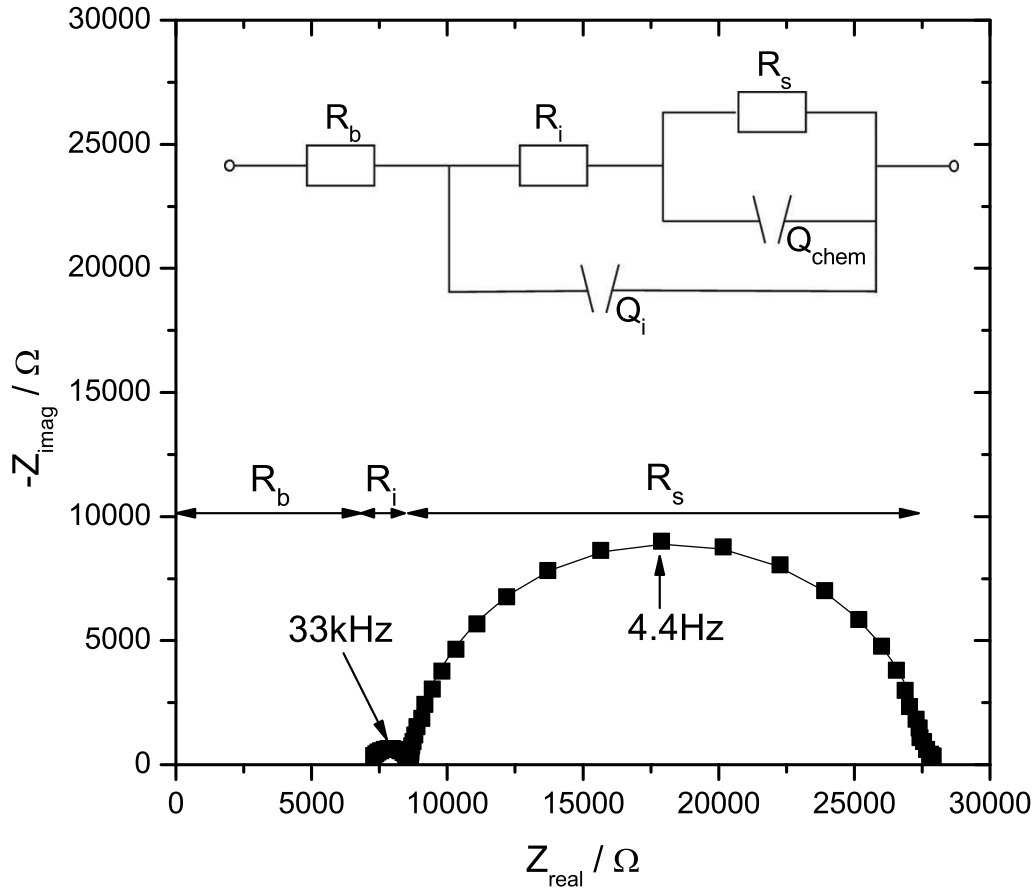


Figure 4.10: An impedance spectrum recorded from $\text{Ba}_{0.25}\text{Sr}_{0.75}\text{Co}_{0.8}\text{Fe}_{0.2}\text{O}_{3-\delta}$ at 650°C and $P(\text{O}_2) = 0.2$ bar on a $100\ \mu\text{m}$ microelectrode. The solid line represents the fit with the equivalent circuit shown in the inset.

(k_B : Boltzmann constant; T : temperature; e : elementary charge; R_s : area specific surface resistance; c_{O} : concentration of lattice oxygen). R_s corresponds to the low frequency semicircle, indicating a large capacitance. This large capacitance is a “chemical capacitance” C_δ [82] related to the oxygen stoichiometry change in the electrode bulk and is inversely proportional to the derivative of the chemical potential of oxygen vacancy with respect to oxygen vacancy concentration:

$$C_\delta \propto \left(\frac{\partial \mu_{V_{\text{O}}^{\bullet\bullet}}}{\partial c_{V_{\text{O}}^{\bullet\bullet}}} \right)^{-1} \quad (4.5)$$

The intermediate frequency semicircle corresponds to the oxygen ion transfer through the BSCF/YSZ interface and is characterized by R_i and the related capacitance C_i . The axis intercept R_b at high frequencies is mainly due to the YSZ bulk resistance (owing to its much larger area, the counter electrode does not contribute to the measured impedance [33]). Since the capacitors had been replaced by more general constant phase elements Q

in the equivalent circuit, the resulting capacitance should be calculated according to [84]

$$C = (R^{1-n}Q)^{1/n} \quad (4.6)$$

where n is a parameter that indicates the degree of depression of the semicircle in the spectrum. Typically n for the low frequency semicircle is close to 1 (0.97 ± 0.02 on average for the compositions studied here).

Depending on the temperature and/or oxygen partial pressure, for some of the compositions studied in this thesis, the middle frequency semicircle is not always separable from the low frequency semicircle or not detectable due to some scattering of the data at higher frequencies. However, this will not change the interpretation of the spectrum and has little influence on the determination of the value of the surface resistance. Average parameter values at 750 °C and $P(O_2) = 0.2$ bar on 60 μm microelectrodes obtained by fitting the impedance spectra for six representative compositions are given in Table 4.2.

Table 4.2: Average values of surface resistance R_{surf} , area-normalized surface resistance R_s and chemical capacitance C_δ at 750 °C and $P(O_2) = 0.2$ bar on 60 μm diameter and 100 nm thick microelectrodes for six representative compositions.

Composition	R_{surf} (k Ω)	R_s ($\Omega \text{ cm}^2$)	C_δ (F)
$\text{Ba}_{0.5}\text{Sr}_{0.5}\text{Co}_{0.8}\text{Fe}_{0.2}\text{O}_{3-\delta}$	3.5 ± 1.0	0.10	$(8.8 \pm 1.0) \times 10^{-7}$
$\text{Ba}_{0.25}\text{Sr}_{0.75}\text{Co}_{0.8}\text{Fe}_{0.2}\text{O}_{3-\delta}$	9.8 ± 2.6	0.28	$(4.8 \pm 1.0) \times 10^{-7}$
$\text{SrCo}_{0.8}\text{Fe}_{0.2}\text{O}_{3-\delta}$	14.4 ± 4.6	0.41	$(6.1 \pm 0.5) \times 10^{-7}$
$\text{Ba}_{0.5}\text{Sr}_{0.5}\text{Co}_{0.4}\text{Fe}_{0.6}\text{O}_{3-\delta}$	26.9 ± 13.7	0.76	$(5.4 \pm 0.6) \times 10^{-7}$
$\text{Ba}_{0.5}\text{Sr}_{0.5}\text{FeO}_{3-\delta}$	38.2 ± 12.6	1.08	$(5.0 \pm 1.4) \times 10^{-7}$
$\text{SrFeO}_{3-\delta}$	128.6 ± 31.9	3.64	$(6.0 \pm 0.7) \times 10^{-7}$

Impedance spectra for determining the averaged values at 750 °C and $P(O_2) = 0.2$ bar were measured on at least two individual samples for each composition. On each sample, measurements were carried out on more than ten microelectrodes. Compared with $(\text{La,Sr})(\text{Co,Fe})\text{O}_{3-\delta}$ microelectrodes prepared in a similar way, $(\text{Ba,Sr})(\text{Co,Fe})\text{O}_{3-\delta}$ have a lower surface resistance [85]. This indicates that the substitution of La^{3+} rare-earth cations by exclusively A^{2+} alkaline-earth metal cations could generally effectively accelerate the rate of oxygen incorporation into the related mixed conducting perovskites. The effect of the substitution was studied and used to clarify the reason for the accelerated oxygen incorporation reaction on BSCF. This will be reported in detail in the following sections.

4.3.2 Temperature dependence

The temperature dependence for $\text{Ba}_{0.25}\text{Sr}_{0.75}\text{Co}_{0.8}\text{Fe}_{0.2}\text{O}_{3-\delta}$ is shown in Fig. 4.11. All resistances show Arrhenius-type behavior (for certain BSCF compositions, the Arrhenius plots of R_s are slightly curved in the temperature range studied) and the corresponding apparent Arrhenius term E' for each resistance (which in fact is the negative activation energy E_a for the corresponding rate process, $E_a = -E'$) is indicated in the figure as well. For the capacitances, “formal E_a values” (which do not correspond to kinetic quantities) obtained from Arrhenius plots are given.

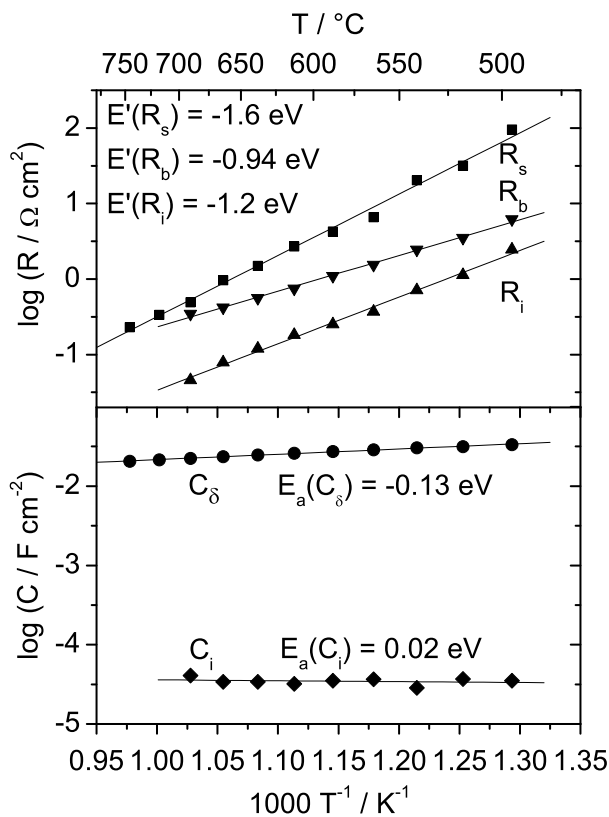


Figure 4.11: Temperature dependence of R_s , R_b , R_i , C_δ and C_i for $\text{Ba}_{0.25}\text{Sr}_{0.75}\text{Co}_{0.8}\text{Fe}_{0.2}\text{O}_{3-\delta}$ measured on a $100 \mu\text{m}$ microelectrode at $P(\text{O}_2) = 0.2$ bar.

As mentioned in section 4.3.1, it is not always possible to probe the middle frequency semicircle. Nevertheless, by fitting the data of the low frequency semicircle, R_s and C_δ could always be determined accurately. The individual activation energies for the aforementioned six compositions are listed in Table 4.3; they show a rather similar temperature dependence.

The temperature dependence for $\text{Ba}_{0.5}\text{Sr}_{0.5}\text{Co}_{0.8}\text{Fe}_{0.2}\text{O}_{3-\delta}$ has been reported in a previous study [15] and it is repeated on a new sample here. The activation energy amounts

Table 4.3: Activation energy related to surface resistance R_s and formal activation energy of chemical capacitance C_δ in the temperature range of 500 °C to 750 °C on 100 μm microelectrodes at $P(\text{O}_2) = 0.2$ bar for six representative compositions.

Composition	$-E'(R_s)$ (eV)	$-E_a(C_\delta)$ (eV)
$\text{Ba}_{0.5}\text{Sr}_{0.5}\text{Co}_{0.8}\text{Fe}_{0.2}\text{O}_{3-\delta}$	1.6 ± 0.1	0.16 ± 0.01
$\text{Ba}_{0.25}\text{Sr}_{0.75}\text{Co}_{0.8}\text{Fe}_{0.2}\text{O}_{3-\delta}$	1.6 ± 0.1	0.13 ± 0.01
$\text{SrCo}_{0.8}\text{Fe}_{0.2}\text{O}_{3-\delta}$	1.8 ± 0.1	0.18 ± 0.01
$\text{Ba}_{0.5}\text{Sr}_{0.5}\text{Co}_{0.4}\text{Fe}_{0.6}\text{O}_{3-\delta}$	1.3 ± 0.1	0.17 ± 0.02
$\text{Ba}_{0.5}\text{Sr}_{0.5}\text{FeO}_{3-\delta}$	1.7 ± 0.1	0.13 ± 0.02
$\text{SrFeO}_{3-\delta}$	1.8 ± 0.1	$-(0.03 \pm 0.01)$

to 1.6 eV, and is thus close to the value of 1.8 eV reported in [15]. However it is higher than the value of ≈ 1.1 eV observed for porous cathodes [10, 86]. This may be due to the fact that often gas diffusion, surface exchange and bulk transport resistance contribute to the effective electrode resistance of porous electrodes. Moreover, it has to be kept in mind that the porous electrodes were exposed to higher sintering temperatures (1000 °C) than in the microelectrode preparation (lower than 800 °C), and that any resulting change in the surface composition may affect the reaction kinetics.

The activation energies related to R_s for other compositions are in the range of 1.3 eV to 1.8 eV, which is comparable to the values for LSCF [14]. However, there is no obvious increase of activation energy towards Fe-rich compositions as observed in LSCF [14].

When the samples are kept at high temperatures, the activation energies of ionic conductivities in YSZ and electrode-electrolyte ion transfer are not obviously affected by this heat treatment. However, the aforementioned degradation makes the accurate determination of the activation energy related to R_s nontrivial. Fig. 4.12 depicts the difference in the activation energies determined during cooling and subsequent heating due to the slow increase of R_s . This difference has been taken into account for the evaluation of the error bars of the activation energies.

The chemical capacitance C_δ describes the variation of oxygen nonstoichiometry upon the variation of $P(\text{O}_2)$. For all BSCF compositions studied here except $\text{SrFeO}_{3-\delta}$, C_δ decreases slightly with increasing temperature which is contrary to the situation for LSCF [14]. Nevertheless, this observation is in good agreement with the temperature and oxygen partial pressure dependence of oxygen nonstoichiometry determined from thermogravimetry (section 4.5.5).

The YSZ bulk resistance R_b could be converted to the YSZ bulk conductivity σ_{YSZ} according to the spreading resistance formula: $\sigma_{\text{YSZ}} = 1/2R_b d_{\text{ME}}$ in which d_{ME} is the

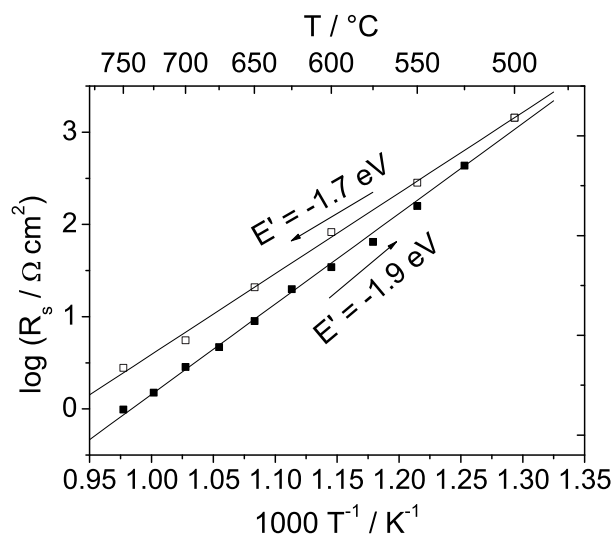


Figure 4.12: Influence of the degradation on the determination of the activation energy related to R_s demonstrated with the measurements on a $100 \mu\text{m}$ $\text{SrCo}_{0.8}\text{Fe}_{0.2}\text{O}_{3-\delta}$ micro-electrode at $P(\text{O}_2) = 0.2$ bar.

diameter of the microelectrode [87]. The activation energy of σ_{YSZ} from R_b (0.94 eV) agrees with the literature values [88] indicating a correct temperature calibration.

4.3.3 Oxygen partial pressure dependence

The $P(\text{O}_2)$ dependence is illustrated with $\text{Ba}_{0.25}\text{Sr}_{0.75}\text{Co}_{0.8}\text{Fe}_{0.2}\text{O}_{3-\delta}$ shown in Fig. 4.13. Measurements always started from low $P(\text{O}_2)$ (around 10^{-4} bar) and proceeded to high $P(\text{O}_2)$ (around 0.9 bar) with a step of one order of magnitude. To estimate the influence of the degradation, after the measurement at highest $P(\text{O}_2)$, another measurement at lowest $P(\text{O}_2)$ or at $P(\text{O}_2) = 0.2$ bar was carried out (e. g., open symbol in Fig. 4.13). Although there was a certain increase, it did not severely change the $P(\text{O}_2)$ dependence (dashed fitting line in Fig. 4.13). In a $\log(R_s)$ - $\log(P(\text{O}_2))$ plot, the data can be fitted to a straight line, the relation between R_s and $P(\text{O}_2)$ is therefore $R_s \sim (P(\text{O}_2))^{-n}$. For the estimation of the error bars for n , both values at low $P(\text{O}_2)$ measured at the beginning and the end were used.

The values of the exponent n for the six representative compositions are summarized in Table 4.4. Even based on a more conservative estimation of the error bar of about ± 0.1 , except $\text{SrFeO}_{3-\delta}$, all the others have n values higher than 0.5. If we start from straightforward oxygen reduction reactions, the reaction order of molecular oxygen species is expected to be 1 if molecular oxygen species are involved in the rate-determining step or 1/2 if only atomic oxygen species appear in the RDS. n is the exponent for the overall $P(\text{O}_2)$ dependence. Since additionally either defects with a negative $P(\text{O}_2)$ dependence

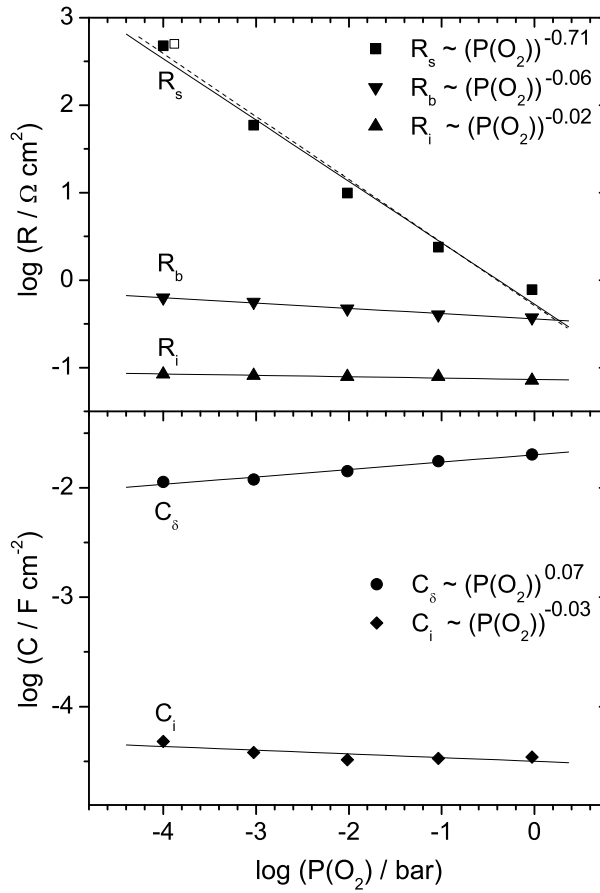


Figure 4.13: $P(O_2)$ dependence of R_s , R_b , R_i , C_δ and C_i for $Ba_{0.25}Sr_{0.75}Co_{0.8}Fe_{0.2}O_{3-\delta}$ measured on a $100 \mu\text{m}$ microelectrode at 700°C . Measurements were carried out in the sequence of increasing $P(O_2)$ and the open symbol refers to the measurement repeated at the lowest $P(O_2)$ after the measurement at the highest $P(O_2)$. Dashed line is the fitting using the value for lowest $P(O_2)$ measured at the end.

Table 4.4: $P(O_2)$ dependence of surface resistance R_s and chemical capacitance C_δ on $100 \mu\text{m}$ microelectrodes at 700°C for six representative compositions.

Composition	n in $R_s \sim (P(O_2))^{-n}$	m in $C_\delta \sim (P(O_2))^m$
$Ba_{0.5}Sr_{0.5}Co_{0.8}Fe_{0.2}O_{3-\delta}$	0.73 ± 0.04	0.05 ± 0.01
$Ba_{0.25}Sr_{0.75}Co_{0.8}Fe_{0.2}O_{3-\delta}$	0.71 ± 0.01	0.07 ± 0.01
$SrCo_{0.8}Fe_{0.2}O_{3-\delta}$	0.61 ± 0.06	0.18 ± 0.02
$Ba_{0.5}Sr_{0.5}Co_{0.4}Fe_{0.6}O_{3-\delta}$	0.65 ± 0.04	0.10 ± 0.01
$Ba_{0.5}Sr_{0.5}FeO_{3-\delta}$	0.83 ± 0.03	0.15 ± 0.02
$SrFeO_{3-\delta}$	0.55 ± 0.02	0.03 ± 0.02

(V_{O^\bullet}, e') are consumed, or those with a positive $P(O_2)$ dependence (h^\bullet) are produced, n should be less than 1 or less than 0.5. An exponent higher than 0.5 in our case strongly indicates that the reaction order of molecular oxygen species is equal to 1. This is a first

mechanistic indication of the oxygen surface incorporation reaction mechanism. Further discussion will be given in section 4.6.

C_δ decreases slightly with decreasing $P(O_2)$, i. e., with increasing $c_{V_{O^{\bullet\bullet}}}$, which is in accordance with the trend observed in the temperature dependence. The $P(O_2)$ dependencies of R_i , R_b and C_i are negligible as expected.

4.3.4 Effect of dc bias

For $Ba_{0.25}Sr_{0.75}Co_{0.8}Fe_{0.2}O_{3-\delta}$, the influence of dc bias on the individual resistances and capacitances is depicted in Fig. 4.14a and c. R_s decreases with both cathodic and anodic bias. On the contrary, R_b and R_i roughly stay constant in the bias range shown in the figure. With the increase of the bias, a significant fraction of the applied bias drops at R_b , correspondingly R_s reaches a plateau.

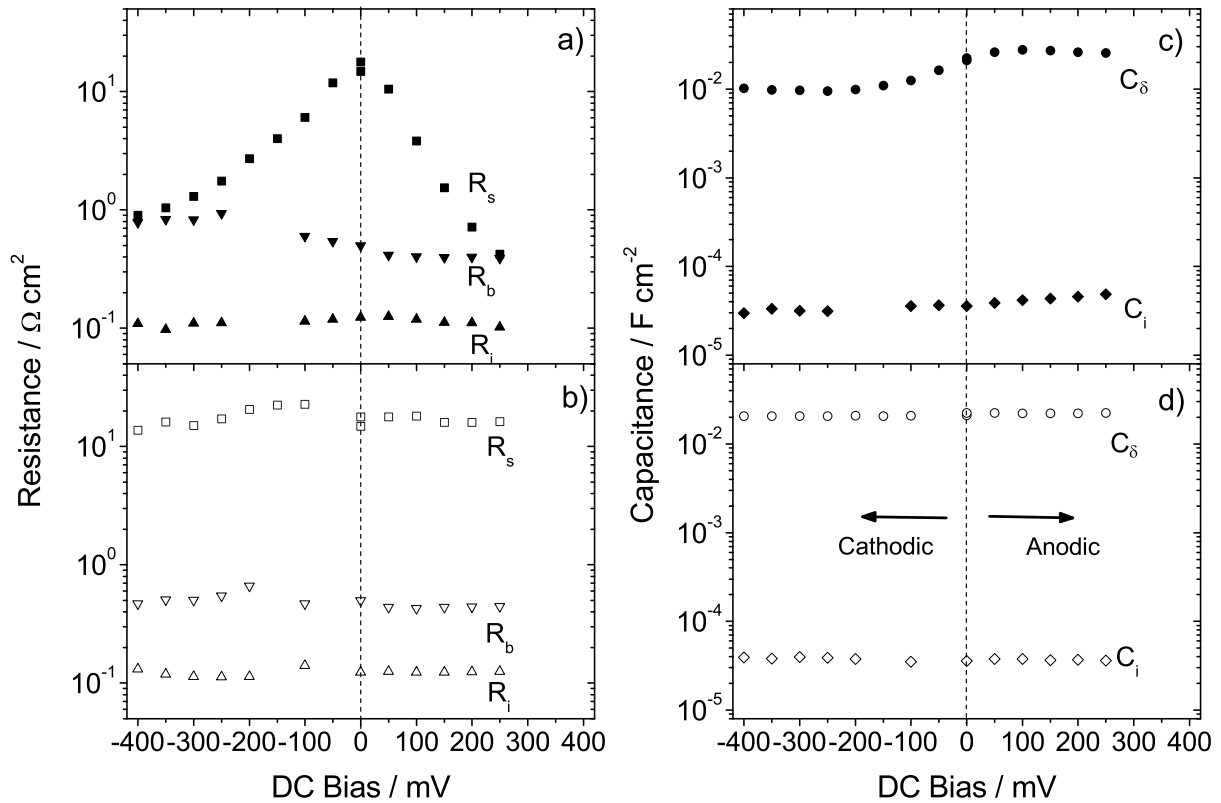


Figure 4.14: a), c) Bias dependence of R_s , R_b , R_i , C_δ and C_i for $Ba_{0.25}Sr_{0.75}Co_{0.8}Fe_{0.2}O_{3-\delta}$ measured on $80 \mu m$ microelectrodes at $650 \text{ }^\circ C$ and $P(O_2) = 0.2 \text{ bar}$. The impedance spectra were recorded after applying two-minutes' bias and with dc bias superimposed on the ac signal. b), d) R_s , R_b , R_i , C_δ and C_i determined from the impedance spectra recorded two minutes after switching off the bias. Cathodic and anodic bias measurements were carried out on two different microelectrodes.

To explain quantitatively the decrease of R_s upon the applied bias is a complex task,

since in contrast to electrochemical experiments in solution, the changes in the surface potential drop (which is the relevant quantity for surface kinetics) are not necessarily equal to the changes in the applied bias [89]. They depend on the detailed reaction mechanism as well as on the coverage of adsorbed charged oxygen species. Generally, the bias can act on the surface reaction rate k^a ($\propto 1/R_s$) either by modifying the bulk defect concentrations (a bias of 200 mV corresponds to $\log(P(O_2)/P^0) = 4.4$ at 650 °C according to Nernst's equation) and/or by the effect of the modified surface potential drop on concentrations of charged surface species or on charged particles crossing the surface plane in the rate-determining step.

C_δ decreases with increasing cathodic bias which is in agreement with the observed decrease of C_δ towards lower $P(O_2)$, since a cathodic bias corresponds to a strongly decreased effective $P(O_2)$ inside the electrode material. C_i roughly keeps unaffected by the applied bias.

The applied bias has been kept small enough to prevent irreversible changes. This was demonstrated with a measurement two minutes after switching off the bias at certain bias values and the results for the individual quantities are included in Fig. 4.14b and d. All the resistances and capacitances after the application of bias are similar to the ones before, for both cathodic and anodic bias.

However, on a more degraded $Ba_{0.5}Sr_{0.5}Co_{0.8}Fe_{0.2}O_{3-\delta}$ sample (with two orders of magnitude higher initial R_s), a similar cathodic bias already introduces an irreversible reduction of R_s (Fig. 4.15b). For each bias measurement, the same procedure has been applied to the $Ba_{0.5}Sr_{0.5}Co_{0.8}Fe_{0.2}O_{3-\delta}$ sample as for the $Ba_{0.25}Sr_{0.75}Co_{0.8}Fe_{0.2}O_{3-\delta}$ sample. The sequence of measurements is as follows (Fig. 4.15): First, anodic bias measurements a1 were carried out on one microelectrode; then on another microelectrode the measurements continued in the sequence of cathodic bias c1, c2 and anodic bias a2. R_s remains unchanged after anodic bias measurements a1, while after cathodic bias measurements c1, it is strongly reduced which has also been confirmed by the following bias measurements on the same microelectrode (c2, a2).

The dramatic reduction of R_s at high dc bias which has been referred to as “electrochemical activation” has been studied on $La_{0.6}Sr_{0.4}Co_{0.8}Fe_{0.2}O_{3-\delta}$ [90]. The effect depends on the magnitude of the bias as well as the length of the bias pulse. For the degraded $Ba_{0.5}Sr_{0.5}Co_{0.8}Fe_{0.2}O_{3-\delta}$ sample, the effect of anodic bias is less pronounced than cathodic bias and the magnitude of the bias that is needed for the activation is much less than in the case of $La_{0.6}Sr_{0.4}Co_{0.8}Fe_{0.2}O_{3-\delta}$.

For a $Ba_{0.5}Sr_{0.5}Co_{0.8}Fe_{0.2}O_{3-\delta}$ sample without severe degradation, the standard “activation voltage” of -2.5 V at 750 °C destroys the microelectrode while -1 V didn't change

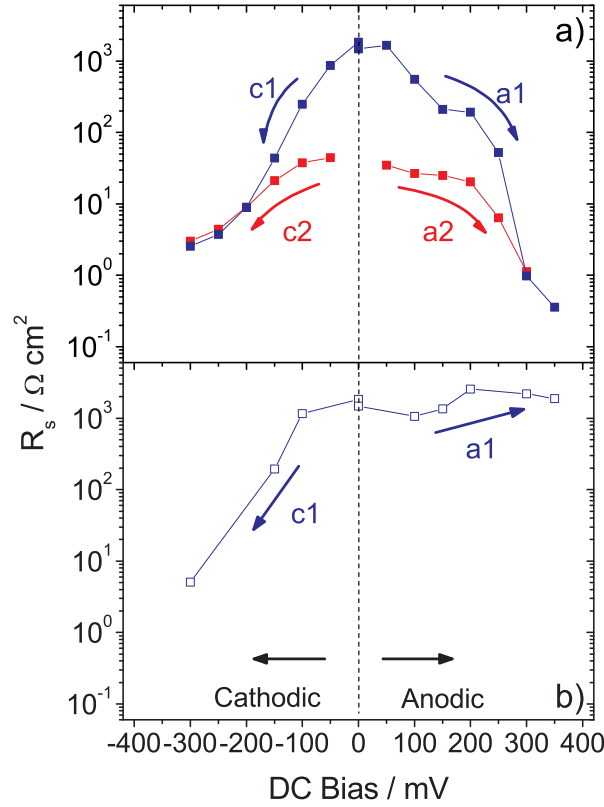


Figure 4.15: a) Bias dependence of R_s for a degraded $\text{Ba}_{0.5}\text{Sr}_{0.5}\text{Co}_{0.8}\text{Fe}_{0.2}\text{O}_{3-\delta}$ sample measured on $80 \mu\text{m}$ microelectrodes at $650 \text{ }^\circ\text{C}$ and $P(\text{O}_2) = 0.2 \text{ bar}$. The impedance spectra were recorded after applying two-minutes' bias and with dc bias superimposed on the ac signal. b) R_s determined from the impedance spectra recorded two minutes after switching off the bias. Anodic bias measurements a1 were carried out on one microelectrode and cathodic bias measurements c1, c2 and anodic bias measurements a2 were carried out on another microelectrode in the sequence of $c1 \rightarrow c2 \rightarrow a2$.

R_s obviously [58]. At the same time, the same cathodic bias does not decrease R_s of the much less degraded $\text{Ba}_{0.25}\text{Sr}_{0.75}\text{Co}_{0.8}\text{Fe}_{0.2}\text{O}_{3-\delta}$ sample. It is therefore possible that there is a upper limit for the surface exchange rate for acceptor-doped perovskite and fluorite oxides which has been suggested by De Souza and Kilner after reviewing a number of tracer exchange data [91].

4.3.5 Comments on the degradation

The reasons for the degradation have not been able to be identified specifically. Intuitively, one might assign it to the phase transformation occurring for certain compositions when kept at intermediate temperatures. Nevertheless, degradation was also confirmed on the $\text{Ba}_{0.5}\text{Sr}_{0.5}\text{Co}_{0.4}\text{Fe}_{0.6}\text{O}_{3-\delta}$ microelectrodes which showed long-term phase stability at intermediate temperatures. Therefore, the phase transformation can be excluded as the

decisive factor for the degradation of the dense thin-film microelectrodes.

A previous study has proposed that the activation effect on LSCF (reduction of R_s upon the application of large bias) may be due to the modified crystal structure and cation composition within the outmost surface layer [58]. Such modification may as well be responsible for the degradation that changed R_s in the opposite direction compared to the activation. However, it is difficult to prove this experimentally for BSCF due to the overlap of the Ba3d and Co2p XPS peaks. Nevertheless, contamination by Si on the surface of the degraded microelectrodes has been confirmed by XPS and may be one of the reasons for the degradation.

4.4 Oxygen diffusion coefficients and effective surface exchange constants of $\text{Ba}_{0.5}\text{Sr}_{0.5}\text{Co}_{0.8}\text{Fe}_{0.2}\text{O}_{3-\delta}$

In the surface reaction, not only the concentration of point defects (e. g. $\text{V}_{\text{O}}^{\bullet\bullet}$) but also their (surface) mobility may be crucial. Since surface defect mobilities are almost impossible to access experimentally, the related bulk defect mobilities can be investigated instead. Reliable bulk ion transport data can be important for the understanding of surface reaction kinetics. However, as explained in section 2.3.3, the accurate determination of oxygen diffusion coefficients is a nontrivial task. In this thesis, the routine method of conductivity relaxation experiments was tried out at first.

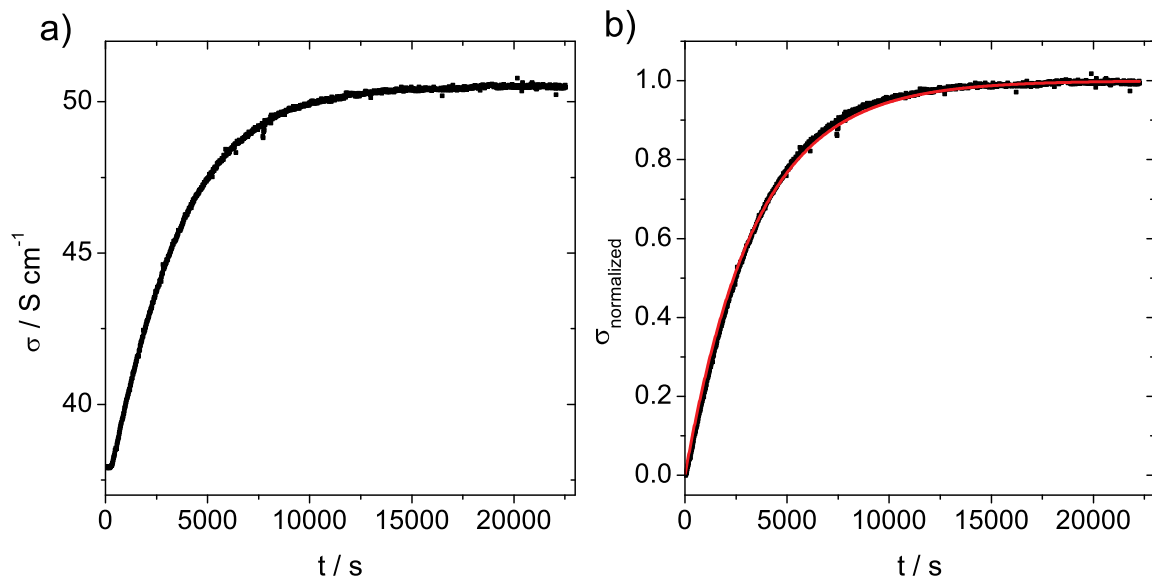


Figure 4.16: For a BSCF5080 sintered pellet: a) Conductivity relaxation upon $\text{P}(\text{O}_2)$ change from 0.3 to 1 bar at 500 °C. b) Variation of the normalized conductivity $\sigma_{\text{normalized}}$ versus time. Red line: fit according to equation 4.7.

Fig. 4.16a shows an example of the conductivity relaxation profile upon the change of $P(\text{O}_2)$ from 0.3 to 1 bar at 500 °C for $\text{Ba}_{0.5}\text{Sr}_{0.5}\text{Co}_{0.8}\text{Fe}_{0.2}\text{O}_{3-\delta}$ (BSCF5080). The oxygen diffusion coefficient D^δ and the surface exchange rate constant k^δ can be extracted by fitting the normalized conductivity $\sigma_{\text{normalized}}$ to the following equation (Fig. 4.16b)

$$\sigma_{\text{normalized}} = \frac{\sigma(t) - \sigma(0)}{\sigma_\infty - \sigma(0)} = 1 - \sum_{n=1}^{\infty} \frac{2L^2 \exp(-\beta_n^2 D^\delta t / l^2)}{\beta_n^2 (\beta_n^2 + L^2 + L)} \quad (4.7)$$

where $\sigma(0)$ is the initial conductivity, σ_∞ the final conductivity at the new $P(\text{O}_2)$, $\sigma(t)$ the conductivity after time t , $L = lk^\delta/D^\delta$ with l as the half width of the sample and β_n 's the positive roots of $\beta_n \tan \beta_n = L$ [92]. This equation is valid for two dimensional diffusion into a sample with square cross-section as in this thesis. The fitting was performed with a MATLAB (Ver. 7.8, The MathWorks, Inc., USA) routine initially written by R. A. De Souza.

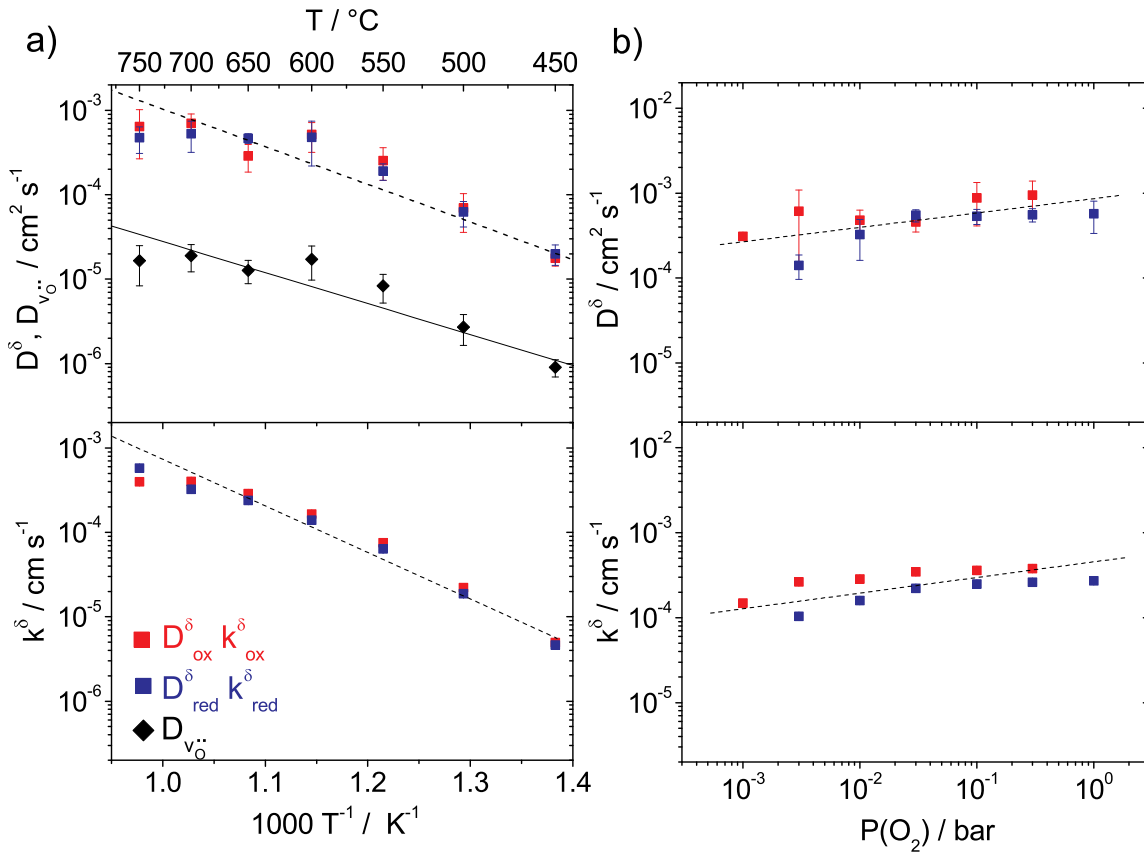


Figure 4.17: a) T dependence ($P(\text{O}_2)$ changes between 0.3 to 1 bar) and b) $P(\text{O}_2)$ dependence (at 600 °C) of the oxygen diffusion coefficients D^δ and the surface exchange rate constants k^δ for BSCF5080 from conductivity relaxation experiments. Data from oxidation and reduction steps are both included in the figure. Oxygen vacancy diffusion coefficients D_{V_O} are calculated from equation 2.17. Dashed lines represent the Arrhenius relation (a) and power law for $P(\text{O}_2)$ dependence (b).

The extracted D^δ and k^δ and their T and $P(\text{O}_2)$ dependencies are summarized in Fig. 4.17. From the Arrhenius plots in Fig. 4.17a, the activation energies of D^δ and k^δ in the temperature range of 450 °C to 750 °C are 0.71 (± 0.13) eV and 0.98 (± 0.10) eV respectively. Oxygen vacancy diffusion coefficients $D_{V_{\bullet\bullet}}$ are calculated from equation 2.17 with the thermodynamic factors ω_{O} ($\omega_{\text{O}} = 1/2\partial\ln P(\text{O}_2)/\partial\ln c_{\text{O}}$). The ω_{O} values are in the range of 106 to 141 between 450 and 750 °C estimated from the thermogravimetric analysis (section 4.5.5). The corresponding activation energy is 0.62 (± 0.13) eV. Contrary to the strong $P(\text{O}_2)$ dependence reported in Ref. [93] (exponents of ≈ 0.6 for k^δ as well as for D^δ), D^δ and k^δ are almost $P(\text{O}_2)$ independent with $D^\delta \sim (P(\text{O}_2))^{0.19\pm 0.07}$ and $k^\delta \sim (P(\text{O}_2))^{0.15\pm 0.04}$. The absolute values of D^δ in Ref. [49, 93] are almost one order of magnitude smaller than D^δ measured here.

The reliability of D^δ and k^δ obtained, however, should be examined carefully. The error bars indicated in Fig. 4.17 only took the errors from the fitting procedure into account. These errors come from the fact that the D^δ and k^δ values from the fitting are to some extent related to the input D^δ , k^δ values of the fitting procedure. Therefore it is necessary to consider the errors introduced in the experimental procedures separately. For example, at relatively high temperatures with faster kinetics, the conductivity relaxation curves are modified by the limited gas flushing rate through the quartz tube. This may be one reason why the curves in the Arrhenius plots tend to flatten towards higher temperatures. In addition to this, a slow phase transformation during the experiments at the surface of the sample is confirmed by XRD measurements (Fig. 4.18). The new hexagonal perovskite

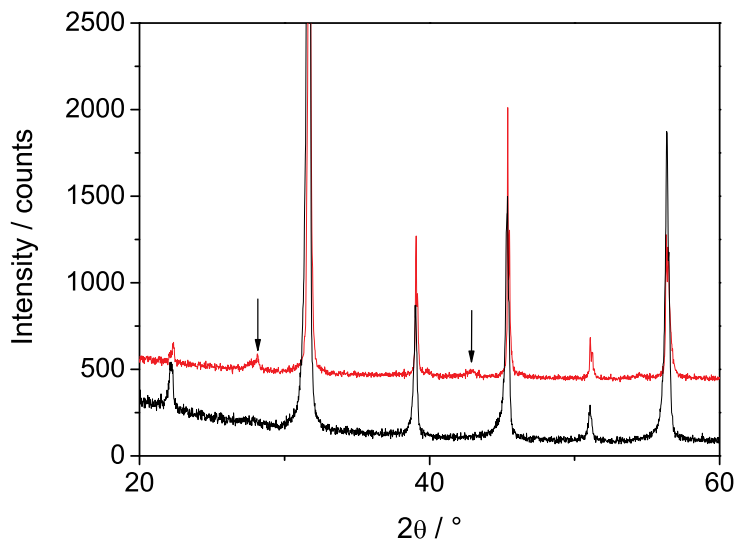


Figure 4.18: X-ray diffractograms of the $(\text{Ba}_{0.5}\text{Sr}_{0.5})_{1.04}\text{Co}_{0.8}\text{Fe}_{0.2}\text{O}_{3-\delta}$ pellet after conductivity relaxation experiments. Red curve (shifted upwards): the pellet as it is; black curve: after the top 0.1 mm layer was polished away.

phase (section 4.2.3) is identified with the extra peaks indicated with the arrows, and the intensity ratio between the (100) and (111) perovskite peaks is different. Since after polishing away the top 0.1 mm layer, the pellet retains its cubic perovskite phase, the phase transformation then mainly affects k^δ but possibly influences D^δ indirectly through the coupling of k^δ and D^δ in the fitting. Unfortunately the studied sample is under mixed k^δ , D^δ control ($k^\delta \approx D^\delta$) which makes the fitting prone to errors.

Based on these discussions, acquiring reliable oxygen diffusion coefficients and effective surface exchange constants from conductivity relaxation experiments is not easy for this sample, not to mention the difficulty in sintering dense BSCF pellets. A reliable separation of D and k would require the comparison of data from thinner (k -limited) and thicker (D -limited) BSCF samples. Compared with the conductivity relaxation experiments, oxygen isotope exchange and SIMS analysis on dense thin films are more suitable for this purpose, avoiding the aforementioned problems. In particular the space-resolved concentration profile $c^*(x)$ allows a more reliable determination of k^* and D^* .

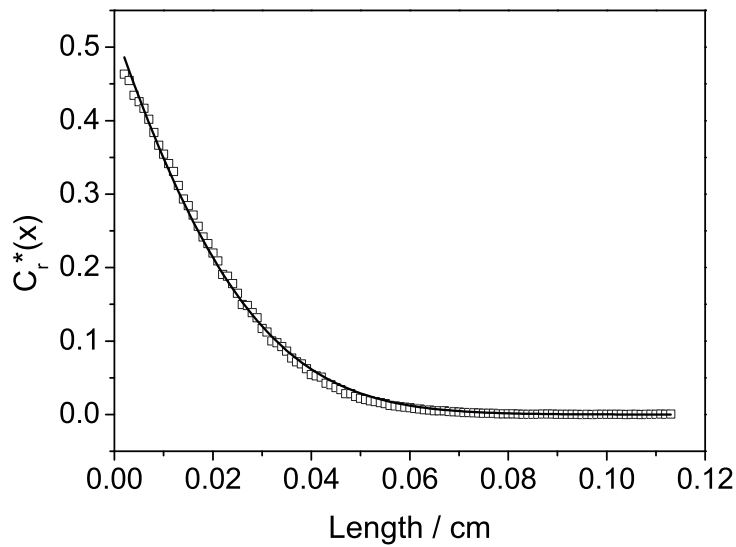


Figure 4.19: Normalized ^{18}O concentration profile $c^*(x)$ after isotope exchange at 600 °C and $P(\text{O}_2) = 0.5$ bar for 1200 s for a $\text{Ba}_{0.5}\text{Sr}_{0.5}\text{Co}_{0.8}\text{Fe}_{0.2}\text{O}_{3-\delta}$ film. Line = fit according to equation 4.8.

Fig. 4.19 is a typical ^{18}O concentration profile from SIMS analysis for BSCF5080 films. The sample was tracer-annealed at 600 °C and $P(\text{O}_2) = 0.5$ bar for 1200 s. The normalized ^{18}O fraction c_r^* is defined as $[c^*(x, t) - c_{\text{bg}}^*] / (c_g^* - c_{\text{bg}}^*)$, where c_{bg}^* and c_g^* refer to the background and annealing gas isotope fraction, $c^*(x, t)$ is the ^{18}O fraction in the film, and x is the distance from the cut. For the geometry mentioned in section 3.7, the measured data can be fitted by the solution of the diffusion equation for a semi-infinite

medium:

$$c^*(x, t) = \operatorname{erfc}\left(\frac{x}{2\sqrt{D^*t}}\right) - \exp\left(\frac{k^*x}{D^*} + \frac{k^{*2}t}{D^*}\right) \cdot \operatorname{erfc}\left(\frac{x}{2\sqrt{D^*t}} + k^*\sqrt{\frac{t}{D^*}}\right) \quad (4.8)$$

where D^* is the tracer diffusion coefficient, k^* is the effective surface exchange constant and t is the exchange time [92]. The fitting was performed with a MATLAB (Ver. 7.8, The MathWorks, Inc., USA) routine initially written by R. A. De Souza.

The temperature dependencies of extracted D^* and k^* are displayed in Fig. 4.20. The activation energy of tracer diffusion is determined to be $E_a = 0.50 (\pm 0.04)$ eV.

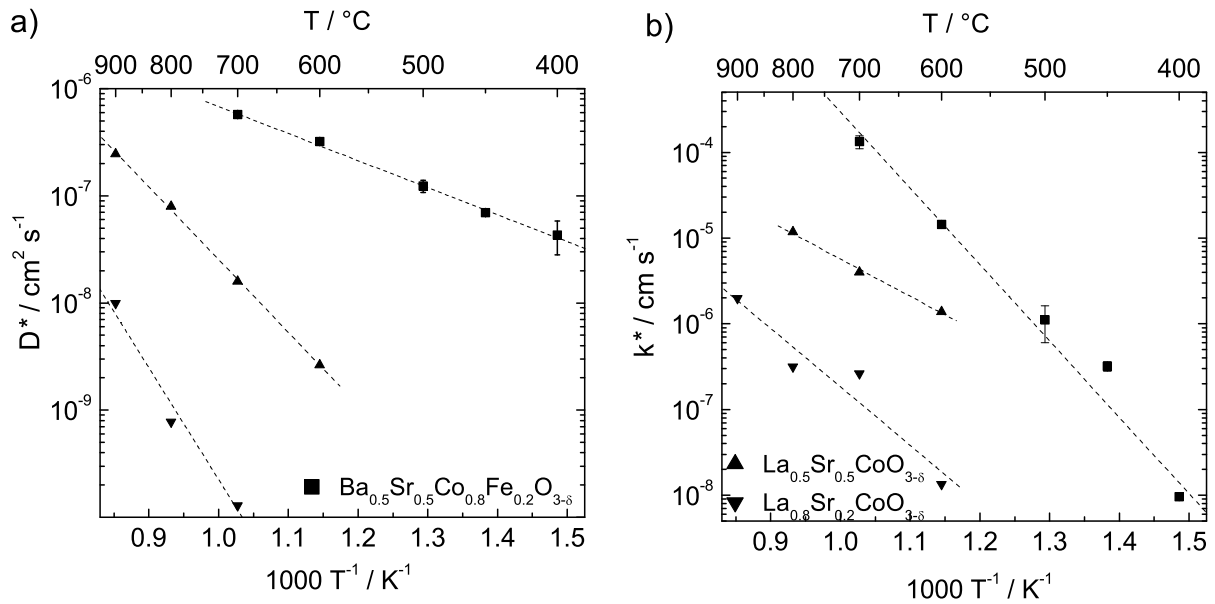


Figure 4.20: Arrhenius plots for $\text{Ba}_{0.5}\text{Sr}_{0.5}\text{Co}_{0.8}\text{Fe}_{0.2}\text{O}_{3-\delta}$ ($P(\text{O}_2) = 0.5$ bar). a) D^* ; b) k^* . Data for $\text{La}_{0.5}\text{Sr}_{0.5}\text{CoO}_{3-\delta}$ and $\text{La}_{0.8}\text{Sr}_{0.2}\text{CoO}_{3-\delta}$ ($P(\text{O}_2) = 1$ atm) [51] are shown for comparison.

$E_a(k^*) = 1.70 (\pm 0.30)$ eV for the BSCF5080 films agrees well with $E_a = 1.6$ to 1.8 eV from the area-normalized surface resistance R_s from microcontact measurements (section 4.3.2), and the absolute k^* value determined here is about one order of magnitude higher (estimated from equation 4.4 assuming $k^* \approx k^a$) [15, 94]. The k^* value for the BSCF5080 films is larger by one to three orders of magnitude than that of $\text{La}_{0.5}\text{Sr}_{0.5}\text{CoO}_{3-\delta}$ and $\text{La}_{0.8}\text{Sr}_{0.2}\text{CoO}_{3-\delta}$ (Fig. 4.20b), confirming faster oxygen exchange in BSCF5080 compared to LSCF. Recently Berenov et al. [95] reported D^* and k^* values measured on sintered BSCF5080 pellets within individual grains. They are generally more than one order of magnitude lower than the data obtained here for dense thin films and have different activation energies for D^* : 0.7 eV and for k^* : 1.1 eV. Those pellets were sintered at $T > 1000$ °C while our films were deposited below 800 °C. Thin films interacting with

the substrate and having a certain lattice mismatch could also behave differently from sintered ceramics. Such differences might affect D^* and k^* .

The vacancy diffusion coefficient $D_{V_{\bullet\bullet}O}$ obtained in this thesis is compared with values from literature in Fig. 4.21a. The calculation of the vacancy diffusion coefficient $D_{V_{\bullet\bullet}O}$ from tracer diffusion coefficient D^* ($D_{V_{\bullet\bullet}O} = D^*c_O/(f \cdot c_{V_{\bullet\bullet}O})$) (section 2.2) uses δ -values determined by thermogravimetry (section 4.5.5). $D_{V_{\bullet\bullet}O}$ has an activation energy $E_a = 0.47 (\pm 0.04)$ eV. This is in agreement with the findings from the oxygen permeation experiments (A, B and C in Fig. 4.21a). The $D_{V_{\bullet\bullet}O}$ -values obtained here are lower by a factor of 3 to 10 than the $D_{V_{\bullet\bullet}O}$ estimated from permeation which can at least partly be attributed to the low density of the permeation membranes (if relative densities were given at all, they were only specified as “higher than 90 %” [47] which is not sufficient to rule out gas leakage reliably). The $D_{V_{\bullet\bullet}O}$ calculated from D^δ in this thesis are slightly higher than the ones from D^* here. This is most probably due to the complexity in the accurate determination of D^δ mentioned previously in this section.

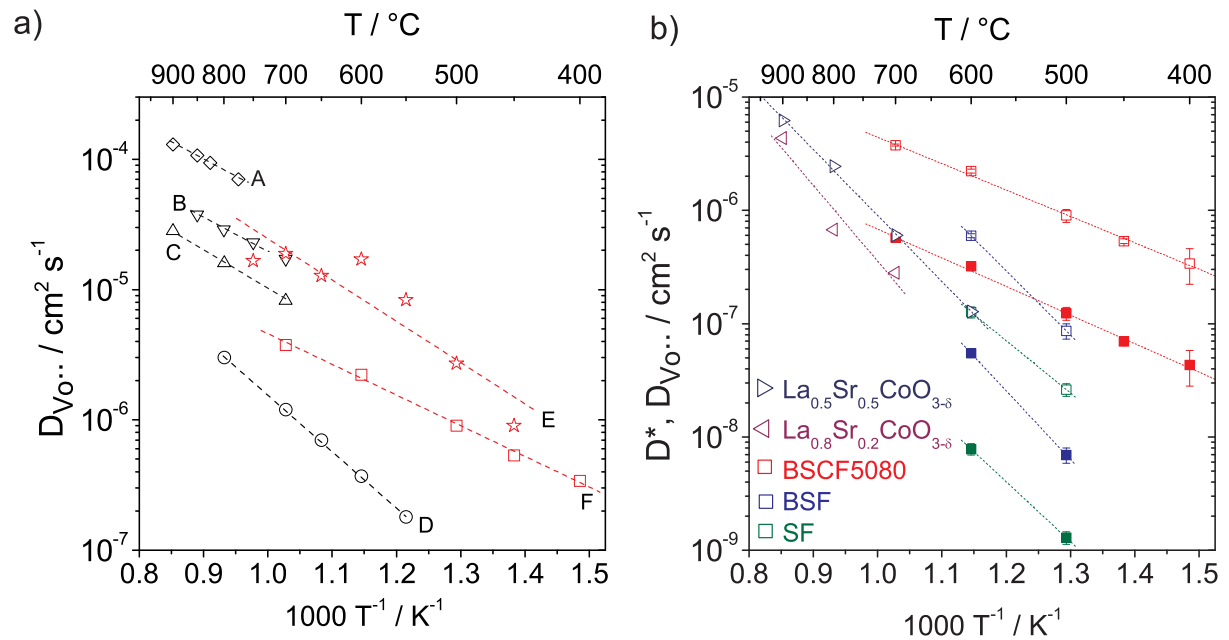


Figure 4.21: a) Comparison of $D_{V_{\bullet\bullet}O}$ obtained in this thesis (E: from conductivity relaxation experiments; F: from oxygen isotope exchange and SIMS measurements) with literature values (A: [10]; B: [46]; C: [47]; D: [49], D^δ extrapolated to 0.1 bar.). b) Arrhenius plots of D^* (solid symbols) and $D_{V_{\bullet\bullet}O}$ (open symbols) for BSCF5080, BSF and SF ($P(O_2) = 0.5$ bar). Data for $La_{0.5}Sr_{0.5}CoO_{3-\delta}$ and $La_{0.8}Sr_{0.2}CoO_{3-\delta}$ ($P(O_2) = 1$ atm) [51] are shown for comparison.

$D_{V_{\bullet\bullet}O}$ of $(La,Sr)(Mn,Fe,Co)O_{3-\delta}$ perovskites [51] (Fig. 4.21b) depends only slightly on the cation composition [21, 48] and can be regarded as being a characteristic for such

perovskites with a rather small lattice constant. In comparison to this, $D_{V_{\bullet\bullet}^{\circ}}$ calculated from D^* for the BSCF5080 films are significantly higher. Different from the situation for $(\text{La,Sr})(\text{Mn,Fe,Co})\text{O}_{3-\delta}$ perovskites, $D_{V_{\bullet\bullet}^{\circ}}$ of $(\text{Ba,Sr})(\text{Co,Fe})\text{O}_{3-\delta}$ perovskites significantly changes with variation of cation composition (Fig. 4.21b). The corresponding activation energies are $E_a(D^*) = 1.2 (\pm 0.1)$ eV, $E_a(D_{V_{\bullet\bullet}^{\circ}}) = 1.1 (\pm 0.1)$ eV for BSF and $E_a(D^*) = 1.0 (\pm 0.1)$ eV, $E_a(D_{V_{\bullet\bullet}^{\circ}}) = 0.9 (\pm 0.1)$ eV for SF. They are closer to the values for $(\text{La,Sr})(\text{Mn,Fe,Co})\text{O}_{3-\delta}$ perovskites [21, 48] and much higher than the activation energy for BSCF5080. The activation energy and the absolute values for SF are in quite good agreements with the values from Ref. [96] ($E_a(D_{V_{\bullet\bullet}^{\circ}}) = 79 (\pm 10)$ kJ/mol and $D_{V_{\bullet\bullet}^{\circ}} = 1.4 \times 10^{-7}$ cm²/s at 600 °C calculated from D^δ obtained in conductivity relaxation experiments) which indicates the reliability of the $D_{V_{\bullet\bullet}^{\circ}}$ values from oxygen isotope exchange experiments.

For a number of perovskites, in particular rare-earth aluminates, the mobility of oxygen vacancy and its activation energy was interpreted in terms of a “critical radius” r_c . r_c indicates the open space within the triangle formed by one B- and two A-site cations through which the O^{2-} has to hop [97]. In a first-order approximation, the mobility of oxygen vacancies $V_{\bullet\bullet}^{\circ}$ in cubic perovskites increases with increasing r_c . One has to pay attention that the examples in Ref. [97] refer to perovskites with Goldschmidt tolerance factor $t < 1$ where r_c varies strongly with cation radii r_A and r_B . In contrast, for perovskites with $t > 1$ such as BSCF, larger A-cations increase the lattice constant but simultaneously block more space in the A_2B -triangle thus r_c hardly varies. Increasing r_B does not increase the lattice constant which is essentially fixed by r_A and r_O , and slightly decreases r_c . Thus r_c of BSCF hardly depends on cation size and is even smaller than LSCF. Thus the high mobility and low activation energy for BSCF seem to be related to other factors, such as the lower average charge (no 3+ rare-earth cations, only 2+ alkaline-earth cations at A-site; Fe^{3+} and $\text{Co}^{2+/3+}$) and higher polarizability (Ba^{2+} and Co^{2+}). Extrapolating our $D_{V_{\bullet\bullet}^{\circ}}$ to 1500 °C and inserting $\delta = 0.5$ results in an ionic conductivity of 2 S/cm, comparable to the 0.3 S/cm at this temperature for $\text{Ba}_{0.8}\text{Sr}_{0.2}\text{Co}_{0.8}\text{Fe}_{0.2}\text{O}_{2.5}$ obtained from pair potential molecular dynamics [98].

Exchange coefficients k^* for different cation compositions in BSCF determined here do not show a systematical change upon the variation of cation composition. Since k^* is perceptible to the conditions at the surface, the values obtained here are believed to be strongly influenced by the preparation method.

4.5 Influence of bulk properties on oxygen incorporation rate

One of the tasks in this study is to get a detailed understanding of the oxygen reduction mechanism on BSCF and related perovskites. On one hand, impedance spectroscopy measurements on microelectrodes yield quantitative data on the oxygen incorporation rate (quantified with the effective surface exchange rate k^a calculated from equation 4.4) which can be compared for BSCFs with different cation compositions. On the other hand, the bulk materials properties are closely correlated to the less easily measurable surface properties. Although the absolute values of point defect concentrations and mobilities will differ, the equilibrium between bulk and surface suggests that the respective variations (e. g., $P(\text{O}_2)$ dependence) are similar. Thus it is a reasonable hypothesis that the bulk properties can influence the steps of the oxygen incorporation by affecting the concentration and the mobility of the involved point defects. Since it is difficult to directly detect the nature and coverage of intermediate oxygen species for the cathode oxygen reduction reaction, a study on the influence of bulk properties on the oxygen incorporation rate is then expected to supply valuable information on the detailed oxygen reduction mechanism.

Values of k^a for BSCFs studied in this thesis are calculated from the average values of R_s listed in Table 4.2 (750 °C and $P(\text{O}_2) = 0.2$ bar on 60 μm diameter microelectrodes); k^a for $\text{La}_{0.6}\text{Sr}_{0.4}\text{CoO}_{3-\delta}$ (LSC), $\text{La}_{0.6}\text{Sr}_{0.4}\text{FeO}_{3-\delta}$ (LSF) and $(\text{La}_{0.8}\text{Sr}_{0.2})_{0.92}\text{MnO}_{3-\delta}$ (LSM80) are calculated from R_s obtained for similarly prepared samples [14, 99].

4.5.1 Lattice constant

Fig. 4.22 shows how the oxygen incorporation rate varies with the lattice constant. From this figure, one cannot draw any overall correlation for BSCF between k^a and the lattice constant although there may be individual correlations if either only the Ba/Sr or only the Fe/Co ratio is varied (dashed lines). SF in the BSCF materials family has an oxygen incorporation rate comparable to that of LSC and LSF, but all other BSCFs have higher k^a values than LSCF and LSM. This indicates that replacement of rare-earth cations by alkaline-earth cations alone is not necessarily sufficient for a significant acceleration, but in general the replacement of Ln^{3+} rare-earth cations on the perovskite's A-site by exclusively A^{2+} alkaline-earth cations improves the oxygen incorporation rate. Since the lattice constant is closely related to many other properties, it is not possible to draw unique conclusions from Fig. 4.22. The lattice constant may influence the oxygen incorporation rate in different ways. The variation of the lattice constant may change the overlap of the oxygen and transition metal orbitals which influences the electronic conductivity. Since

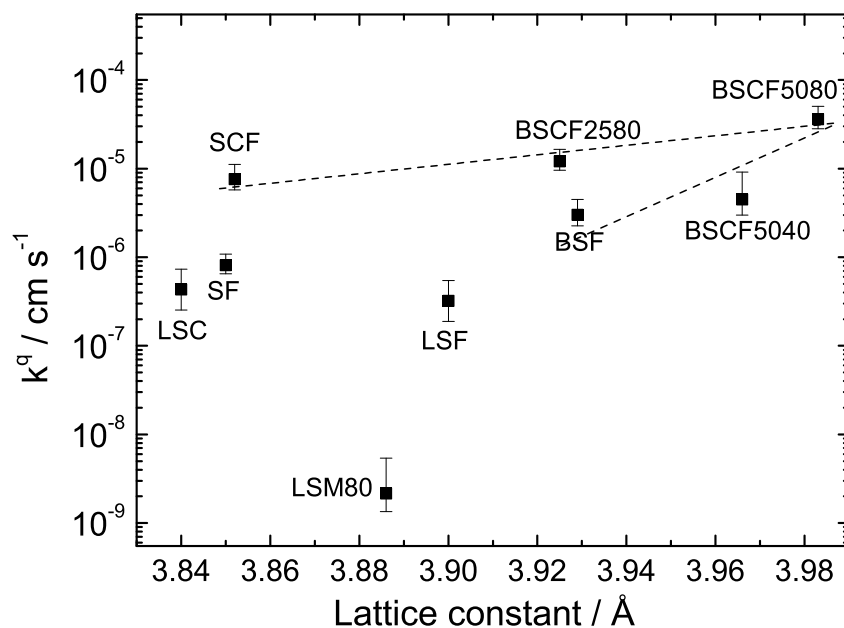


Figure 4.22: Effective oxygen exchange rate constant k^a measured on dense microelectrodes of different cation compositions versus lattice constant (room temperature, furnace-cooled in air). The lattice constant of LSC: Ref. [100], LSF: Ref. [101] for $\text{La}_{0.8}\text{Sr}_{0.2}\text{FeO}_{3-\delta}$ and LSM80: Ref. [102] for $(\text{La}_{0.8}\text{Sr}_{0.2})_{0.925}\text{MnO}_{3-\delta}$.

the lattice constant as well as the oxygen deficiency δ depends on cation composition, they may be related. This means the lattice constant may also influence k^a by affecting the concentration and mobility of oxygen vacancies.

4.5.2 Electronic conductivity

For the electrical percolation in the electrode, a certain electronic conductivity is necessary. How important the electronic conductivity (providing it exceeds a certain required threshold) is for the electrocatalytic oxygen reduction, cannot be decided in advance. LSM, LSCF and BSCF all show p-type electronic conductivities in the semiconducting regime. Doping on the perovskite's A-site by Sr in LaMnO_3 effectively increases the electronic conductivity σ_{eon} . At 750 °C in air, σ_{eon} for LSM is typically in the range of 100-500 S/cm [104]. For LSCF, the conductivities for Co-rich and Fe-rich compositions are rather different (LSC can even exhibit metallic conductivity under certain conditions [106]). Under comparable T and $P(\text{O}_2)$ conditions, σ_{eon} of $\text{La}_x\text{Sr}_{1-x}\text{Co}_y\text{Fe}_{1-y}\text{O}_{3-\delta}$ changes by one order of magnitude [100,101,107]. Compared with LSM and LSCF, σ_{eon} for BSCF5080 is generally one order of magnitude lower and does not exceed 100 S/cm [18, 53].

A plot of k^a versus σ_{eon} is shown in Fig. 4.23. The high electronic conductivity of LSM80 does not lead to a high effective rate constant k^a . In contrast, a high electrocat-

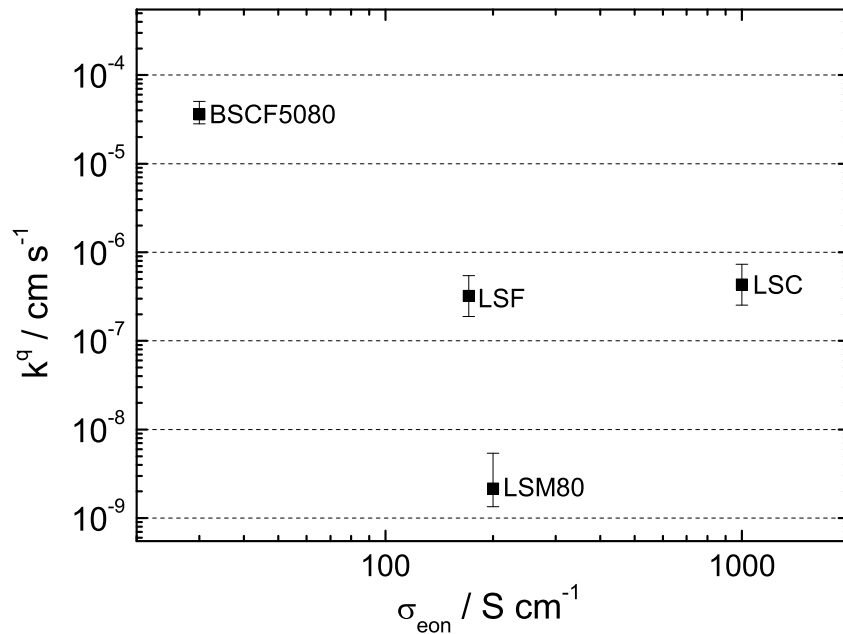


Figure 4.23: Effective oxygen exchange rate constant k^q measured on dense microelectrodes of different cation compositions versus electronic conductivity (750 °C, air). σ_{eon} value for BSCF5080 from Ref. [103], LSM80 from Ref. [104], LSC from Ref. [100] and LSF from Ref. [105].

alytic activity is observed for BSCF5080 even with much lower σ_{eon} . While σ_{eon} varies by one order of magnitude between LSF and LSC, their k^q values hardly differ. These findings indicate that an electronic conductivity as low as around 30 S/cm can suffice for fast oxygen reduction reaction. However, for an electron transfer from the cathode material to adsorbed oxygen species, the coverage of the adsorbed species has to be sufficient and the energy levels have to match as well. Therefore, this non-correlation of k^q and σ_{eon} does not imply that electron transfer can a priori be ruled out as the rate-determining step. Indeed, it only demonstrates that a high σ_{eon} is not a sufficient condition for fast oxygen incorporation kinetics.

4.5.3 Goldschmidt tolerance factor

The Goldschmidt tolerance factor is defined as $t = (r_A + r_O) / \sqrt{2}(r_B + r_O)$ in which r_A , r_B and r_O are the ionic radii of A, B and O ions with their appropriate coordination numbers, valence and spin states; r_A and r_B are calculated as weighted average of the corresponding Shannon cation radii [44]. Interestingly, a study on CO oxidation on $\text{LaTO}_{3\pm\delta}$ (T = transition metal) perovskite catalysts [108] found the samples with higher t to show a higher catalytic activity. It has to be kept in mind that only perovskites with $t \leq 1$ were considered in Ref. [108]. Thus we want to check here whether the tolerance factor is a

relevant quantity also for the oxygen incorporation reaction, and where materials with $t > 1$ appear in the respective plot.

In the LSC [109], LSF [110] and BSCF [111] perovskites, Co^{3+} and Fe^{3+} are the predominant oxidation states for temperature and oxygen partial pressure studied here, i. e., the alkaline-earth cations on the A-site are mainly compensated by the formation of oxygen vacancies. While Fe^{3+} ions are in high spin (HS) state [112], the spin state of Co^{3+} is not so clear. Most of the literature studies agree on that in LaCoO_3 Co^{3+} ions are in intermediate spin (IS) state at relatively low temperature [113] and this is used in our calculation for LSC. However, Co^{3+} ions in BSCF at 750 °C in air may be in IS state or HS state [112]. There are no Shannon ionic radii available for Co^{3+} in IS state; therefore it is estimated by averaging the ionic radii of Co^{3+} in low spin state (0.545 Å) and high spin state (0.61 Å), the error bar shows the difference between these two values. The value for LSM80 was calculated with Mn^{3+} ions in HS state [114]. Depending on the exact rare-earth dopant content and nonstoichiometry, B-site ions typically have mixed valence states. Nevertheless, calculating with the predominant valence state represents well the overall tendencies and therefore serves as a reasonable approximation.

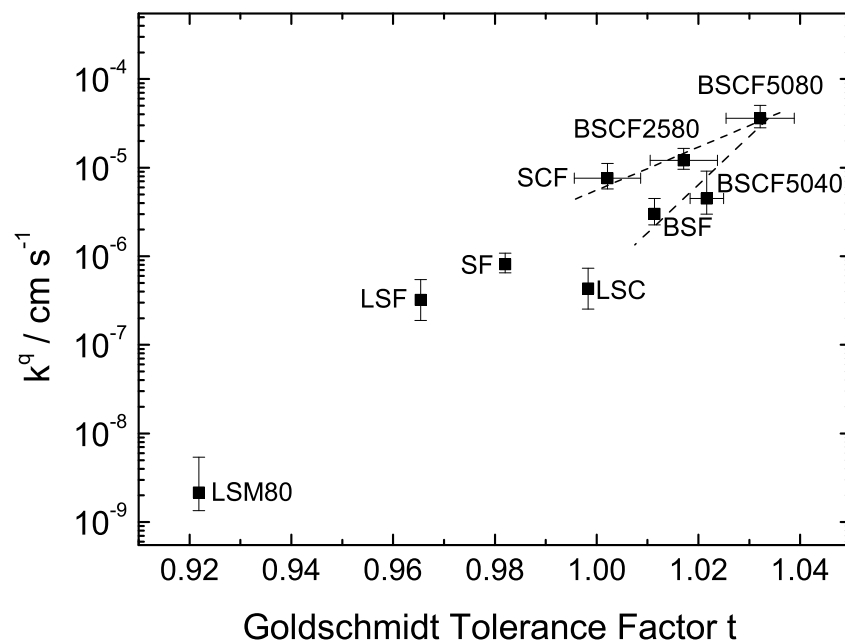


Figure 4.24: Effective oxygen exchange rate constant k^a measured on dense microelectrodes of different cation compositions versus Goldschmidt tolerance factor t .

The influence of the tolerance factor on k^a is shown in Fig. 4.24. There seems to be no universal correlation between k^a and the Goldschmidt tolerance factor t in the BSCF family although when only Ba/Sr or only Co/Fe ratio is varied, k^a may increase with in-

creasing t and correspondingly the oxygen surface reduction is accelerated with increasing t . This is similar to the correlation between k^q and lattice constant shown in Fig. 4.22. Nevertheless, if one allows for some more scatter and includes the other cathode materials, a rough overall correlation between increasing t and increasing k^q can be recognized. The tolerance factor is a parameter that primarily indicates the crystallographic stability of the cubic perovskite structure; the closer to one the more favorable the cubic perovskite structure. If this contribution was decisive, a correlation should appear not with the absolute value of t , but with its deviation from 1. However, this is not the case here. On the other hand, for the materials discussed in Ref. [108] the tolerance factor was empirically related to an averaged metal-oxygen bond strength such that lower t values correspond to higher M-O bond energies. This interpretation translates the rough correlation in Fig. 4.24 into an increase of k^q upon decrease of M-O bond energy, pointing towards a possible role of oxygen vacancies in oxygen incorporation kinetics.

4.5.4 Oxidation enthalpy

The oxidation enthalpy ΔH_{ox} for the reaction $1/2\text{O}_2 + \text{V}_{\text{O}}^{\bullet\bullet} + 2\text{M}_{\text{M}}^{\times} \rightleftharpoons \text{O}_{\text{O}}^{\times} + 2\text{M}_{\text{M}}^{\bullet}$ can be determined from the relationship between $\ln P(\text{O}_2)$ and $1/T$ for selected values of oxygen nonstoichiometry δ (see e. g., Ref. [110, 115, 116]) according to

$$\Delta H_{\text{ox}} = \frac{\partial(\mu_{\text{O}} - \mu_{\text{O}}^0)/T}{\partial(1/T)} \Big|_{\delta} = \frac{R \partial \ln(P(\text{O}_2)/P^0)}{2 \partial(1/T)} \Big|_{\delta} \quad (4.9)$$

or from calorimetric measurements of $P(\text{O}_2)$ change. The values from both methods for $(\text{Ba}_{0.5}\text{Sr}_{0.5})_{1.04}\text{Co}_{0.8}\text{Fe}_{0.2}\text{O}_{3-\delta}$ are shown in Fig. 4.25a and b and they are consistent with each other. The oxidation enthalpy is a parameter that indicates the ability of a material to take up oxygen. ΔH_{ox} of BSCF5080 increases with increasing T , i. e., increasing oxygen nonstoichiometry, (see Fig. 4.25) which is a nonideal behavior. This increase of ΔH_{ox} with T is significantly larger than what could be expected from different heat capacitances c_p of educts (less oxidized perovskite + O_2) and products (more oxidized perovskite) but has also been observed for $\text{SrCo}_{0.8}\text{Fe}_{0.2}\text{O}_{3-\delta}$ [117], $\text{La}_{1-x}\text{Sr}_x\text{CoO}_{3-\delta}$ [109] and $(\text{La},\text{Sr})(\text{Co},\text{Fe})\text{O}_{3-\delta}$ [115]. For LSCF this dependence of oxidation enthalpy was described by a model which additionally consider the disproportionation of the transition metals from 3+ to 2+ and 4+. As shown in Fig. 4.25, the change of ΔH_{ox} upon the change of δ increases with increasing Co content in BSCF, and thus the disproportionation model may also be valid for BSCF.

The relation k^q versus ΔH_{ox} for the studied BSCF compositions is depicted in Fig. 4.26. Although the absolute oxygen nonstoichiometry of these compositions differs, ΔH_{ox} values at 750 °C and for $P(\text{O}_2)$ change from 0.001 bar to 1 bar (0.04 bar to 1 bar for SF and

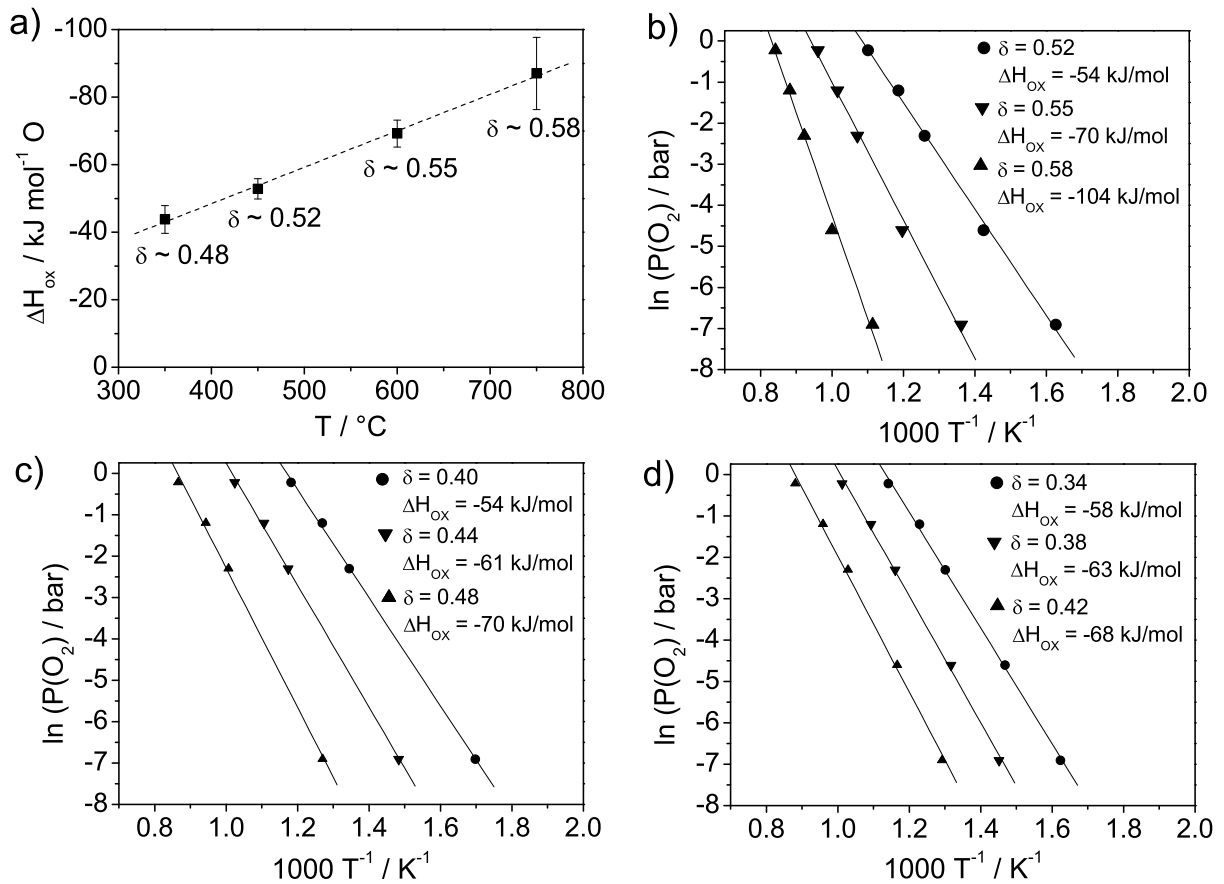


Figure 4.25: a) Calorimetrically determined oxidation enthalpy ΔH_{ox} of $(\text{Ba}_{0.5}\text{Sr}_{0.5})_{1.04}\text{Co}_{0.8}\text{Fe}_{0.2}\text{O}_{3-\delta}$ for different temperatures ($P(\text{O}_2)$ changes 0.001 \leftrightarrow 0.04 \leftrightarrow 1 bar). δ -values for $P(\text{O}_2) = 0.04$ bar are indicated; ΔH_{ox} determined from $\ln P(\text{O}_2) - 1/T$ plot for b) $(\text{Ba}_{0.5}\text{Sr}_{0.5})_{1.04}\text{Co}_{0.8}\text{Fe}_{0.2}\text{O}_{3-\delta}$; c) BSCF5040; d) BSF.

SCF) show no apparent systematic variation for the studied compositions when taking the error bars into account. At lower T such as 600 $^\circ\text{C}$, the error bars as well as the difference between the largest and smallest ΔH_{ox} values decrease further. Since k^{a} changes by almost two orders of magnitude while ΔH_{ox} values keep roughly constant, there seems to be no simple correlation between k^{a} and ΔH_{ox} . This observation is different from the situation for the $(\text{La,Sr})(\text{Mn,Fe,Co})\text{O}_{3-\delta}$ materials family, where a systematic increase of surface reaction rates with decreasing magnitude of the oxidation enthalpy was found [118]. One reason for this difference may be that in the $(\text{La,Sr})(\text{Mn,Fe,Co})\text{O}_{3-\delta}$ family the oxygen vacancy concentration varies by several orders of magnitude between $(\text{La,Sr})(\text{Mn})\text{O}_{3-\delta}$ and $(\text{La,Sr})(\text{Co})\text{O}_{3-\delta}$, and that this variation is to a large degree determined by ΔH_{ox} . Amongst the BSCF materials, the relative changes of oxygen vacancy concentration are much smaller.

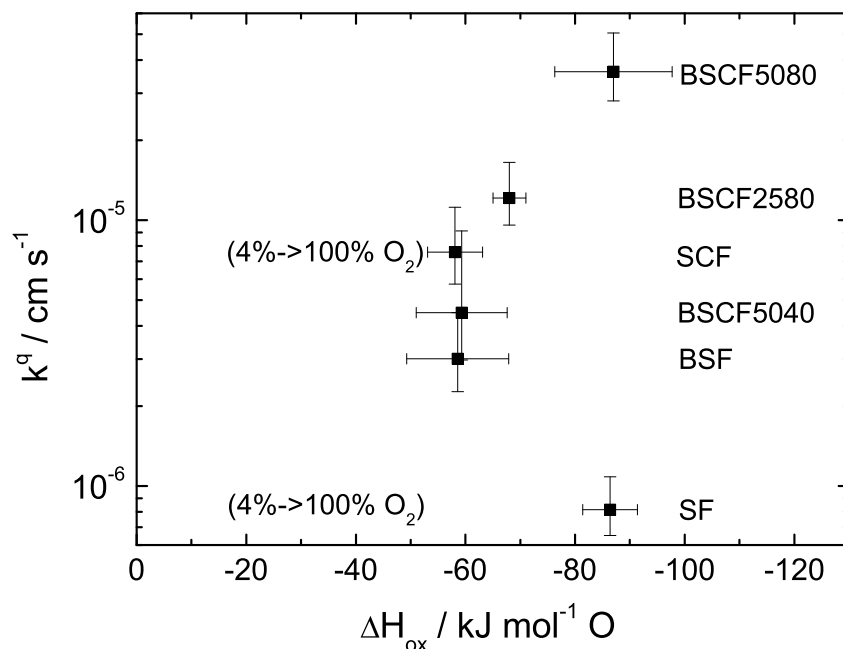


Figure 4.26: Effective oxygen exchange rate constant k^a measured on dense microelectrodes of different cation compositions versus calorimetrically determined oxidation enthalpy ΔH_{ox} (750 °C, $P(\text{O}_2)$ change from 0.001 bar to 1 bar if not indicated otherwise).

4.5.5 Oxygen vacancy concentration

The oxygen stoichiometry determined by thermogravimetric analysis for BSCF are shown in Fig. 4.27. The data for $(\text{Ba}_{0.5}\text{Sr}_{0.5})_{1.04}\text{Co}_{0.8}\text{Fe}_{0.2}\text{O}_{3-\delta}$ determined by thermogravimetric reduction of the oxide and chemical reaction are included in Fig. 4.27a and compared with the literature data for $\text{Ba}_{0.5}\text{Sr}_{0.5}\text{Co}_{0.8}\text{Fe}_{0.2}\text{O}_{3-\delta}$. Considering the remarkable scatter among the literature data, the values from the two methods in this study are in good agreement with each other. The thermodynamic factors of oxygen ω_{O} (section 2.2) determined from the nonstoichiometry data are included in Fig. 4.27b. Taking the error bars into account, the results are identical to the ones in Ref. [49]. The increase of ω_{O} corresponds to the decrease of chemical capacitance towards higher temperature (section 4.3.2). C_{δ} calculated with ω_{O} from the thermogravimetric analysis data ($C_{\delta} = 4F^2 \partial c_{\text{O}} / \partial \mu_{\text{O}} = 4F^2 c_{\text{O}} / \omega_{\text{O}} RT$ [82]) for BSCF5080 at 600 °C is $2.5 \cdot 10^3 \text{ F/cm}^3$ and thus is very close to the value from impedance spectroscopy measurements ($3.1 \cdot 10^3 \text{ F/cm}^3$). There is no obvious correlation between the oxygen incorporation rate and the chemical capacitance C_{δ} from impedance spectroscopy (see Table 4.2) for different cation compositions in BSCF.

Vacancies are necessary reaction partners in the oxygen incorporation reaction. This does not mean that they are for sure involved in the rate-determining step and therefore affect the reaction rate. Nevertheless, based on the $P(\text{O}_2)$ dependence of surface exchange

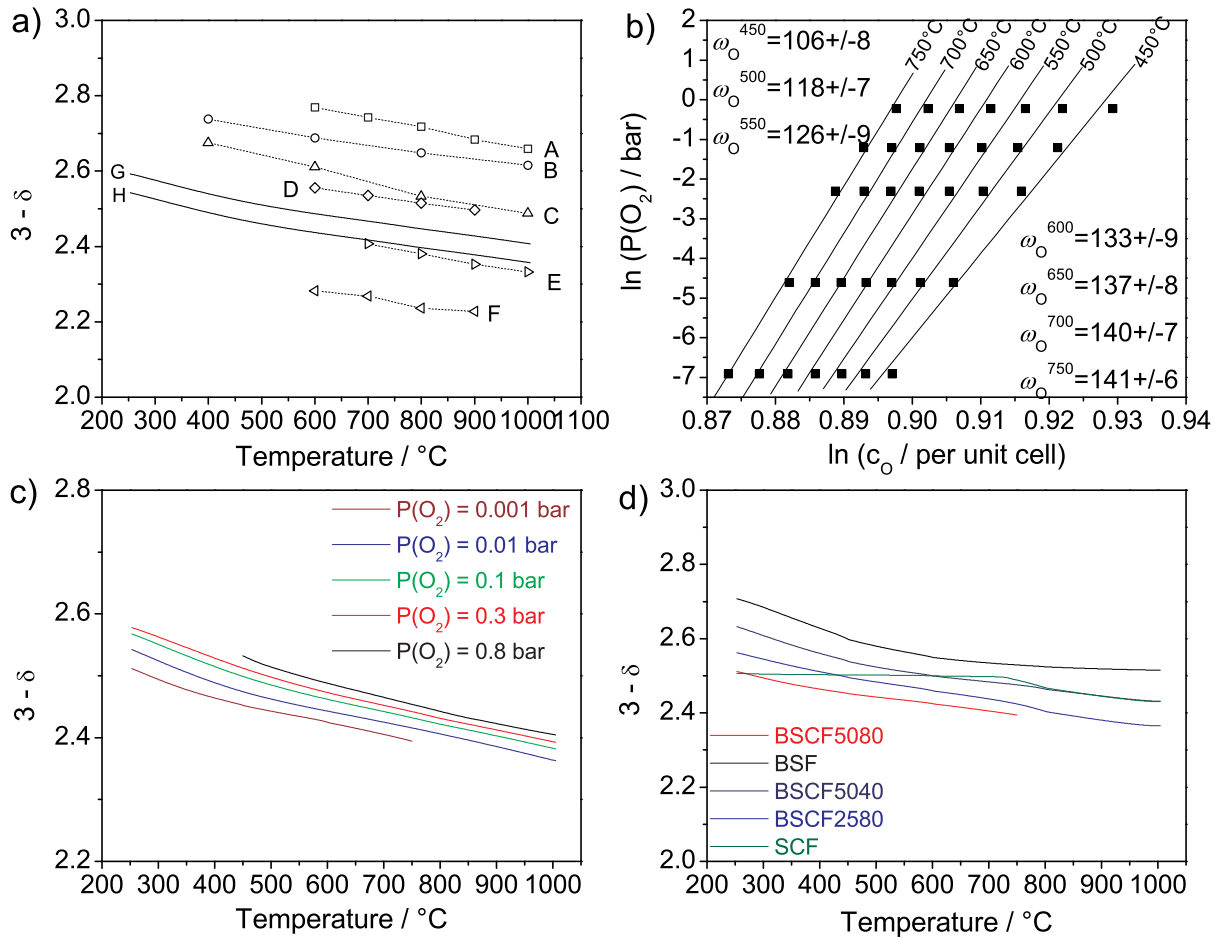


Figure 4.27: a) Temperature dependence of oxygen stoichiometry $3-\delta$ ($P(\text{O}_2)$ is in the range of 0.1 - 0.2 bar, literature values are for $\text{Ba}_{0.5}\text{Sr}_{0.5}\text{Co}_{0.8}\text{Fe}_{0.2}\text{O}_{3-\delta}$ and values from this work are for $(\text{Ba}_{0.5}\text{Sr}_{0.5})_{1.04}\text{Co}_{0.8}\text{Fe}_{0.2}\text{O}_{3-\delta}$). A = [52] B = [10]; C = [53]; D = [49]; E = [27]; F = [54]; G = this work, absolute δ value determined from thermogravimetric reduction of the oxide; H = this work, absolute δ value determined from chemical reaction method; b) Thermodynamic factor of oxygen between 450 and 750 $^{\circ}\text{C}$ for $(\text{Ba}_{0.5}\text{Sr}_{0.5})_{1.04}\text{Co}_{0.8}\text{Fe}_{0.2}\text{O}_{3-\delta}$; c) Temperature dependence of $3-\delta$ for $(\text{Ba}_{0.5}\text{Sr}_{0.5})_{1.04}\text{Co}_{0.8}\text{Fe}_{0.2}\text{O}_{3-\delta}$ at various $P(\text{O}_2)$; d) Temperature dependence of $3-\delta$ for BSCFs with different cation compositions at $P(\text{O}_2) = 0.001$ bar.

coefficients, or on the coincidence of high tracer exchange coefficients k^* with high tracer diffusion coefficients D^* (known to be proportional to the concentration of oxygen vacancies $c_{\text{V}\bullet}$), an important role of oxygen vacancies for the incorporation reaction has previously been suggested [13, 91, 118, 119].

Compared with LSM80, k^a of LSCF is two orders of magnitude higher (see e. g., Fig. 4.24). A strong increase of k^* ($\approx k^a$) from LSM to LSCF perovskites was observed in Ref. [91] and correlated with an increase in D^* . This empirical correlation

$$\delta \log k^* \approx 0.5 \delta \log D^* \quad (4.10)$$

where δ refers to the variation of the material, implies that within this materials family the activation energies of k^* and D^* - although varying from material to material - are coupled [118]:

$$E_a(k^*) \approx 0.5E_a(D^*) \approx 0.5(E_a(D_{V_{\bullet\bullet}}) - \Delta H_{\text{ox}}) \quad (4.11)$$

D^* is given by $D_{V_{\bullet\bullet}}$ and $c_{V_{\bullet\bullet}}$ according to $D^* = f \cdot c_{V_{\bullet\bullet}} D_{V_{\bullet\bullet}} / c_{\text{O}}$ (equation 2.14). $D_{V_{\bullet\bullet}}$ is to a good approximation materials independent within the LSM-LSCF family [21, 48], but $c_{V_{\bullet\bullet}}$ varies strongly. Since the temperature dependence of electronic charge carrier concentrations in these materials is small [120, 121], $c_{V_{\bullet\bullet}} \propto e^{+\Delta H_{\text{ox}}/kT}$ and $E_a(D^*) \approx E_a(D_{V_{\bullet\bullet}}) - \Delta H_{\text{ox}}$ follows. For perovskites in the LSM-LSC-LSF family the $V_{\text{O}}^{\bullet\bullet}$ mobility and its activation energy $E_a(D_{V_{\bullet\bullet}}) \approx 0.9$ eV hardly depend on the cation composition [21, 122]. Thus, the variation of $E_a(D^*)$ for different perovskites is due to the different oxidation enthalpies ΔH_{ox} .

According to Equation 4.11, the surface reaction activation energy $E_a(k^*)$ also contains a contribution $0.5E_a(D_{V_{\bullet\bullet}})$ related to the motion of a vacancy or the corresponding jump of an atomic oxygen species in the rate-determining step [123]. In Ref. [118] this was interpreted by a reaction mechanism in which the incorporation of adsorbed atomic oxygen species into $V_{\text{O}}^{\bullet\bullet}$ determines the overall rate. Recent DFT studies of oxygen incorporation into LSM [73, 124] revealed that the incorporation of adsorbed O^- into a neighboring $V_{\text{O}}^{\bullet\bullet}$ occurs without barrier and is fast, whereas the preceding approach of $V_{\text{O}}^{\bullet\bullet}$ to the adsorbed O^- is comparably slow and rate-determining. Thus the mechanistic interpretation of Ref. [118] has to be corrected. The contribution of $0.5E_a(D_{V_{\bullet\bullet}})$ is not assigned to the jump of the adsorbed O^- any more, but to the approach of a $V_{\text{O}}^{\bullet\bullet}$ by diffusion within the surface layer to the O^- . For diffusion of an oxygen vacancy in the surface layer, the jump barrier amounts to only 70 % of the bulk value [73] which is in reasonable agreement with the contribution $0.5E_a(D_{V_{\bullet\bullet}})$ appearing in the k^* - D^* correlation. As a consequence the reaction rate is proportional not only to the concentration of $V_{\text{O}}^{\bullet\bullet}$ but also to their mobility at the surface. Since $D_{V_{\bullet\bullet}}$ is approximately constant, the acceleration of oxygen incorporation in LSCF compared to LSM is mainly due to the increased $c_{V_{\bullet\bullet}}$ in LSCF. $c_{V_{\bullet\bullet}}$ for LSM80 is 4×10^{-9} per unit cell calculated from $D_{V_{\bullet\bullet}}$ and D^* in Refs. [21, 51] while $c_{V_{\bullet\bullet}}$ for LSCF under similar conditions is generally between 0.05 and 0.2 per unit cell.

The correlation between k^q and the bulk oxygen vacancy concentration $c_{V_{\bullet\bullet}}$ for LSCF and BSCF materials is shown in Fig. 4.28. Moving from SF which has a k^q comparable with LSCF to BSCF5080, a perceptible speedup of the oxygen incorporation reaction rate occurs: k^q increases by more than an order of magnitude, although $c_{V_{\bullet\bullet}}$ increases only slightly by a factor smaller than 2. The nonlinear increase of k^q upon the increase of $c_{V_{\bullet\bullet}}$ in Fig. 4.28 suggests that the oxygen vacancies are involved in the rate-determining

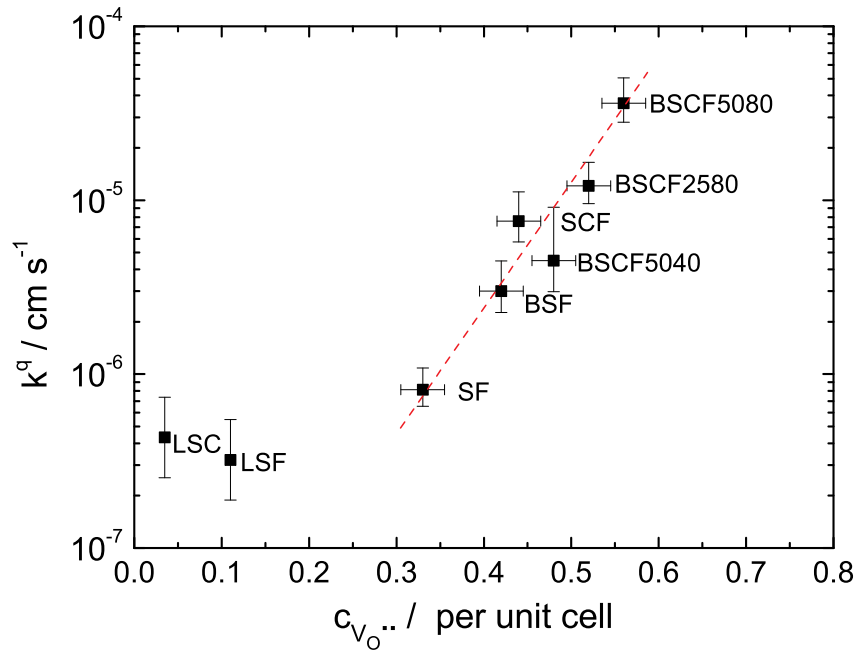


Figure 4.28: Effective oxygen exchange rate constant k^q measured on dense microelectrodes of different cation compositions versus bulk oxygen vacancy concentration $c_{V_{O^{\bullet\bullet}}}$ (750 °C, $P(O_2) = 0.2$ bar). $c_{V_{O^{\bullet\bullet}}}$ value for LSF is from Ref. [110], for LSC from Ref. [109], for SF from Ref. [125] and for BSCF2580 from Ref. [27] for $Ba_{0.2}Sr_{0.8}Co_{0.8}Fe_{0.2}O_{3-\delta}$.

step of the oxygen incorporation reaction, but in this case the main accelerating effect from oxygen vacancies is not their increased concentration. Based on these discussions, the nonlinear increase of k^q upon the increase of $c_{V_{O^{\bullet\bullet}}}$ may be mainly attributed to the increased oxygen vacancy mobility (accompanied by a lower activation energy $E_a(D_{V_{O^{\bullet\bullet}}}) = 0.5$ eV). To verify this hypothesis, the correlation of k^q and $D_{V_{O^{\bullet\bullet}}}$ was studied.

4.5.6 Oxygen vacancy diffusion coefficient

In Fig. 4.29, k^q (600 °C, $P(O_2) = 0.2$ bar) is plotted versus the product of bulk oxygen vacancy concentration $c_{V_{O^{\bullet\bullet}}}$ (600 °C, $P(O_2) = 0.2$ bar) and oxygen vacancy diffusion coefficient $D_{V_{O^{\bullet\bullet}}}$ (600 °C, $P(O_2) = 0.5$ bar, calculated from D^*). ($c_{V_{O^{\bullet\bullet}}} \times D_{V_{O^{\bullet\bullet}}}$) is proportional to the oxygen ion conductivity (Equation 2.9). In the $\log(k^q)$ - $\log(c_{V_{O^{\bullet\bullet}}} \times D_{V_{O^{\bullet\bullet}}})$ plot, the exponent at 600 °C is 1.16. This means k^q is almost exactly proportional to the bulk oxygen ion conductivity. Due to the moderately different activation energies of $D_{V_{O^{\bullet\bullet}}}$ for BSCF with different cation compositions, this exponent should be slightly modified at different temperatures. Nevertheless, the correlation between k^q and $D_{V_{O^{\bullet\bullet}}}$ strongly supports the previous hypothesis: the oxygen vacancies are involved in the rate-determining step and the accelerated oxygen vacancy diffusion is the main determining factor for the

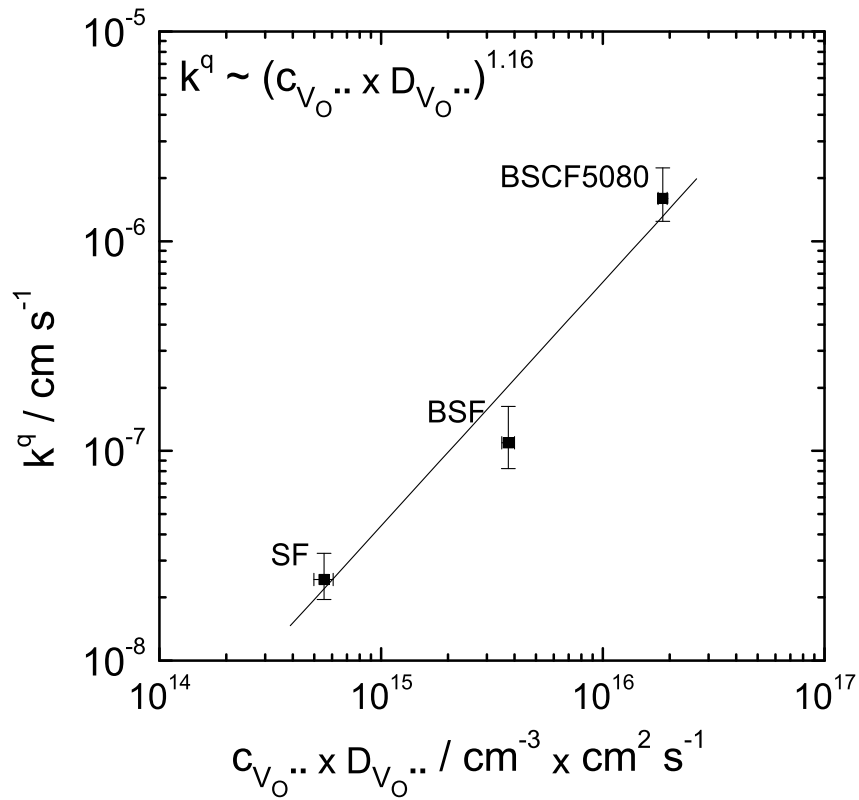


Figure 4.29: Effective oxygen exchange rate constant k^q measured on dense microelectrodes of different cation compositions versus the product of bulk oxygen vacancy concentration $c_{V_{O^{\bullet\bullet}}}$ (600 °C, $P(\text{O}_2) = 0.2$ bar) and oxygen vacancy diffusion coefficient $D_{V_{O^{\bullet\bullet}}}$ (600 °C, $P(\text{O}_2) = 0.5$ bar, calculated from D^*).

increased oxygen incorporation reaction rate in BSCF compared with LSCF/SF.

4.6 Proposed oxygen incorporation mechanism for $(\text{Ba,Sr})(\text{Co,Fe})\text{O}_{3-\delta}$

From the aforementioned experimental observations and discussions, there are three main conclusions which help to propose a reasonable oxygen incorporation mechanism:

- (1) From the similar temperature and $P(\text{O}_2)$ dependence of R_s , the six compositions studied in the BSCF materials family can be assumed to have the same oxygen reduction mechanism (in the case of SrFeO_3 , the mechanism may slightly differ from the one for other BSCFs and is closer to the one for LSCF where the encounter of an oxygen vacancy and an adsorbed O_2^- occurs by the diffusion of O_2^- towards the oxygen vacancy);
- (2) From the $P(\text{O}_2)$ dependence of R_s with a exponent higher than 0.5, the reaction order of oxygen molecules is 1;
- (3) The correlation between the oxygen incorporation rate (calculated from R_s) and the

product of oxygen vacancy concentration and mobility indicates that the oxygen vacancy is involved in the rate-determining step and the diffusion of the (surface) oxygen vacancies plays an important role in the oxygen incorporation reaction.

Based on these conclusions, the number of possible reaction mechanisms is effectively reduced. To finally propose a most probable reaction mechanism, the missing experimental information on the oxygen species at the surface can be obtained from DFT calculations which can supply detailed information on e. g., the energies of the intermediate oxygen species and the barriers of the individual steps. Since such calculations are not available yet for BSCF materials, results for LaMnO₃ [73, 124] will be discussed (keeping in mind the differences in the defect chemistry between these materials). The most stable surface was found to be MnO₂ [001] terminated [126]. The following conclusions therefore refer to the situation on MnO₂ [001] terminated LaMnO₃ slabs.

- (1) The adsorption enthalpy (per O₂ molecule) is much more negative for formation of 2O⁻ than for O₂⁻ or O₂²⁻, thus O⁻ is the adsorbate with the highest coverage.
- (2) The dissociation of a peroxide species sticking in an oxygen vacancy occurs with a very small barrier.
- (3) The diffusion of an adsorbed O⁻ on the surface atop M_M after the dissociation step has a high activation energy of 2.0 eV. In contrast to the diffusion of O⁻, the activation energy for surface diffusion of a V_O^{••} is only about 70 % of the bulk activation energy value (resulting in 0.7 eV for LSM and probably smaller for BSCF). Therefore the encounter of an adsorbed O⁻ and a V_O^{••} is mainly through the diffusion of the V_O^{••} towards the O⁻.

Combining the experimental observations and the information from DFT calculations, the oxygen incorporation into BSCF is proposed to proceed in the way depicted in Fig. 4.30 composed of the following steps: a) First, the oxygen molecule adsorbs on the bare BSCF surface (not into an oxygen vacancy) forming a superoxide ion. This is an exothermic and fast process; b) The surface diffusion of a V_O^{••} towards the adsorbed superoxide ion (including a fast electron transfer) results in a peroxide ion sticking in the oxygen vacancy. This is the rate-determining step (for BSCF5080 with the highest oxygen vacancy mobility, its rate comes close to the rate for O₂⁻ chemisorption). The rate of this reaction is proportional to [O₂⁻]·[V_O^{••}]·D^{surf}_{V_O^{••}} and it also validates the high P(O₂) dependence of R_s; c) The subsequent dissociation of the peroxide occurs with a very small barrier ending up with an adsorbed O⁻. This is also a fast step; d) The incorporation of the adsorbed O⁻ into BSCF occurs through the diffusion of an oxygen vacancy towards the adsorbed O⁻. Due to the higher coverage of O⁻ than O₂⁻, this step is faster than rate-determining step b.

This mechanism comprises oxygen vacancy motion in two steps, one of which is rate-

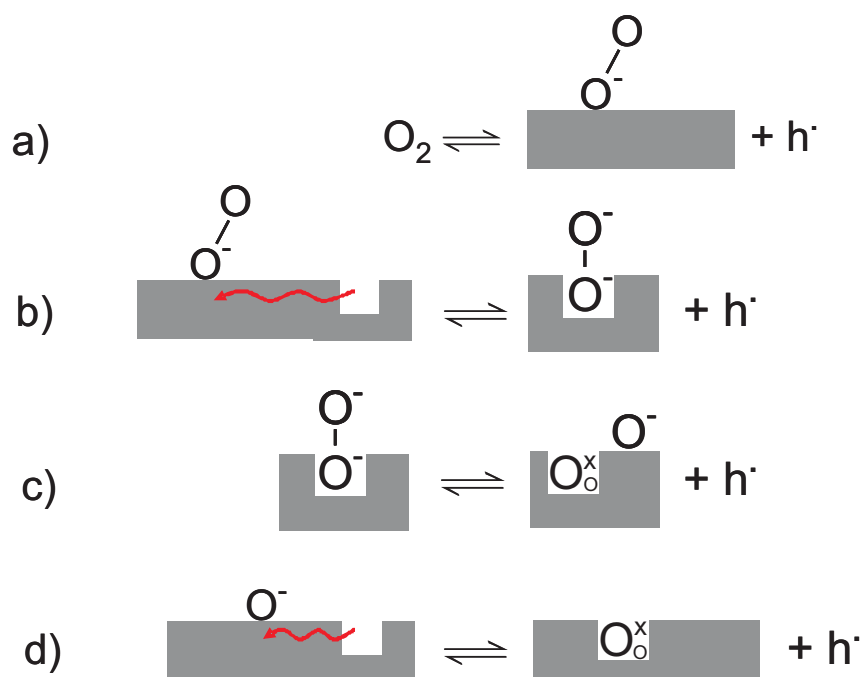


Figure 4.30: Proposed oxygen incorporation mechanism into BSCF: a) Chemisorption of an oxygen molecule on the bare BSCF surface and formation of the superoxide ion; b) The surface diffusion of a $V_O^{\bullet\bullet}$ towards the adsorbed superoxide ion (including a fast electron transfer) results in a peroxide ion sticking in the oxygen vacancy; c) The subsequent dissociation of the peroxide; d) The incorporation of the adsorbed O^- into BSCF occurs through the diffusion of an oxygen vacancy towards the adsorbed O^- .

determining, and thus emphasizes the importance of having not only a high oxygen vacancy concentration but also a high oxygen vacancy (surface) mobility.

Although this suggested mechanism is in good agreement with the observed dependence of the reaction rate on $c_{V_O^{\bullet\bullet}}$, $D_{V_O^{\bullet\bullet}}$ and $P(O_2)$, one has to keep in mind that a reaction mechanism is always a hypothesis which, strictly speaking, can only be falsified but never finally proven. Nevertheless it contributes to the understanding of the surface reaction and can suggest guidelines for further materials optimization.

4.7 Perovskites with mixed monovalent and trivalent ions at A-site

Compared with LSCF SOFC cathodes, the substitution of La^{3+} rare-earth cations by exclusively A^{2+} alkaline-earth metal cations in BSCF generally effectively accelerated the rate of oxygen incorporation into the perovskites, according to the suggested mechanism by introducing more oxygen vacancies with high mobility. However, the alkaline-earth metals lead to carbonate formation which decrease the cathode performance as mentioned

in section 4.2.2. One possibility to avoid this problem is to substitute the 2+ alkaline-earth metals with a combination of 1+ alkali metals and 3+ rare-earth metals. This will maintain the average A-site valence state to be around 2+ and probably also the high oxygen vacancy concentration and mobility in the perovskite structure which are responsible for the fast oxygen incorporation into the perovskite.

For this purpose, powders with various A-site cation combinations were synthesized. The A-site cations were chosen based on a rough estimation of the Goldschmidt tolerance factor, which should be as close to 1 as possible. In the case of (La, Ag)Co_{0.4}Fe_{0.6}O_{3-δ}, the solubility of Ag in the perovskite structure is rather limited. For the powder of nominal composition La_{0.9}Ag_{0.1}Co_{0.4}Fe_{0.6}O_{3-δ} with an Ag content as low as 10 %, the X-Ray diffractogram indicates the existence of elementary silver which is similar to the observations for Sr_{0.9}Ag_{0.1}TiO_{3-δ} prepared by the solgel-citrates (SGC) technique [127]. In the case of (La, K)Co_{0.4}Fe_{0.6}O_{3-δ} and (Nd, K)Co_{0.4}Fe_{0.6}O_{3-δ}, obtaining a single phase powder is difficult. It is not clear if K is incorporated into the perovskite structure and at the same time there is always K segregation by reacting with CO₂/H₂O in air. A nominal La_{0.45}K_{0.45}Co_{0.4}Fe_{0.6}O_{3-δ} powder was soaked in water and it is possible to remove most of K in the powder while maintaining predominant perovskite peaks in the diffractogram. The La:K:Co:Fe ratio was 0.45:0.01:0.40:0.60 for the soaked powder according to ICP-OES measurements. From in-situ X-Ray diffraction, the perovskite was stable upto at least 1200 °C. Based on these results, it is possible that the K-containing compound is removed by soaking. The remaining powder is therefore composed of a mixture of a A-site deficient perovskite and a B-cation oxide. To test the performance of this A-site deficient perovskite, La_{0.5}Co_{0.4}Fe_{0.6}O_{3-δ} powder was directly synthesized and studied with microelectrode impedance spectroscopy. The X-ray diffractogram for the synthesized La_{0.5}Co_{0.4}Fe_{0.6}O_{3-δ} is shown in Fig. 4.31a. It is composed of a predominant orthorhombic perovskite phase which can be indexed on the basis of the Pnma(62) space group and a B-cation oxide indicated by the peaks marked with the arrows. Thin films and microelectrodes with this composition were prepared in the same way as for BSCF. Fig. 4.31b shows the X-ray diffractogram for a 100 nm La_{0.5}Co_{0.4}Fe_{0.6}O_{3-δ} thin film on a (100)-oriented YSZ single crystal. The film prefers (112) and (002) orientation. The peak from the oxide phase appears in the film as well and is indicated by the arrow.

The average values from the impedance spectroscopy measurements at 750 °C and P(O₂) = 0.2 bar on 60 μm microelectrodes for R_s and C_δ are 44.92 (± 12.00) Ωcm² and (4.3±0.8)×10⁻⁹ F respectively. R_s of La_{0.5}Co_{0.4}Fe_{0.6}O_{3-δ} is one order of magnitude higher than LSCFs studied in Ref. [14] and C_δ two orders of magnitude lower. This is most probably due to the phase impurity of this powder. From the temperature dependence

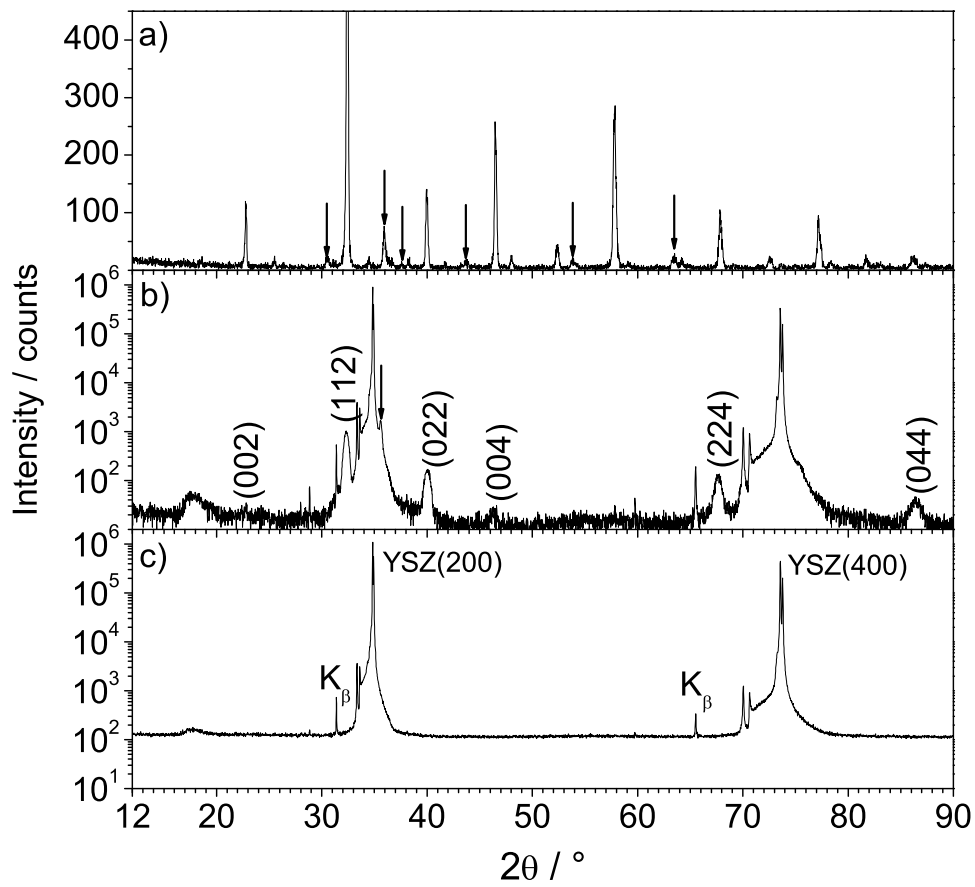


Figure 4.31: X-ray diffractograms of a) $\text{La}_{0.5}\text{Co}_{0.4}\text{Fe}_{0.6}\text{O}_{3-\delta}$ powder; b) a 100 nm $\text{La}_{0.5}\text{Co}_{0.4}\text{Fe}_{0.6}\text{O}_{3-\delta}$ thin film on a YSZ single crystal with (100) orientation; c) a YSZ single crystal with (100) orientation.

measured on two samples, the activation energies related to R_s is $2.1 (\pm 0.1)$ eV and the formal activation energy of C_δ $E_a(C_\delta)$ is $0.11 (\pm 0.01)$ eV.

Chapter 5

Summary

This work is mainly concerned with the mixed conducting perovskite solid solution materials family $\text{Ba}_{1-x}\text{Sr}_x\text{Co}_y\text{Fe}_{1-y}\text{O}_{3-\delta}$ (BSCF) which is discussed as solid oxide fuel cell (SOFC) cathode material. The aim is to get an improved understanding of the complex oxygen reduction reaction on such oxides in general, and in particular for the application as catalytically active cathode in SOFC.

As a SOFC cathode candidate, the stability of BSCFs with regard to the application was first studied on powders synthesized from the metal nitrates by the glycine nitrate process. With respect to the stability towards electrolyte materials, at 750 °C $(\text{Ba}_{0.5}\text{Sr}_{0.5})_{1.04}\text{Co}_{0.8}\text{Fe}_{0.2}\text{O}_{3-\delta}$ (BSCF5080) already reacts with 8 mol % $\text{Y}_2\text{O}_3\text{-ZrO}_2$ (YSZ). This undesired reactivity is more pronounced than that of $\text{La}_{0.6}\text{Sr}_{0.4}\text{Co}_{0.8}\text{Fe}_{0.2}\text{O}_{3-\delta}$ and YSZ. At 850 °C, BSCF5080 even starts to react with $\text{Ce}_{0.9}\text{Ge}_{0.1}\text{O}_{2-\delta}$ (CGO). The increased reactivity of BSCF5080 may mainly come from the higher A-/B- cation size mismatch and therefore BSCFs with lower Ba content or Ba-deficiency may show higher stability with the electrolytes. Concerning the stability of BSCFs under CO_2 -containing atmosphere, a high Ba content is detrimental. Even Ba-deficiency can not effectively inhibit the formation of carbonates. As a result, Ba-containing perovskite oxide cathodes require highly purified oxidizing atmosphere which is not very practical. Some of the BSCF compositions with cubic perovskite structure from the synthesis slowly transform to noncubic phases at intermediate temperatures. For the investigated compositions, no obvious relationship between the cubic perovskite stability at intermediate temperatures and the Goldschmidt tolerance factor could be established. However, BSCF with lower Co content shows higher long-term phase stability, therefore Co/Fe ratio may play an important role. Co changes its oxidation state more easily and the ionic radius change upon the change of the oxidation state facilitates the formation of face-sharing octahedra with shorter B-O bond length and the resulting noncubic perovskites.

The oxygen reduction kinetics and mechanism was studied on geometrically well de-

finned microelectrodes. 100 nm thick dense thin films of the respective compositions were deposited by pulsed laser deposition (PLD) on (100)-oriented YSZ single crystals. X-ray diffraction (XRD) shows the films maintain high phase purity and exhibit a highly textured structure which depends on the film thickness, the exact cation composition and the substrate. Scanning electron microscopy (SEM) measurements confirm that the thin films prepared under the present deposition conditions are dense films with columnar growth. The thin films were subsequently patterned into circular microelectrodes with 20 to 100 μm diameter by photolithography. Silver paste and foil were attached to the back side of the sample as counter electrode. Impedance spectra were recorded on these microelectrodes and the temperature, oxygen partial pressure and dc bias dependence was studied.

It is found that the oxygen reduction on these BSCF microelectrodes proceeds through the “bulk path”, i. e., incorporation of oxygen into the electrode on the whole electrode surface, and subsequent oxygen ions diffusion through the electrode bulk. The rate of oxygen incorporation is limited by the oxygen surface reaction rate. Based on the equivalent circuit developed from previous works, the surface resistance R_s corresponding to the oxygen surface incorporation reaction can be quantitatively compared for different cation compositions in BSCF. The temperature dependence of R_s is similar for the six BSCF compositions studied and the activation energies are in the range of 1.3 to 1.8 eV. In the oxygen partial pressure $P(\text{O}_2)$ dependence, all compositions have an exponent between -0.5 and -1 in the $\log R_s$ - $\log P(\text{O}_2)$ plot indicating the reaction order of the oxygen molecules is 1. Both cathodic and anodic dc bias decrease R_s . Applied cathodic bias values up to 400 mV do not introduce obvious irreversible changes on a less degraded (“fresh”) sample while a cathodic bias of 300 mV already obviously decreases R_s and introduces irreversible changes on a more degraded (“aged”) sample.

Due to the difficulty in directly detecting the coverage and nature of the intermediate oxygen species on the surface of the cathodes under SOFC operation conditions, correlations between the oxygen incorporation reaction rate k^a calculated from R_s and various bulk materials properties were studied and used to supply information on the detailed oxygen reduction mechanism. There is no straightforward correlation between k^a and the lattice constant, the electronic conductivity, the Goldschmidt tolerance factor or the oxidation enthalpy. However, k^a increases nonlinearly with increasing oxygen vacancy concentration $c_{V_{\text{O}}^{\bullet\bullet}}$ which indicates that the oxygen vacancies are involved in the rate-determining step of the oxygen incorporation reaction. The nonlinear increase of k^a with increasing $c_{V_{\text{O}}^{\bullet\bullet}}$ was assumed to be caused by the increased oxygen vacancy mobility.

To confirm this assumption, acquiring reliable oxygen vacancy diffusion coefficient

data is necessary. Due to the relatively low density of sintered pellets and the complexity in the experiments, oxygen vacancy diffusion coefficients from conductivity relaxation experiments for BSCF5080 were not accurate enough. However, reliable oxygen vacancy diffusion coefficients were obtained on 250 nm dense BSCF thin films deposited by PLD on (100)-oriented MgO single crystals. A gas-tight gold cover layer was deposited on top of the BSCF film by evaporation. In order to enable oxygen isotope exchange between BSCF and the atmosphere, a cut about 30 μm wide with relatively sharp edges was created through the gold and BSCF layers with an automatic dicing saw. Isotope exchange was carried out at different temperatures and later on the ^{18}O concentration profile in the quenched samples was analyzed by time-of-flight secondary ion mass spectrometry (TOF-SIMS). The oxygen vacancy diffusion coefficients $D_{V_{\text{O}}^{\bullet\bullet}}$ calculated from the extracted oxygen tracer diffusion coefficient D^* for BSCF5080 are significantly higher than that of $(\text{La,Sr})(\text{Mn,Fe,Co})\text{O}_{3-\delta}$ perovskites. The activation energy E_a of $D_{V_{\text{O}}^{\bullet\bullet}}$ for BSCF5080 is only 0.47 ± 0.04 eV which is much lower than that of $\text{Ba}_{0.5}\text{Sr}_{0.5}\text{FeO}_{3-\delta}$ (BSF, 1.1 ± 0.1 eV), $\text{SrFeO}_{3-\delta}$ (SF, 0.9 ± 0.1 eV) and $(\text{La,Sr})(\text{Mn,Fe,Co})\text{O}_{3-\delta}$ (≈ 0.9 eV). The high $D_{V_{\text{O}}^{\bullet\bullet}}$ and low E_a is thought to be due to low cation charge (A^{2+} , fraction of Co^{2+}) and high polarizability (Ba^{2+} , Co^{2+}).

With $D_{V_{\text{O}}^{\bullet\bullet}}$ calculated from D^* , the correlation between k^{q} and $D_{V_{\text{O}}^{\bullet\bullet}}$ is confirmed. While the increase of k^{q} from $(\text{La,Sr})(\text{Mn})\text{O}_{3\pm\delta}$ (LSM) to $(\text{La,Sr})(\text{Co,Fe})\text{O}_{3-\delta}$ (LSCF) is mainly due to the increase of the oxygen vacancy concentration, the increase of k^{q} from LSCF/SF to $\text{Ba}_{0.5}\text{Sr}_{0.5}\text{Co}_{0.8}\text{Fe}_{0.2}\text{O}_{3-\delta}$ mainly comes from the accelerated (surface) oxygen vacancy diffusion. Based on the experimental observations and the conclusions from DFT calculations on LaMnO_3 slabs, the rate-determining step of the oxygen incorporation reaction on BSCF is proposed to be the diffusion of an oxygen vacancy towards an adsorbed O_2^- resulting in an O_2^{2-} adsorbed at the vacancy position, the dissociation of which is fast.

There are intrinsic problems of BSCF when it is applied as SOFC cathode, such as the undesired reactivity with the electrolyte, the carbonate formation under CO_2 -containing atmosphere and the long-term phase transformation. It is almost impossible to solve them only by varying the cation composition within this material family. Therefore BSCF may not be applicable as a SOFC cathode. Nevertheless, based on the proposed oxygen incorporation mechanism for BSCF, the combination of high oxygen vacancy concentration and mobility is an adequate criterion for selecting other SOFC cathode candidates. In BSCF, the high oxygen vacancy concentration is due to the fact that the 4+ oxidation state of B-site cations is not so stable, and therefore the 2+ oxidation state at A-site is mainly compensated by the formation of oxygen vacancies. To avoid the problems introduced by Ba and maintain the average oxidation state of A-site to be 2+, perovskites with a

combination of 1+ alkali metals and 3+ rare earth metals at A-site were studied. The solubility of Ag in $(\text{La,Ag})\text{Co}_{0.4}\text{Fe}_{0.6}\text{O}_{3-\delta}$ perovskites is rather limited. For K-containing $(\text{La,K})\text{Co}_{0.4}\text{Fe}_{0.6}\text{O}_{3-\delta}$ and $(\text{Nd,K})\text{Co}_{0.4}\text{Fe}_{0.6}\text{O}_{3-\delta}$ perovskites, it is difficult to get phase pure powders. R_s from impedance spectroscopy studies of the material with a nominal composition $\text{La}_{0.5}\text{Co}_{0.4}\text{Fe}_{0.6}\text{O}_{3-\delta}$ and a predominant perovskite phase is one order of magnitude higher than LSCF and this is most probably due to the phase impurities. Based on the mechanism suggested in this thesis, fast oxygen exchange materials should have a high oxygen vacancy mobility. This motivates to investigate perovskites with highly polarizable A-cations. In this respect, Bi^{3+} instead of Ba^{2+} would be an interesting candidate, which also might help to reduce the carbonate formation problem.

References

- [1] S. C. Singhal, *Solid State Ionics* **152**, 405 (2002).
- [2] D. J. L. Brett, A. Atkinson, N. P. Brandon, and S. J. Skinner, *Chem. Soc. Rev.* **37**, 1568 (2008).
- [3] The theoretical cell potential E^o for SOFCs with the reaction of $\text{H}_2 + 1/2\text{O}_2 \rightarrow \text{H}_2\text{O}(\text{g})$ is equal to $-\Delta G^o/zF = 248/(2 \times 96485) \text{ V} = 1.28 \text{ V}$ at 900 K. $-\Delta G^o$ is the standard value of the change in Gibbs energy of this reaction.
- [4] N. Q. Minh, *J. Am. Ceram. Soc.* **76**, 563 (1993).
- [5] L. J. Gauckler, D. Beckel, B. E. Buergler, E. Jud, U. P. Muecke, M. Prestat, J. L. M. Rupp, and J. Richter, *Chimia* **58**, 837 (2004).
- [6] N. P. Brandon, S. J. Skinner, and B. C. H. Steele, *Annu. Rev. Mater. Res.* **33**, 183 (2003).
- [7] J. Fleig, K. Kreuer, and J. Maier, Ceramic fuel cells, in *Handbook of Advanced Ceramics*, edited by S. Somiya et al., pg. 57-103, Elsevier, 2003.
- [8] S. J. Skinner, *Int. J. Inorg. Mater.* **3**, 113 (2001).
- [9] Z. P. Shao, W. S. Yang, Y. Cong, H. Dong, J. H. Tong, and G. X. Xiong, *J. Membr. Sci.* **172**, 177 (2000).
- [10] Z. P. Shao and S. M. Haile, *Nature* **431**, 170 (2004).
- [11] V. Brichzin, J. Fleig, H.-U. Habermeier, G. Cristiani, and J. Maier, *Solid State Ionics* **152**, 499 (2002).
- [12] J. Mizusaki, T. Saito, and H. Tagawa, *J. Electrochem. Soc.* **143**, 3065 (1996).
- [13] Y. L. Yang, C. L. Chen, S. Y. Chen, C. W. Chu, and A. J. Jacobson, *J. Electrochem. Soc.* **147**, 4001 (2000).

- [14] F. S. Baumann, J. Fleig, G. Cristiani, B. Stuhlhofer, H.-U. Habermeier, and J. Maier, *J. Electrochem. Soc.* **154**, B931 (2007).
- [15] F. S. Baumann, J. Fleig, H.-U. Habermeier, and J. Maier, *Solid State Ionics* **177**, 3187 (2006).
- [16] R. Merkle and J. Maier, *Angew. Chem. Int. Ed.* **47**, 3874 (2008).
- [17] F. A. Kröger, *The Chemistry of Imperfect Crystals*, North-Holland Publ. Comp., Amsterdam, 2nd edition, 1974.
- [18] B. Wei, Z. Lu, S. Y. Li, Y. Q. Liu, K. Y. Liu, and W. H. Su, *Electrochem. Solid-State Lett.* **8**, A428 (2005).
- [19] H. Schmalzried, *Solid State Reactions*, VCH, Weinheim, 2nd edition, 1981.
- [20] H. Rickert, *Electrochemistry of Solids*, Springer-Verlag, Berlin, 1982.
- [21] T. Ishigaki, S. Yamauchi, K. Kishio, J. Mizusaki, and K. Fueki, *J. Solid State Chem.* **73**, 179 (1988).
- [22] J. Maier, *Physical Chemistry of Ionic Materials*, John Wiley & Sons, Chichester, 2004.
- [23] J. Maier, *Solid State Ionics* **112**, 197 (1998).
- [24] J. Maier, *Solid State Ionics* **135**, 575 (2000).
- [25] R. Merkle, J. Maier, and J. Fleig, Mechanistic understanding and electrochemical modeling of mixed conducting (SOFC) electrodes, in *Handbook of Fuel Cells - Fundamentals, Technology and Applications (Volume 5)*, edited by W. Vielstich, H. Yokokawa, and H. A. Gasteiger, pg. 425-440, John Wiley & Sons, 2009.
- [26] S. B. Adler, *Chem. Rev.* **104**, 4791 (2004).
- [27] S. Svarcová, K. Wiik, J. Tolchard, H. J. M. Bouwmeester, and T. Grande, *Solid State Ionics* **178**, 1787 (2008).
- [28] T. Akashi, M. Nanko, T. Maruyama, Y. Shiraishi, and J. Tanabe, *J. Electrochem. Soc.* **145**, 2090 (1998).
- [29] O. Schulz, M. Martin, C. Argirusis, and G. Borchardt, *Phys. Chem. Chem. Phys.* **5**, 2308 (2003).

- [30] M. S. Islam, *J. Mater. Chem.* **10**, 1027 (2000).
- [31] Y. Teraoka, H. M. Zhang, K. Okamoto, and N. Yamazoe, *Mater. Res. Bull.* **23**, 51 (1988).
- [32] A. Esquirol, N. P. Brandon, J. A. Kilner, and M. Mogensen, *J. Electrochem. Soc.* **151**, A1847 (2004).
- [33] F. S. Baumann, J. Fleig, H.-U. Habermeier, and J. Maier, *Solid State Ionics* **177**, 1071 (2006).
- [34] Y. Teraoka, H. M. Zhang, S. Furukawa, and N. Yamazoe, *Chem. Lett.* **14**, 1743 (1985).
- [35] L. M. Liu, T. H. Lee, L. Qiu, Y. L. Yang, and A. J. Jacobson, *Mater. Res. Bull.* **31**, 29 (1996).
- [36] Z. P. Shao, G. X. Xiong, J. H. Tong, H. Dong, and W. S. Yang, *Sep. Purif. Technol.* **25**, 419 (2001).
- [37] Z. P. Shao, H. Dong, G. X. Xiong, Y. Cong, and W. S. Yang, *J. Membr. Sci.* **183**, 181 (2001).
- [38] S. M. Sun, M. Rebeilleau-Dassonneville, X. F. Zhu, W. L. Chu, and W. S. Yang, *Catal. Today* **149**, 167 (2010).
- [39] Z. P. Shao, J. Mederos, W. C. Chueh, and S. M. Haile, *J. Power Sources* **162**, 589 (2006).
- [40] Q. S. Zhu, T. A. Jin, and Y. Wang, *Solid State Ionics* **177**, 1199 (2006).
- [41] Z. Yang, A. S. Harvey, A. Infortuna, and L. J. Gauckler, *J. Appl. Crystallogr.* **42**, 153 (2009).
- [42] K. Yamaura, H. W. Zandbergen, K. Abe, and R. J. Cava, *J. Solid State Chem.* **146**, 96 (1999).
- [43] K. Wiik, S. Aasland, H. L. Hansen, I. L. Tangen, and R. Odegard, *Solid State Ionics* **152**, 675 (2002).
- [44] R. D. Shannon, *Acta Cryst.* **A32**, 751 (1976).
- [45] H. H. Wang, C. Tablet, W. S. Yang, and J. Caro, *Mater. Lett.* **59**, 3750 (2005).

- [46] H. Lu, Y. Cong, and W. S. Yang, *Solid State Ionics* **177**, 595 (2006).
- [47] H. H. Wang, Y. Cong, and W. S. Yang, *J. Membr. Sci.* **210**, 259 (2002).
- [48] J. A. Kilner, R. A. De Souza, and I. C. Fullarton, *Solid State Ionics* **86-8**, 703 (1996).
- [49] E. Bucher, A. Egger, P. Ried, W. Sitte, and P. Holtappels, *Solid State Ionics* **179**, 1032 (2008).
- [50] J. E. ten Elshof, M. H. R. Lankhorst, and H. J. M. Bouwmeester, *Solid State Ionics* **99**, 15 (1997).
- [51] R. A. De Souza and J. A. Kilner, *Solid State Ionics* **106**, 175 (1998).
- [52] H. H. Wang, W. S. Yang, C. Tablet, and J. Caro, *Diffusion Fundamentals* **2**, 46 (2005).
- [53] P. Y. Zeng, Z. H. Chen, W. Zhou, H. X. Gu, Z. P. Shao, and S. M. Liu, *J. Membr. Sci.* **291**, 148 (2007).
- [54] S. McIntosh, J. F. Vente, W. G. Haije, D. H. A. Blank, and H. J. M. Bouwmeester, *Solid State Ionics* **177**, 1737 (2006).
- [55] L. A. Chick, L. R. Pederson, G. D. Maupin, J. L. Bates, L. E. Thomas and G. J. Exarhos, *Mater. Lett.* **10**, 6 (1990).
- [56] K. Kleveland, M.-A. Einarsrud, and T. Grande, *J. Am. Ceram. Soc.* **83**, 3158 (2000).
- [57] H. I. Yoo, B. J. Wuensch, and W. T. Petuskey, *Solid State Ionics* **150**, 207 (2002).
- [58] F. S. Baumann, *Oxygen reduction kinetics on mixed conducting SOFC model cathodes*, PhD thesis, Stuttgart, 2006.
- [59] M. Vračar, A. Kuzmin, R. Merkle, J. Purans, E. A. Kotomin, J. Maier, and O. Mathon, *Phys. Rev. B: Condens. Matter* **76**, 174107 (2007).
- [60] A. Y. Yan, B. Liu, Y. L. Dong, Z. J. Tian, D. Z. Wang, and M. J. Cheng, *Appl. Catal., B* **80**, 24 (2008).
- [61] J. A. Kilner, B. C. H. Steele, and L. Ilkov, *Solid State Ionics* **12**, 89 (1984).
- [62] R. J. Chater, S. Carter, J. A. Kilner, and B. C. H. Steele, *Solid State Ionics* **53-56**, 859 (1992).

- [63] P. Fielitz and G. Borchardt, *Solid State Ionics* **144**, 71 (2001).
- [64] M. Burriel, G. Garcia, J. Santiso, J. A. Kilner, R. J. Chater, and S. J. Skinner, *J. Mater. Chem.* **18**, 416 (2008).
- [65] R. A. De Souza, J. Zehnpfenning, M. Martin, and J. Maier, *Solid State Ionics* **176**, 1465 (2005).
- [66] X. F. Zhu, H. H. Wang, and W. S. Yang, *Solid State Ionics* **177**, 2917 (2006).
- [67] P. Bezdicka, A. Wattiaux, J. C. Grenier, M. Pouchard, and P. Hagenmuller, *Z. Anorg. Allg. Chem.* **619**, 7 (1993).
- [68] S. McIntosh, J. F. Vente, W. G. Haije, D. H. A. Blank, and H. J. M. Bouwmeester, *Chem. Mater.* **18**, 2187 (2006).
- [69] J. J. Tunney, P. Whitfield, X. M. Du, and M. L. Post, *Thin Solid Films* **426**, 221 (2003).
- [70] S. Y. Hou, J. Kwo, R. K. Watts, J. Y. Cheng, and D. K. Fork, *Appl. Phys. Lett.* **67**, 1387 (1995).
- [71] X. H. Zhu, S. K. Lee, H. N. Lee, and D. Hesse, *Mater. Sci. Eng., B* **118**, 60 (2005).
- [72] R. A. Evarestov, E. A. Kotomin, Y. A. Mastrikov, D. Gryaznov, E. Heifets, and J. Maier, *Phys. Rev. B: Condens. Matter* **72**, 214411 (2005).
- [73] E. A. Kotomin, Y. A. Mastrikov, E. Heifets, and J. Maier, *Phys. Chem. Chem. Phys.* **10**, 4644 (2008).
- [74] H. Y. Tu, Y. Takeda, N. Imanishi, and O. Yamamoto, *Solid State Ionics* **117**, 277 (1999).
- [75] Y. Tsur, T. D. Dunbar, and C. A. Randall, *J. Electroceram.* **7**, 25 (2001).
- [76] Z. S. Duan, M. Yang, A. Y. Yan, Z. F. Hou, Y. L. Dong, Y. Chong, M. J. Cheng, and W. S. Yang, *J. Power Sources* **160**, 57 (2006).
- [77] A. Y. Yan, M. J. Cheng, Y. L. Dong, W. S. Yang, V. Maragou, S. Q. Song, and P. Tsiakaras, *Appl. Catal., B* **66**, 64 (2006).
- [78] M. Arnold, H. H. Wang, and A. Feldhoff, *J. Membr. Sci.* **293**, 44 (2007).
- [79] A. Boulouf and D. Louer, *J. Appl. Crystallogr.* **24**, 987 (1991).

- [80] M. Arnold, T. M. Gesing, J. Martynczuk, and A. Feldhoff, *Chem. Mater.* **20**, 5851 (2008).
- [81] L. Ge, W. Zhou, R. Ran, S. M. Liu, Z. P. Shao, W. Q. Jin, and N. P. Xu, *J. Membr. Sci.* **306**, 318 (2007).
- [82] J. Jamnik and J. Maier, *Phys. Chem. Chem. Phys.* **3**, 1668 (2001).
- [83] J. Fleig and J. Maier, *J. Europ. Ceram. Soc.* **24**, 1343 (2004).
- [84] J. Fleig, *Solid State Ionics* **150**, 181 (2002).
- [85] F. S. Baumann, J. Maier, and J. Fleig, *Solid State Ionics* **179**, 1198 (2008).
- [86] S. Lee, Y. Lim, E. A. Lee, H. J. Hwang, and J.-W. Moon, *J. Power Sources* **157**, 848 (2006).
- [87] F. L. Jones, *The Physics of Electrical Contacts*, Clarendon Press, Oxford, 1957.
- [88] M. Filal, C. Petot, M. Mokchah, C. Chateau, and J. L. Carpentier, *Solid State Ionics* **80**, 27 (1995).
- [89] J. Fleig, *Phys. Chem. Chem. Phys.* **7**, 2027 (2005).
- [90] F. S. Baumann, J. Fleig, M. Konuma, U. Starke, H.-U. Habermeier, and J. Maier, *J. Electrochem. Soc.* **152**, A2074 (2005).
- [91] R. A. De Souza and J. A. Kilner, *Solid State Ionics* **126**, 153 (1999).
- [92] J. Crank, *The Mathematics of Diffusion*, Oxford University Press, Oxford, 1956.
- [93] P. Ried, E. Bucher, W. Preis, W. Sitte, and P. Holtappels, *ECS Trans.* **7**, 1217 (2007).
- [94] L. Wang, R. Merkle, F. S. Baumann, J. Fleig, and J. Maier, *ECS Trans.* **7**, 1015 (2007).
- [95] A. Berenov, A. Atkinson, J. A. Kilner, E. Bucher, and W. Sitte, in *Proceedings of the Eighth Fuel Cell Forum Lucerne*, 2008. Some uncertainty might also arise from the fact that only a part of the profile was recorded, i. e., the leveling off at c_{bg}^* is not directly observed.
- [96] J. Yoo, A. Verma, S. Y. Wang, and A. J. Jacobson, *J. Electrochem. Soc.* **152**, A497 (2005).

- [97] J. A. Kilner and R. J. Brook, *Solid State Ionics* **6**, 237 (1982).
- [98] C. A. J. Fisher, M. Yoshiya, Y. Iwamoto, J. Ishii, M. Asanuma, and K. Yabuta, *Solid State Ionics* **177**, 3425 (2007) (No $V_{\text{O}}^{\bullet\bullet}$ hopping barrier or E_a available from this reference).
- [99] J. Fleig, H. R. Kim, J. Jamnik, and J. Maier, *Fuel Cells* **8**, 330 (2008).
- [100] S. R. Wang, M. Katsuki, M. Dokiya, and T. Hashimoto, *Solid State Ionics* **159**, 71 (2003).
- [101] L. W. Tai, M. M. Nasrallah, H. U. Anderson, D. M. Sparlin, and S. R. Sehlin, *Solid State Ionics* **76**, 259 (1995).
- [102] F. Zheng and L. R. Pederson, *J. Electrochem. Soc.* **146**, 2810 (1999).
- [103] Z. H. Chen, R. Ran, W. Zhou, Z. P. Shao, and S. M. Liu, *Electrochim. Acta* **52**, 7343 (2007).
- [104] J. Mizusaki, Y. Yonemura, H. Kamata, K. Ohyama, N. Mori, H. Takai, H. Tagawa, M. Dokiya, K. Naraya, T. Sasamoto, H. Inaba, and T. Hashimoto, *Solid State Ionics* **132**, 167 (2000).
- [105] E. V. Bongio, H. Black, F. C. Raszewski, D. Edwards, C. J. McConville, and V. R. W. Amarakoon, *J. Electroceram.* **14**, 193 (2005).
- [106] M. Sogaard, P. V. Hendriksen, M. Mogensen, F. W. Poulsen, and E. Skou, *Solid State Ionics* **177**, 3285 (2006).
- [107] K. Yasumoto, Y. Inagaki, M. Shiono, and M. Dokiya, *Solid State Ionics* **148**, 545 (2002).
- [108] T. Shimizu, *Chem. Lett.* **9**, 1 (1980).
- [109] J. Mizusaki, Y. Mima, S. Yamauchi, K. Fueki, and H. Tagawa, *J. Solid State Chem.* **80**, 102 (1989).
- [110] J. Mizusaki, M. Yoshihiro, S. Yamauchi, and K. Fueki, *J. Solid State Chem.* **58**, 257 (1985).
- [111] A. S. Harvey, F. J. Litterst, Z. Yang, J. L. M. Rupp, A. Infortuna, and L. J. Gauckler, *Phys. Chem. Chem. Phys.* **11**, 3090 (2009).

- [112] A. S. Harvey, Z. Yang, A. Infortuna, D. Beckel, J. A. Purton, and L. J. Gauckler, *J. Phys.: Condens. Matter* **21** (2009).
- [113] M. A. Korotin, S. Yu. Ezhov, I. V. Solovyev, V. I. Anisimov, D. I. Khomskii, and G. A. Sawatzky, *Phys. Rev. B: Condens. Matter* **54**, 5309 (1996).
- [114] H. Kamata, Y. Yonemura, J. Mizusaki, H. Tagawa, K. Naraya, and T. Sasamoto, *J. Phys. Chem. Solids* **56**, 943 (1995).
- [115] E. Bucher, W. Sitte, G. B. Caraman, V. A. Cherepanov, T. V. Aksenova, and M. V. Ananyev, *Solid State Ionics* **177**, 3109 (2006).
- [116] S. Stølen, E. Bakken, and C. E. Mohn, *Phys. Chem. Chem. Phys.* **8**, 429 (2006).
- [117] N. Grunbaum, L. Mogni, F. Prado, and A. Caneiro, *J. Solid State Chem.* **177**, 2350 (2004).
- [118] R. Merkle, J. Maier, and H. J. M. Bouwmeester, *Angew. Chem. Int. Ed.* **43**, 5069 (2004).
- [119] R. H. E. van Doorn, I. C. Fullarton, R. A. De Souza, J. A. Kilner, H. J. M. Bouwmeester, and A. J. Burggraaf, *Solid State Ionics* **96**, 1 (1997).
- [120] T. Ohtani, K. Kuroda, K. Matsugami, and D. Katoh, *J. Eur. Ceram. Soc.* **20**, 2721 (2000).
- [121] A. Mineshige, M. Kobune, S. Fujii, Z. Ogumi, M. Inaba, T. Yao, and K. Kikuchi, *J. Solid State Chem.* **142**, 374 (1999).
- [122] J. Mizusaki, I. Yasuda, J. Shimoyama, S. Yamauchi, and K. Fueki, *J. Electrochem. Soc.* **140**, 467 (1993).
- [123] Point defect migration steps in fast steps preceding or following the rate-determining step do not contribute to the overall activation energy since these steps are represented by quasi-equilibrium mass action laws. Only when a movement occurs within the rate-determining step its migration energy contributes to the overall activation energy.
- [124] R. Merkle, Y. A. Mastrikov, E. Heifets, E. A. Kotomin, M. Kukla, and J. Maier, *ECS Trans.* **25**, 2753 (2009).
- [125] J. Mizusaki, M. Okayasu, S. Yamauchi, and K. Fueki, *J. Solid State Chem.* **99**, 166 (1992).

-
- [126] Y. A. Mastrikov, E. Heifets, E. A. Kotomin, and J. Maier, *Surf. Sci.* **603**, 326 (2009).
- [127] L. Fabbrini, A. Kryukov, S. Cappelli, G. L. Chiarello, I. Rossetti, C. Oliva, and L. Forni, *J. Catal.* **232**, 247 (2005).

Acknowledgments

At this moment, I would like to express my gratitude to all who directly or indirectly contributed to this work.

I thank Prof. Dr. Joachim Maier for giving me the opportunity to work in his group at the Max Planck Institute for Solid State Research.

I am grateful to Prof. Dr. Emil Roduner and Prof. Dr. Ir. Eric Jan Mittemeijer for being on my examination committee.

I thank Dr. Dieter Fischer for being on my Ph. D. advisory committee and the helpful suggestions and discussions.

Special thanks go to the Hans L. Merkle-Stiftung for generous financial support of this thesis.

I am greatly indebted to Dr. Rotraut Merkle who supervised me during the whole process in all aspects, from the detailed instructions of the experiments to the proof-reading of the presentations and the thesis. Being an experienced scientist in this field, she not only shared her knowledge and experience with me, but also influenced me with her preciseness. Her hard-working cheered me up when I was down and her calmness set me free from anxiety. I am especially grateful for her always being available for the discussions even when she was quite busy.

Without the various support from the colleagues in the two Max Planck Institutes in Stuttgart, this work would not be complete. Therefore I express my sincere gratitude to the following colleagues: I thank Georg Cristiani and Benjamin Stuhlhofer (Technology Service Group) for the preparation of the microelectrode samples by PLD and photolithography. I thank Tolga Acartürk and Dr. Ulrich Starke (Interface Analysis Service Group) for the help with SIMS experiments, especially Tolga for being a patient and experienced tutor in teaching me to carry out the SIMS measurements. I thank Gabi Götz for measuring an appreciable number of X-ray diffractograms, the corresponding analysis and helpful discussions. I thank my predecessor Dr. Frank Baumann for his initial help in the lab and kind suggestions. I thank Albrecht Meyer and Gerhard Werner (Analytical Chemistry Lab, MPI-MF) for the ICP-OES measurements, Tamina Neumaier for carrying out the DSC measurements, Barbara Baum, Annette Zechmeister and Helmut Wendel (Crys-

tal Preparation Group) for preparing samples with different geometries, Marion Hagel and Stephan Schmid (Technology Service Group) for gold deposition and surface profile measurements, Peter Senk for helping with the determination of oxygen nonstoichiometry by chemical reaction. I further thank Annette Fuchs, Jochen Weber, Bernhard Fenk and Thomas Reindl (Department von Klitzing), Sabine Kühnemann (Stuttgart Center for Electron microscopy, MPI-MF), Viola Duppel and Claudia Kamella (Department Simon), Eva Peters (Department Kern) for SEM measurements, Helmut Kammerlander (Glass Workshop) for the preparation of the glassware used for conductivity relaxation experiments, Dr. Mitsuharu Konuma (Interface Analysis Service Group) for performing the XPS experiments, Wolfgang König (Department Keimer) for IR measurements, Dr. Yuguo Guo and Barbara Reichert for performing the AFM measurements, Joerg Dahmen (Department Aldinger, MPI-MF) and Dr. Paul Balog for pellet sintering by hot pressing, Bernd Hinrichsen and Dr. Robert Dinnebier (X-ray Diffraction Group), Michael Fischer and Dr. Yvonne Liebold (Department Jansen) for XRD measurements on air-sensitive samples, Marion Kelsch (Stuttgart Center for Electron microscopy, MPI-MF) for tenuating SIMS sample of depth profile measurement, Felicitas Predel for metallographic sample preparation, Sanela Goeres (Department Simon) and Dr. Reinhard Kremer (Chemical Service Group) for the magnetic susceptibility measurements, Marie-Luise Schreiber for hot gas extraction measurements for the determination of oxygen nonstoichiometry, Werner Dieterich (High Pressure Group) for the help with high pressure experiments, Uwe Traub for his friendly help with all computer related problems, Udo Klock, Willi Kussmaul and Ewald Schmitt for various technical support, Dr. Guoqiang Liu, Dr. Vitaliy Alexandrov, Dr. Dominik Samuelis and Dr. Miloš Vračar for the helping with regards to \LaTeX . I thank Sofia Weiglein for her essential help in the administrative work.

I thank all of my colleagues in the group of Prof. Maier as well as the Chinese colleagues from both institutes who made my days in FKF enjoyable and indelible.

I thank my parents and friends for their loving support. I would like to apologize to my beloved grandmother for not being able to accompany her through the last part of her life.

Curriculum Vitae

Name: Lei Wang
Date of Birth: 22.03.1982
Place of Birth: Qingdao, Shandong, P. R. China

09/1988-07/1994 Renmin Road No. 3 Primary School, Qingdao, China
09/1994-07/1997 Qingdao No. 16 Middle School, Qingdao, China
09/1997-07/2000 Qingdao No. 2 High School, Qingdao, China
07/2000 College Entrance Examination

09/2000 - 06/2004 Bachelor of Engineering in Materials Science and Engineering,
Southeast University, Nanjing, China

11/2003 - 08/2004 Exchange student, University of Ulm, Ulm, Germany

11/2003 - 11/2005 Master of Science in Advanced Materials,
University of Ulm, Ulm, Germany

Thesis: Mechanical Properties and Stability at the Nanoscale of
Metallic Multilayers

02/2006 - 11/2009 PhD at the Max Planck Institute for Solid State Research
in the Department of Prof. Dr. J. Maier and at the University
of Stuttgart, Stuttgart, Germany

Thesis: $\text{Ba}_{1-x}\text{Sr}_x\text{Co}_y\text{Fe}_{1-y}\text{O}_{3-\delta}$ SOFC Cathode Materials:
Bulk Properties, Kinetics and Mechanism of Oxygen Reduction